Firmato digitalmente da VANELLA ANDREA C=IT

UNIVERSITÀ DI SIENA 1240

Department of Physical Sciences, Earth and Environment

PhD in Experimental Physics

XXXIV Cycle

Coordinator: Prof. Riccardo Paoletti

Nanoparticle formation in nanoporous structures and applications

Disciplinary Scientific Sector: FIS/03

In Partial Fulfillment of the Requirements for the Degree of Doctor of Philosphy

PhD Student:
Andrea Vanella
University of Siena
Via Roma 56

Supervisor:
Prof. Emilio Mariotti
University of Siena

Co-Supervisor:
Prof.ssa Carmela Marinelli
University of Siena

2020/2021

Abstract

In the recent years the scientific community demonstrates an increasing interest in the study of nanoparticles and their properties, such as interaction with a surface and the adsorption/desorption characteristic. The latte properties, as well the formation and growth of nanoparticles, can be controlled by a proper light source. On the other hand having a much larger specific surface to increase the adsorbed amount of atoms, is a desirable characteristic of the system. That is on of the reason of the large exploitation of nanoporous material in many different research fields. Porous glass presents a wide variety of benefits: thermal and chemical stability, low production cost, easiness of handling and large value of specific surface area, which can be of the order tens square meters per grams.

This thesis work falls into the context described above, in particular it aims to investigate the adsorption/desorption process of alkali atoms onto different randomly oriented pores structures, as well the formation of aggregates in the pores of the adsorbed atoms by using different external light sources. The control of the desorption process as well as the formation and the desorption of nanoparticles make use of two light induced process: Light Induced Atomic Desorption or LIAD and the Surface Plasmon Induced Desorption. The main difference between these two effects, beside the physics behind the two effects is intrinsically different, is that for the latter is required a resonant light source resonant with the plasmonic oscillation while for the LIAD it is not needed any resonant wavelength.

The main and newer part of the work is done in a chamber were is present an Ultra High Vacuum regime. Most of the studies on this topic were performed in vapor filled cells. The use of an Ultra High Vacuum regime for this work is done to overcome some drawback of the vapor cells, such as the impossibility to change atomic species once that a cell is built or the difficult controlling of the atomic density. Indeed in this apparatus the loading process is done with an externally removable dispenser controlled by a current flowing into it. Hence the loading process is no more continuous an can be switched off by switching off the flowing current. Once the UHV regime is reached, the first step is the loading of the porous sample. Then the adsorption properties at different wavelengths are studied as well as that eventual desorption of the atomic specimen. The formation of nanoparticles in the porous structures are induced by an external light source under different condition of intensity and illumination time. Similar studies are also performed in alkali vapor filled cells, in order to compare the results. There were performed simultaneously measurements by on the optical signal and electric signal by means of a channeltron.

The measurements performed in this work showed that by using porous glass, with different average pores size and under an appropriate illumination, it is possible to exploit the LIAD effect to enhance the aggregation of Rb nanoparticles in UHV regime. The most satisfying sample revealed to be a film of nanoporous alumina of 300 nm thickness.

Acknowledgements

I wish to thank Prof. Emilio Mariotti for his help and support during my work days. I would like to thank also Prof.ssa Carmela Marinelli for her valuable advices.

Special thanks go to the researchers of the PhysNano laboratory at the Saint Petersburg National Research University of Information technologies, Mechanics and Optics (ITMO) for the preparation of the alumina samples analyzed in this work.

I also want to thank Leonardo Stiaccini for the constant and precious technical help and assistance.

Finally, I have to thank Nicole for always being there.

Contents

List of Figures

Chapter 1

Introduction

In this section, a brief introduction of this thesis work and its aim is reported. In sec. 1.1 a general overview of the adsorption and desorption mechanisms and the state of the art of nanoporous materials is provided. The use of light as a tool for changing and checking the atom - surface interaction and the formation of metal nanoparticles in porous structures by means of the Light-Induced Desorption Effect is briefly discussed. Finally, a list of the main goals of this thesis work is provided. In sec. 1.2 a brief description of the structure of the thesis is given.

1.1 Summary

Nanoparticles and their properties, such as adsorption and diffusive properties, are nowadays studied in a wide range of field: chemistry, biology, physics, engineering and mathematical modelling [1–8]. Hence, the ability in controlling their formation/destruction and in driving the adsorption/desorption dynamics plays a key role in the interactions at a nanoscale, with a deep impact on nanotechnology and material science as well as on the comprehension of fundamental physics aspects [9, 10].

Among the various possible tools to control the adsorption/desorption processes and the growth of nanoparticles, light irradiation revealed to be a particularly efficient method [11–13].

On the other hand, the interaction of atoms, molecules and nanoparticles, is strongly affected by the features of the surface, as the size of pores and cavities, the crystalline geometry, the nature of the chemical bonds, the surrounding medium. In

order to thoroughly investigate the diffusion and transport of particles and quasi-particles in pores or fractal structures, different experimental and theoretical studies have been performed [14–17]. Various diffusion processes and peculiar transport phenomena of atoms and photons (such as the Lévy flight) in porous materials and engineered optical materials have been studied and reported [18].

Nanoporous materials and porous glass have been obtaining an increasing interest because of their low production cost, easy handling, thermal and chemical stability as well as their high value of specific surface area which can be of the order of tens square meter per gram.

It was demonstrated that the pore structure plays a fundamental role in nucleation, hence in nanoparticles formation and crystallization [19–21]. Moreover, the possibility of easily obtaining a randomly oriented pore distribution can be employed to study the effects of non-ordered structure [4, 22, 23].

The growth and formation of nanoparticles in such an environment is a consequence of the atomic surface adsorption/desorption processes and of nucleation centers such as pore structural defects. The nanoparticles growing can be addressed by making use of light, both in the case of metals and semiconductors [19, 24–27].

The work of this thesis concerns the aforementioned general context. In particular, it aims to investigate the adsorption/desorption of alkali atoms onto various randomly oriented nanopore structures in an Ultra High Vacuum (UHV) regime, the formation of alkali nanoparticles, and the connection between the two effects both of them controlled by an external light source.

The main steps in the realization of the experimental work, as presented in the following, can be summarized as:

1. a preliminary definition of a proper experimental set up; the study of the main processes as a function of the UHV chamber parameters, such as the pumping efficiency;

2. the loading of different pore surfaces in UHV regime by using a current controlled alkali dispenser;

3. the adsorption and desorption of the loaded porous sample using different wavelength light sources,

4. the formation of rubidium nanoparticles in the pore distribution induced by an external light source,

5. the desorption of the eventually formed nanoparticles, and the determination of the best configuration in order to optimize the formation rate,

6. the comparison of the measurements in UHV with results of experiments performed in sealed alkali vapor cells.

There is an ample documentation of experimental work concerning light desorption of atoms adsorbed onto different surfaces [11, 28–30]; the measurements presented here have to be considered a preliminary and innovative step for further studies involving the loading of nanostructured surface in a controlled pressure environment, considering the very small literature on this topic.

The use of coherent light sources to control the desorption process and the formation and desorption of nanoparticles takes advantages of two well known light influenced processes: the Light Induced Atomic Desorption (LIAD) and the Surface Plasmon Induced Desorption (SPID) effect. The first one does not require a resonant wavelength and makes the atoms sticked on the pores being desorbed and increasing then the vapor density in the structure. By this trick they become available for aggregation in a more complex system, whose size depends on several physical parameters. The SPID needs an illumination at a wavelength being resonant with a plasmonic frequency in order to "destroy" the previously formed nanoparticles.

The LIAD effect has been widely studied on different substrate and with different atomic species [11, 31–33], in most cases by using vapor cells, where by a mechanical way a porous sample is fixed very close to an optical window. The main advantage of a sealed container is the presence of an "almost inexhaustible" solid reservoir of atoms, which tries to keep constant the vapor pressure at the equilibrium temperature value; the continuous evaporation of fresh atoms makes favourable the loading of the pore surface and hence the amplification in the nanoparticle number induced by an external light source.

On the other hand, the cells show several drawbacks. For example, the atomic density cannot be properly regulated, especially for the species with low vapor pressure[1]. As we have underlined, the progressive capture by the porous sample of fresh atoms makes very difficult to fix an equilibrium: the density is always lower than the predicted thermodynamic value. Moreover, once the cell has been built, it becomes impossible to change either the atomic element or the substrate. Finally, the sealed system forbids a transfer to another setup for further detailed studies. The apparatus built by us and discussed in this thesis would solve these drawbacks and start a complementary method for the study of these dynamical processes involving surfaces, atoms and light. In fact, the loading process can be activated and stopped at will, while the atom source can be easily changed as well as the porous substrate. The use of a UHV chamber also allows for simultaneous acquisition of an optical (fluorescence, absorption) signal and of an electric signal by means of a channeltron, in order to have a both a cross check and a different point of view for the processes on the nanoporous surface.

The interesting part of this work is indeed the possibility to control the atomic

[1] It is possible to heat the atom reservoir to increase the atomic density.

vapor pressure and hence the loading process of the pore structure, ideally, switching on and off the process by turning off the alkali dispenser. The control 1. of the adsorption of atomic species onto a porous structured matrix surface and 2. of nanoparticle formation means, for example, the possibility of creating a support for an optical memory.

.

1.2 Thesis structure

This thesis is composed of six chapters, where each one describes an aspect of the work. The index and the list of the figures are placed at the beginning of the thesis as a quick reference to the various section of the thesis and the results reported in it. At the beginning of each chapter is present a brief summary describing the structure of the same chapter and its section.

An overview of the chapter structure is reported in the following list.

- **Chapter 1 - Introduction:** it is this chapter. It consists of a general contextualization of the work presented in this thesis, a list of the main goals and a brief description of the thesis structure.

- **Chapter 2 - Porous Materials, Adsorption and desorption effects:** The chapter describes the porous material. It focuses in particular on the properties and manufacturing of porous glasses and nanoporous alumina, which are the samples used for the following measurements. It then provides an overview on the adsorption/desorption process of atoms in gas phase on a surface, especially the effect known as Light Induced Atomic Desorption. A description of Light Induced Atomic Desorption effect on a nanoporous surface is given. Finally a microscopic interpretation of the same is provided.

- **Chapter 3 - Optics of nanoparticles :** This chapter is dedicated to the descrition of metal nanoparticles and their interaction with the light and optical response. There will be discussed the Mie and Gans theory for the light scattering by a metal spheroid and the Surface Plasmon Induced Desorption effect will be discussed in the last section of the chapter.

- **Chapter 4 - Experimental apparatus :** In this chapter a detailed description of the various experimental apparatuses is provided. In the two sections that constitute this chapter particular attention is given to the laser light sources exploited for the experimental part and for data acquisition system.

- **Chapter 5 - Experimental results :** This chapter is totally dedicated to the measurements performed on the porous sample and their analysis and interpretation. The chapter is divided into three main sections: the first regarding the porous glass samples, the second the measurements performed on the nanoporous alumina samples, both of them in the UHV chamber, and finally the results obtained by measurements with the spectrophotomer on the porous glass enclosed in the alkali (Na and Rb) vapor cells. The measurements on alumina samples revealed to be particularly satisfactory, especially the ones regarding the thicker sample. An efficient loading of Rb atoms was detected.Under certain conditions, the formation of rubidium nanoparticles was observed.

- **Chapter 6 - Conclusions and outlook :** In the final chapter the main obtained results and conclusions are summarized. It is also reported an overview of the future perspectives and possible continuation of the project considering the obtained results.

Chapter 2

Porous Materials, Adsorption and Desorption Effects

In this chapter the processes involved in the adsorption of atoms onto a nanoporous surface as well as a review of the nanoporous matrices used as a substrate for the alkali atoms will be described.
In Section 2.1 a review of the porous glasses is reported, starting with their fabrication in 2.1.1 and their physical properties in 2.1.2. Section 2.2 deals with the characteristics of the nanoporous alumina layers. In chapter 2.3, the adsorption processes of atoms onto a surface will be described. Finally, Section 2.4 explains the phenomenology of the Light Induced Atomic Desorption, with a special attention to the nanoporous surfaces when used as a substrate (Section 2.4.3), while in 2.5 a microscopic interpretation of the LIAD is given.

2.1 Porous glasses

The term Porous Glass (PG) refers to a large variety of silica derived substrates, characterized by the presence of nanometric or micrometric cavities that propagate throughout their volume. There is a large abundance of different available samples, but most of them have common characteristics.

PGs are constituted by a rigid amorphous glass structure, mainly a borosilicate

glass, with a distribution of pores of different desired size. They are usually manufactured and cut in an easy way. Physical properties of PGs are their intrinsic dielectricity, the resistance to mechanical stress and a high thermal resistance. Moreover, PGs are also almost chemically inert, which makes them particularly well suited as substrates. Because of all these characteristics, PGs are used in a wide range of applications, ranging from fundamental research, such as physics or chemistry, to more applicative fields such as biotechnology, medicine or sensing.

For example, thanks to their porous structure, PGs give excellent opportunities in separating substances, hence they are largely used for gas chromatography [34, 35] or thin layer chromatography [36, 37]. In chemistry or biochemistry, adsorption and separation properties may be required as a preliminary step for further processes, and PGs are a privileged tool for this function [38–40].

In biotechnology, PGs are also used for the immobilization of enzymes [41–43], either by inserting functional groups or by controlling the pore sizes. In fact, they are excellently suited for the synthesis of oligonucleotides whose chain length depends on the pore size of PG [44, 45].

As already stated, PGs are used for sensing application, for example in biochemistry, where water-based solutions are absorbed by Porous Glasses and then optically analyzed by using a wide range spectroscopy [46]. In this latter example, the chemical inertia and the transparency of the PGs, are the key properties these materials are used for.

An example of sensing application of PG is related to pollutant detection: indeed, PGs are exploited as fundamental components of sensors for environmental sciences [47]. In [48], the authors have inserted porous glass in a fiber: they showed a drop in light transmittance when exposed to solvent vapors. The paper reports on, for example, the detection of toluene vapors up to few thousand ppm or of activated charcoal inside cartridges.

The thermal and chemical stability as well as the filtering capabilities make PGs suited for industrial applications as chemical reactor membranes [49–51] or as filtering elements in purification processes [52, 53]. PG membranes are also used for reverse osmosis for sea water desalinization and filtering processes [54–56].

PGs have been used as the main component of the recently developed integrated "lab-on-chip", exploited to measure ionic currents, even from a single molecule or protein [57], for example by using a device constituted by a multiplexed 16 solid state nanopore channels produced by laser assisted capillary pulling [58]. Dielectric metalenses, constituted of 500 *nm* nano-antennas, have also been exploited as an on-chip optical levitation device of nanoparticles in vacuum [59].

Properly modified PGs have been exploites to make use of its photochromic properties for different purposes. The photochromism is the property of a len to get darker under exposure to light of sufficiently high frequency, most commonly

ultraviolet radiation. In the absence of activating light, the lenses return to their clear state again. In ref. [60] researchers modified porous glass plates, with an average pores size of 9 *nm*, by making them interact with molybdenum chloride ($[MoCl_5]_2$). The photochromic property exhibited as progressive blue coloration, when exposing the plates to the UV radiation. The discoloration is obtained by heating the samples in air at 473°C for $\simeq$ 30 min.

Photochromic quartz-like lenses were obtained by impregnating a porous silica glass with a mixture of $Ag/Cu-Hal$ from a water-salt solutions. It was shown that UV radiation causes in these nanoporous samples a luminiscence in a visible part of the spectrum ($450 - 620$ nm) [61]. The different maxima in the luminiscence spectra is due by the the presence of different size silver-containing aggregates [62]. Those modified porous glasses showing photochromic properties can be employed in different applications such as recording and dose meter of UV radiation or in solar concentrators where the presence of Ag nanoparticles in transparent media is required [60, 61].

The process of fabrication of Porous Glass is described in Sec 2.1.1, while in Sec. 2.1.2 a description of the physical properties of porous glass is given.

2.1.1 Manufacturing

There are different routes to build up Porous Glasses depending on which special pore structures are required. The most common method involve phase separation of the silicate and borate phases in such a way that the latter is leached out leaving the typical porous network. The borate is used mainly to lower the melting point of the pure silica (other composite may be involved, such as Na_2O) and thus avoiding the need of high processing temperature [63].

The process by which it is possible to obtain PGs is called near-critical spinodal decomposition [64, 65]: it occurs when a mixture of two or more liquid components separate into different phases when cooled down in a controlled procedure. This brings to a spatial separation of the components forming, then, an interconnected network, whose extension grows in time with a power law [66]. It must be noted that the spinodal decomposition is a completely different mechanism with respect to the nucleation at the glass transition [65]: the decomposition process is governed only by diffusion, hence it happens uniformly throughout the volume [67], thus providing the required homogeneity of the PG sample. On the other hand, the nucleation, since an energy barrier must be overcome, occurs at discrete sites [68].

More in detail, when two components of a mixture occupy similar fractions of a volume, tube-shaped local growth is favored, with a tube radius linear time

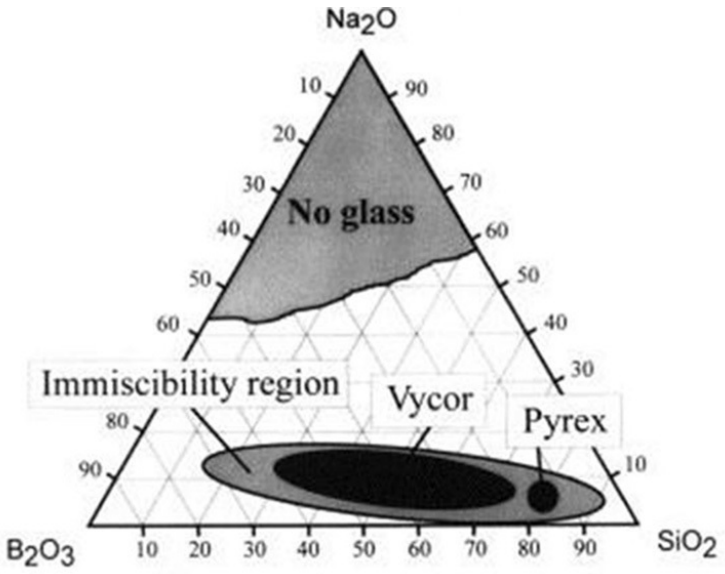

Figure 2.1: Phase diagram for the $Na_2O-B_2O_3-SiO_2$ system [63].

growth [65]. The leading factors affecting the process are the relative viscosity of the fluids involved, the surface tension and the mole fraction of the starting mixture. It is noteworthy that the process does not depend on the chemical features of the starting mixture.

In fig. 2.1, as an example, the $Na_2O-B_2O_3-SiO_2$ system is shown. The bold line divides the glass transition. There is an immiscibility region in the sodium borosilicate glass system, the grey shaded region surrounding the Vycor [1] region that can be separated into phases after appropriate heating treatment [63]. Another commercially used glass, namely the Pyrex, can be obtained by increasing the content of SiO_2 in the mixture at the expense of the B_2O_3 quantity. It is in this zone that spinal decomposition is likely to happen. The key parameters to obtain controlled and determined structures in the final product are the composition of the initial melt, the coooling process, the thermal treatment and the type of the chemical attack.

Taking into account the example reported in fig. 2.1, the initial glass composition is a ternary mixture of SiO_2 (50 - 70%), B_2O_3 (1-10%) and Na_2O[66]. This compound is then heated at about fifty degrees above the glass transition temperature [63, 69], in order to induce phase separation. Then, it is cooled down to a temperature value between 500°C and 750°C, in order to make the spinodal decomposition start and hence to separate the mixture into two phases: one rich in SiO_2 and the other one rich in borosilicate and alkali atoms. It is possible to control the average size of the pores and the extension of the pore network, by tailoring the time of the cooling process. The procedure is schematized in fig 2.2. Once the desired configuration has been obtained, the borate phase is removed by immersing the sample

[1] Vycor is a brand of Porous Glass composed of approximately 96% SiO_2 and 4% B_2O_3, commercially available as Porous VYCOR Glass

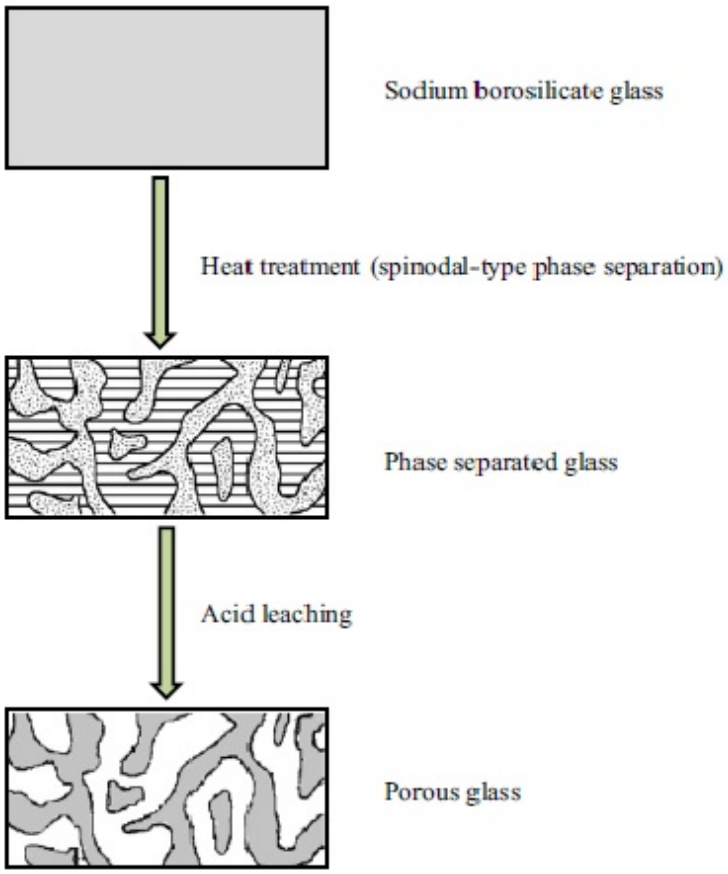

Figure 2.2: Schematic preparation procedure of porous glass [63].

in an acid solution bath at high temperature. An immersion in NaOH is used to remove the residual of colloidal silica. After these cleaning processes, the glass can be handle and cut.

Because of the relatively simple dynamics of the spinodal decomposition, the process can be modelled as a purely diffusion problem. There are several simulations of the growing PG [65, 66] based on relatively simple models. In fig. 2.3 a realistic simulated growing process of a binary mixture is reported, where the light-grey spheres represent the silica-rich phase. For this simulation the mixture has been modelled by spherical particles of identical size with a Lennard-Jones intermolecular potential. The average domain size grows as $\sim t^{1/2}$ while the consequent excess of potential energy of the system decreases as $\sim t^{-1/2}$. The desired average pore size can be tailored by stopping the quenching process induced by the cooling at a specific time, as shown in fig. 2.3.

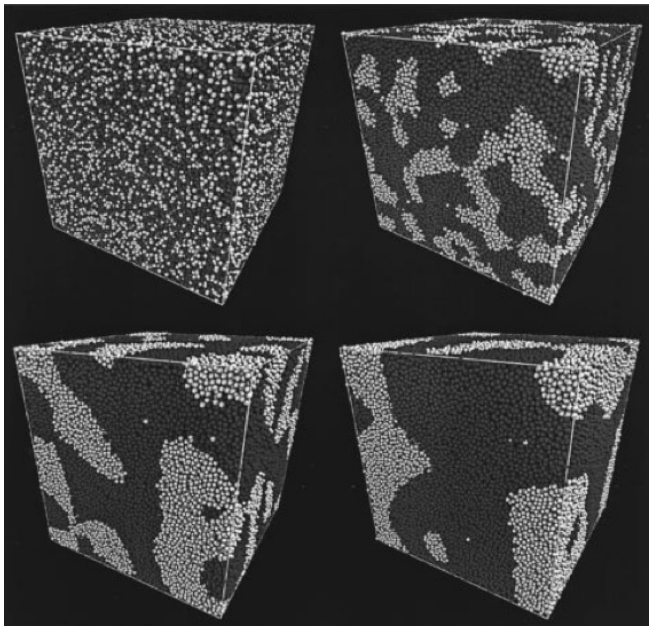

Figure 2.3: Simulation of the spinodal decomposition for a PG from a binary mixture, the light gray spheres reprensent the silica-rich phase.*Top left*: starting point, 0 time steps. *Top right*: 75 time steps, average pore size 2.11 nm. *Bottom left*: 225 time steps, average pore size 3.71 nm. *Bottom right*: 450 time steps, average pore size 5.74 nm [66].

2.1.2 Properties

The samples of Vycor7930 used in this work contain mostly SiO_2 (96%), B_2O_3 (3%), Na_2O (0.4%) and traces of other compounds. The Vycor7930 sample has a specific surface area of 250 m^2/gr and a porosity, defined as the ratio between the volume occupied by the pores, $\mathcal{V}_{free}$, and the whole sample volume:

$$\mathcal{P} = \frac{\mathcal{V}_{free}}{\mathcal{V}_{sample}} = 28\% \tag{2.1}$$

The sample is shaped in disks of $10mm$ in diameter and $2mm$ thick, hence having a volume:

$$\mathcal{V}_{sample} \simeq 157mm^3 \tag{2.2}$$

and an average pore size of $4nm$. The surface appears smooth and almost transparent to the naked eye.

The volume occupied by the pores, that is the free available volume, can be simply evaluated by using eq. 2.1:

$$\mathcal{V}_{free} = \mathcal{V}_{sample} \times \mathcal{P} \simeq 44mm^3 \tag{2.3}$$

The equivalent surface can be roughly estimated, assuming for simplicity the pore having a cylindrical shape and a radius equal to the size of the pores, as:

$$\mathcal{S}_{equiv} = \mathcal{S}_{pores} \times \mathcal{N}_{pores} \tag{2.4}$$

where

$$\mathcal{N}_{pores} = \frac{\mathcal{V}_{free}}{\mathcal{V}_{pores}} \tag{2.5}$$

which gives a result of $\mathcal{S}_{equiv} \approx 220m^2$.

The second sample is a PG of porous silica (SiO_2) disk of $30mm$ in diameter and $3mm$ thick, with a volume of $\sim 2.120\text{mm}^3$ and with an average pore size of $200nm$. Due to the larger pore size with respect to the Vycor7930, this sample appears more whitish when exposed to the room light; the light scattering caused by the air/glass interface becomes more efficient. This is also an indirect proof of the presence of the nanometric pores with size of the order of the visible wavelength.

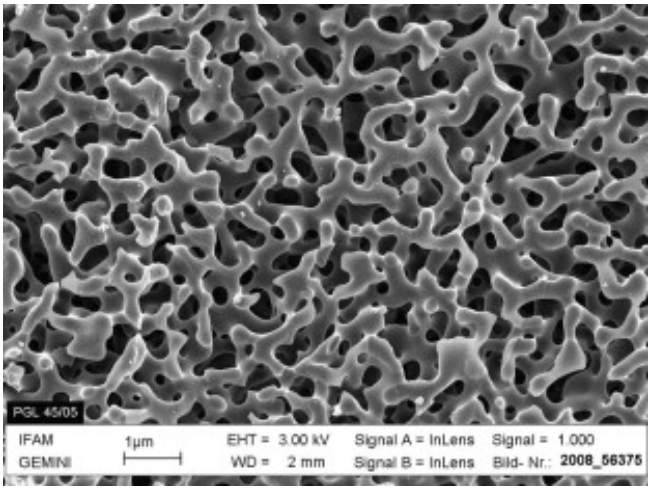

Figure 2.4: Scanning electron micrograph (SEM) of a Controlled Porous Glass showing the size distribution of the continuous interconnected glass matrix [70].

Other measurements have been performed on two rectangular shaped PGs, mechanically fixed in cylindrical vapor cells where an alkali reservoir refurbishes the vapor phase. The two cells contain either Na or a natural mixture of Rb. The PG in the Na cell is known as TRISOPLAC and is produced and commercialized by Vitra-Bio GmbH, while the PG in the Rb cell was produced by the laboratory at the Saint Petersburg National Research University of Information Technologies, Mechanics and Optics (ITMO).

In order to measure the pore size a porosimetry technique has been exploited; it makes use of high pressure Hg injected in the pores, in order to determine the average diameters of the pores. The results are reported in fig. 2.5 and show a pore size of 20 nm. The declared free volume percentage is 55% and the whole sample

volume is $13\text{mm} \times 14\text{mm} \times 1\text{mm} = 182\text{mm}^3$.

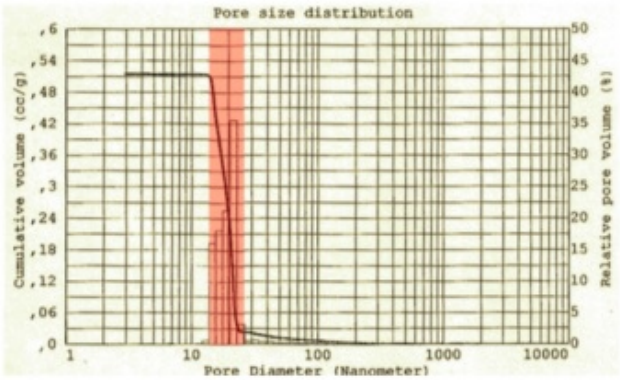

Figure 2.5: Pore size of the TRISOPLAC PG [71]. The red area indicates the 95% of pores population.

The PG in the Rb cells has, instead, an average pores size of $17nm$ and dimensions of $30\text{mm} \times 15\text{mm} \times 1\text{mm} = 450\text{mm}^3$ while the porosity is the 53%, as declared by the Russian researchers. By making use of eq. 2.3, it results a free volume of $\mathcal{V}_{free} = 101.1mm^3$ for the TRISOPLAC, while $\mathcal{V}_{free} = 238.5mm^3$ for the PG in the cell filled with Rb. Using instead eq. 2.4, the equivalent surface for the TRISOPLAC PG results $\mathcal{S}_{equiv} \approx 20m^2$ while it results $\mathcal{S}_{equiv} \approx 50m^2$ for the PG in the Rb cell.

Components	percentage
SiO_2	96 %
B_2O_3	3 %
Na_2O	0.4 %
ZnO_2 and Al_2O_3	< 0.1 %

Table 2.1: Chemical composition of the PGs [72].

In tab. 2.1 the chemical composition of the PGs discussed in this section is reported. Traces of oxydes as ZnO_2 and of others compounds are due to the acid leaching process.

Another tool for the analysis of the PGs samples is the Transmission Electron Microscopy (TEM) technique. In fig 2.6, two original pictures, fig. 2.6a and fig. 2.6b with different magnification and scale bar respectively of 100 nm and 20 nm, taken by the instrument at Dipartimento di Scienze Fisiche , della Terra e dell'Ambiente - sezione di Geologia is shown (courtesy of Cecilia Viti). The image confirms a random spatial pore distribution with pore size diameters of about $20nm$, as known by the company data sheet. TEM is not applicable to alumina, as the sapphire substrate cannot be properly reduced at the desired thickness by precision ion polishing system, which consists of an Ar ion beam accelerated by an initial voltage of 5 kV and an incident angle $\theta = 25°$. The hardness of the the sapphire substrate is indeed too high: the sample should be destroyed during the operation.

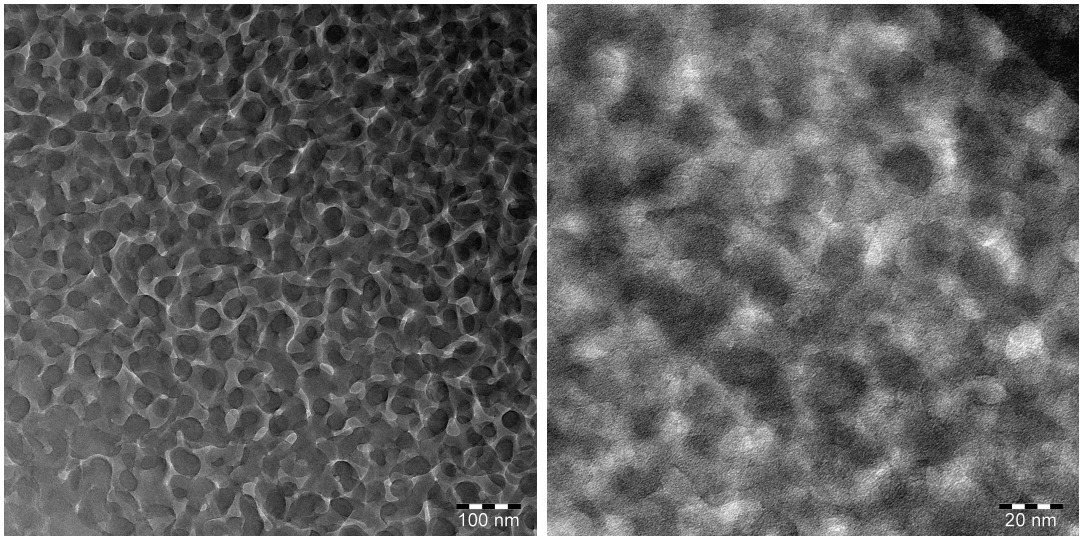

(a) **(b)**

Figure 2.6: TEM images of an amorphous nanoporous structure with pores dimension comparable to the alumina samples examined at two different magnification. **(a)** Scale bar of 100 *nm*. **(b)** Scale bar of 20 *nm*.

At the end of section 5.2.1, there will be showed Scanning Electron Microscopy (SEM) images, taken by the instrumentation at Dipartimento di Scienze Fisiche , della Terra e dell'Ambiente - sezione di Geologia as well, of the 300*nm* alumina sample after the Rb deposition.

2.2 Alumina

Aluminium oxide, commonly known as alumina, is a compound, whose stoichiometric formula is Al_2O_3, known since the beginning of XIX^{th} century. In nature, it is found in its crystalline polymorphic phase α-Al_2O_3, which is indicated as corundum, and can have differents gem varieties due to the presence of impurities in the crystalline structure, such as ruby, where the red color is due to the presence of chromium impurities.

The crystalline structure of α-Al_2O_3 can be seen as an hexagonal close packing of oxygen ions, in which $2/3$ of the octahedral interstices are filled with aluminium cations [73]. Two views along different axis direction of the corundum crystal structure are reported in fig. 2.7.

Alumina is an electric insulator but shows a quite high thermal conductivity ($30 Wm^{-1}K^{-1}$) for a ceramic material [74, 75]. Usually, alumina is extracted from the *bauxite*, the main source for the production of aluminium, even if it contains only

the 30-54% of Al_2O_3. In fact, bauxite is composed of a mixture of minerals such as gibbsite ($Al(OH)_3$) and böhmite (γ-AlO(OH)), along with other impurities of iron oxides, silica (SiO_2) and titanium oxide (TiO_2) [76].

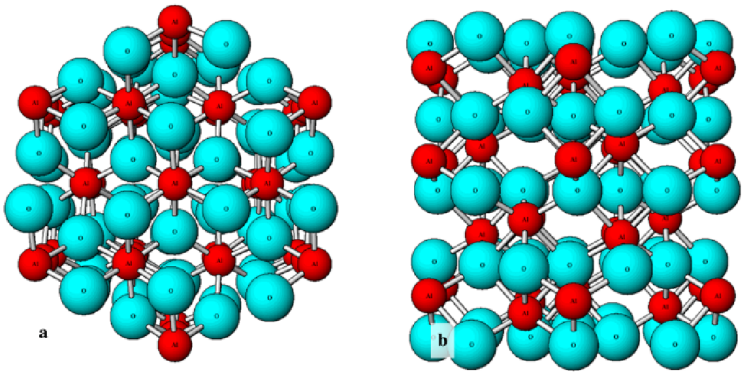

Figure 2.7: The α-Al_2O_3 crystal structure viewed along, (a) the $< 0001 >$ direction ("c" plane) and (b) the $< 10\bar{1}0 >$ direction. Blue and red spheres represent, respectively, oxygen atoms and aluminum atoms [77].

In order to purify the bauxite to obtain the alumina, the Bayer process is used. The scheme of the process is reported in fig. 2.8.

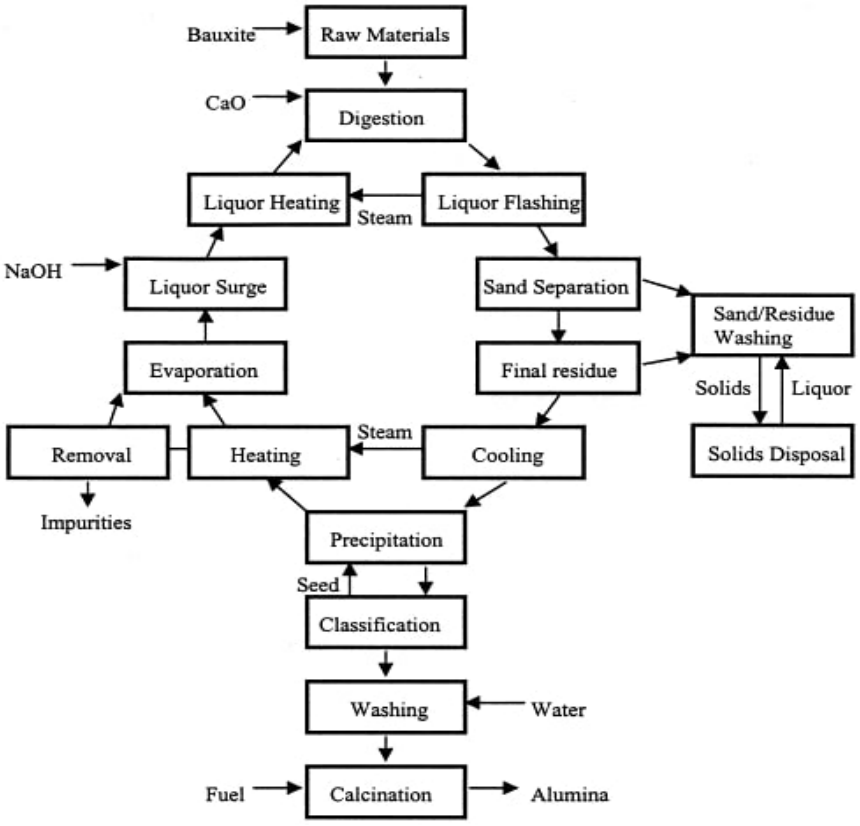

Figure 2.8: Schematic representation of the Bayer process [78].

The first step is to heat the bauxite along with sodium hydroxide (NaOH) bath at 270°C in order to dissolve the majority of species containing aluminium and to obtain the sodium aluminate ($Na^+[Al(OH)_4]^-$) according to the reactions:

$$Al_2O_3(aq) + NaOH \xrightarrow{\triangle} Na^+Al(OH)_4{}^-(aq) \tag{2.6}$$

and

$$Al(OH)_3(s) + NaOH(aq) \xrightarrow{\triangle} Na^+Al(OH)_4{}^-(aq) \tag{2.7}$$

These reactions leave an insoluble residue (*red mud*), composed primarily of iron oxides, quartz, sodium aluminosilicates, calcium carbonate/aluminate and trace of titanium dioxide, which is removed by settling/filtration.

The next step consists in a cooling process during which the $Al(OH)_3$ precipitates, essentially reversing the dissolution reaction 2.7, as described in the following reaction:

$$Na^+Al(OH)_4{}^-(aq) \longrightarrow NaOH(aq) + Al(OH)_3(s) \tag{2.8}$$

Finally, the $Al(OH)_3$ is calcined (heated to over 1100 C°) to give aluminium oxide:

$$2\,Al(OH)_3(s) \xrightarrow{\triangle} Al_2O_3(s) + 3\,H_2O \tag{2.9}$$

The reactions for the extraction process occur almost entirely at the solid/liquid interface [78].

Alumina is nowadays used in different fields like nanosciences [79, 80], engineering applications [81] and fundamental physics [82, 83].

Alumina can also be processed in order to obtain nanoporous structures; one of the methods used to achieve this goal is the so-called Electron Beam Physical Vapor Deposition (EBPVD), a technique which belongs to a class of deposition techniques called Physical Vapor Deposition (PVD). This procedure will be described more in details in the following section.

2.2.1 Nanoporous Alumina Layer Manufacturing

Two samples of *porous alumina* have been used. The samples have been prepared by the researchers of the PhysNano laboratory at the Saint Petersburg National Research University of Information technologies, Mechanics and Optics (ITMO) using a PRO line PVD 75 of the Kurt J. Lesker company, a versatile device allowing for three different types of PVD: the Magnetron Sputtering, the Thermal Evaporation Deposition and the Electron Beam Vapor Deposition. Generally speaking, the

EBPVD consists on a bombardment of a target anode with an electron beam, generated by a charged tungsten filament under high vacuum condition. The electron beam makes the atoms in the target passing from solid phase to vapor phase and allowing for a coating of the surface available in the vacuum chamber with a thin layer of the target material, which can be in the form of a disk, rod or an ingot.

The pressure in the vacuum chamber must be at least of 10^{-5}mbar in order to maximize the mean free path of the electrons from the electron gun to the target, as well as to avoid contamination from other compounds [84]. A hot filament causes the thermionic emission of electrons, which can, after accelerated by a potential difference, provide sufficient energy for evaporating any material. In a typical case involving 1 A current on the emission filament and the beam accelerated through a 10 kV voltage drop, 10 kW is delivered upon impact [85]. The filament is located out of sight of the target as shown in fig. 2.9 and the electron beam is pulled around to the surface by a magnetic field, **B**, directed perpendicularly to the eletronc beam trajectory. The force acting on the electrons is the combination of the electric force, $\mathbf{F}_E$, and the magnetic force, $\mathbf{F}_B$, in the well known Lorentz force:

$$\mathbf{F} = \mathbf{F}_E + \mathbf{F}_B = q(\mathbf{E} + \mathbf{v} \times \mathbf{B}) \tag{2.10}$$

The radius of the circular motion of the electrons r_g, known as gyroradius, is:

$$r_g = \frac{m_e v_\perp}{|q|B} \tag{2.11}$$

where m_e is the electrons mass, $v_\perp$ is the component of the velocity perpendicular to the direction of the magnetic field and B is the strength of the magnetic field.

When hit the target material, the electrons will lose their energy very rapidly.The kinetic energy of the electrons is converted into other forms of energy through interactions with the evaporation material. The thermal energy that is produced heats up the evaporation material causing it to melt or sublimate [86]. Once temperature and vacuum level are sufficiently high, vapor will result from the melt or solid. Once a gaseous phase is obtained, the vapor can be used to coat surfaces. In fig. 2.9 is shown a scheme of the EBPVD apparatus.

In the case of alumina deposition, the layer must be undergo an annealing process at temperatures between 400°C and 1130°C, in order to allow the transition from amorphous to crystalline state [87]. In ref. [88] the electron beam is obtained by a current flow of 50 mA and accelerated by a potential of 4.2 kV and the system is maintained at a pressure of $5.7 \cdot 10^{-6}$mbar.

The vapor obtained may contain both molecules and cluster of aluminium oxide. After the deposition, techniques like the X-Ray Diffraction (XRD) can be used to analyze the structural properties of the film [88].

EBPVD technique has been used for the deposition of our samples [87], which

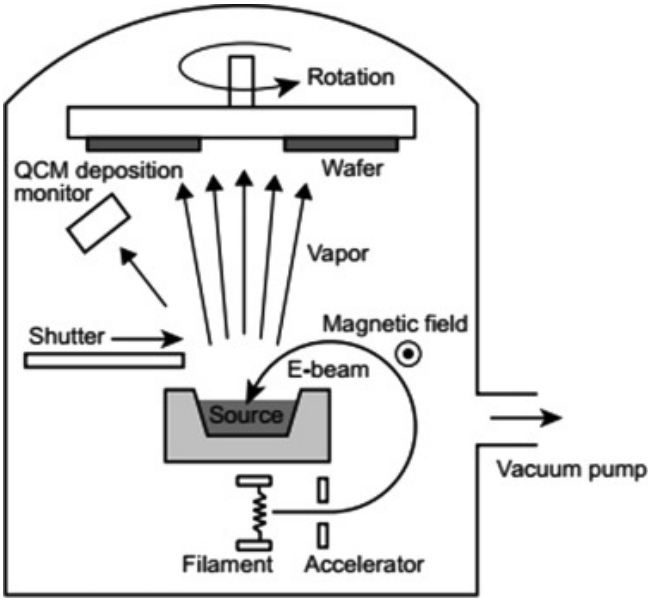

Figure 2.9: Schematic of the Electron Beam Physical Vapor Deposition Technique [85].

consist in a thin layer of alumina on a disk-shaped substrate of 30*mm* diameter and 2*mm* thickness of sapphire (α-Al_2O_3), with the c-axis oriented perpendicular to the substrate surface. However, due to technical issues, the alumina layer does not fill the whole sample in the radial coordinate, and its limit stays 1.3*mm* apart from the edge of the substrate. Therefore, the active part of the sample has a diameter of 27.4*mm* and covers a surface of about 590 mm^2.

The two samples have alumina layers of different thicknesses, roughly 300*nm* and 100*nm*, and a declared pore size of about $20-30nm$ [20]. In order to measure the deposition rate ($\text{Å}/s$), an oscillating quartz crystal has been used. The thickness values are deduced by the deposition rate.

A spectrophotometer, both in S. Petersburg and in Siena, has been used as a tool for the post deposition analysis of the samples. The system measures the absorbance, or optical density (OD): it is commonly defined as the logarithm of the ratio of intensity of the incident light I_i to the intensity of the transmitted beam I_t:

$$OD = \ln \frac{I_i}{I_t} \tag{2.12}$$

In fig. 2.10 the black curve shows a typical spectrophotometer result for a thin film alumina sample on a sapphire substrate, as obtained at ITMO. The red curve is a theoretical line calculated with the following modelling. A transfer matrix method has been applied by the ITMO colleagues. It is used to estimate the refractive index of the porous film considering the refraction of the light from air, in the porous Al_2O_3

and then into the sapphire substrate:

$$\text{Light} \rightarrow \text{Air (n = 1.0)} \rightarrow Al_2O_3\text{(n = n.d.)} \rightarrow \text{Sapphire (n = 1.76)}$$

where the values of the refractive have been taken from [89]. For example to best fit the experimental result, in the case of a sample of 300 nm thickness (not the sample used for this thesis work), according to the quartz crystal microbalance measurement, the value of thickness was set to 190 nm and the refractive index was reduced by 0.05 to take into account the porosity of the film. In fig. 2.10 is reported the result of the fitting: From this theoretical model, it is possible to say that the layer of porous

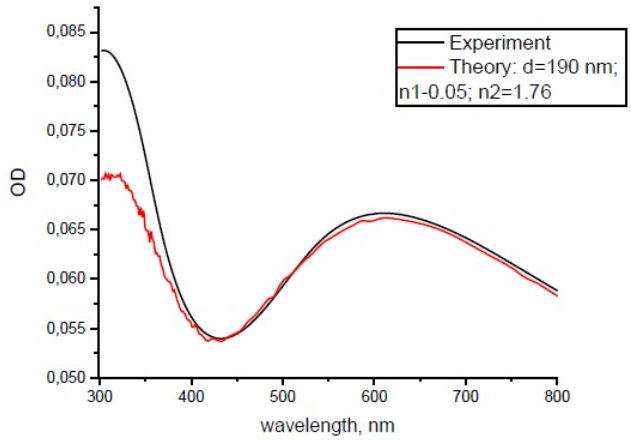

Figure 2.10: *(red line)*: best fit for the optical density of Al_2O_3 film, *(black line)*: experimental result

alumina is about 190 nm and, from the refractive index value, the porosity is of the order of 3% ($0.05/1.76 \simeq 0.028$).

Using this value of porosity, it is possible to simply evaluate the available volume in the porous alumina as:

$$V_{free} = \pi \cdot r^2 \cdot h \cdot 0.03 \tag{2.13}$$

in such a way that the free volume results $V_{free} = 5.31 \cdot 10^{-3}\, mm^3$ and $V_{free} = 1.77 \cdot 10^{-3}\, mm^3$, respectively for the $300nm$ and $100nm$ samples.

The same kind of spectra has been recorded for the alumina samples used in this work, in order to better understand how the optical density of the sapphire is affected by the presence of two different thickness layers of alumina.

In fig. 2.11 the OD spectrum of both the alumina samples and the sapphire disk obtained with our spectrophotometer is shown. Further details of this instrument will be given in sec. 4.1. The black line, which corresponds to the absorbance of the sapphire substrate alone, shows an almost flat trend in all the visible part of the spectrum, up to the UV region where it becomes more opaque to the light.

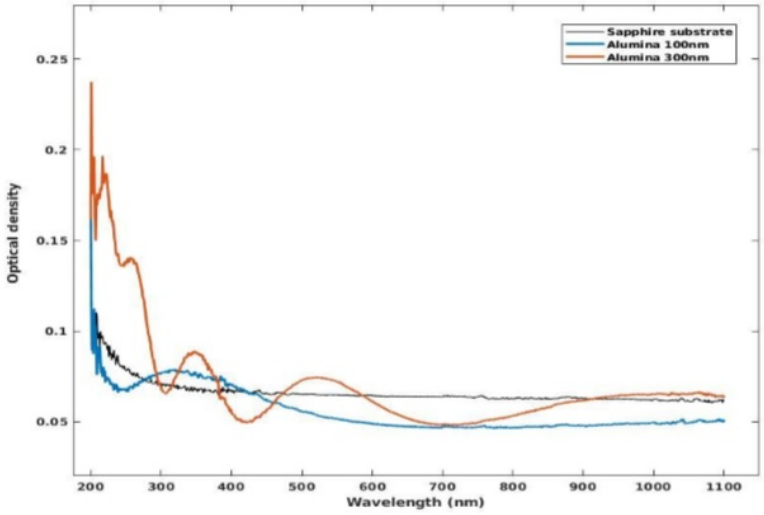

Figure 2.11: Plot of the Optical Density of the 300 nm sample *(orange line)*, 100 nm sample *(blue line)* and the sapphire disk *(black line)*

In the other cases several peaks appear, due to the presence of the alumina layer. The intensity and the number of the peaks in the spectrum increases with the layer volume, i.e. with layer thickness. In particular, the blue line, corresponding to the 100*nm* thickness, presents only one broad peak centered at about 330*nm* and a plateau toward the infra-red zone of the spectrum. On the contrary, the sample with a thickness of 300*nm* shows an oscillating behaviour with peaks of different amplitudes in the UV region of the spectrum, a sharper peak in the same region of the thinner sample and also presents a broad peak around 540 nm. A possible interpretation of these spectra has been given in ref. [90], as due to an interference pattern in the transmitted light amplitude overlapped to the transmission response of the substrate, as can be seen in the fig. 2.12, where different transmitted and reflected spectra in the range of $190 - 820nm$ of AlN films are reported. The oscillating behavior of our samples should therefore be related to the thickness of the Alumina layer: thicker layers obtain a higher wavelength frequency oscillation. By this interpretation it should be possible to give an estimation of the ratio of the two thicknesses.

In order to obtain information on the crystollagraphic purity of the sample and also how and if the nanoporous deposited film modifies the diffraction pattern, X-Ray diffraction measurements have been performed on the NP alumina sample with a thickness of 300 nm after the Rb deposition process. The X-Ray diffraction measurements have been performed at *Dipartimento di Scienze della Terra* of University of Pisa. In fig. 2.13 the X-Ray diffraction pattern of the 300 nm alumina sample is reported.

Three measurements have been performed: the first one has been obtained exposing the substrate side to the X-Ray, then the same measurement has been maded

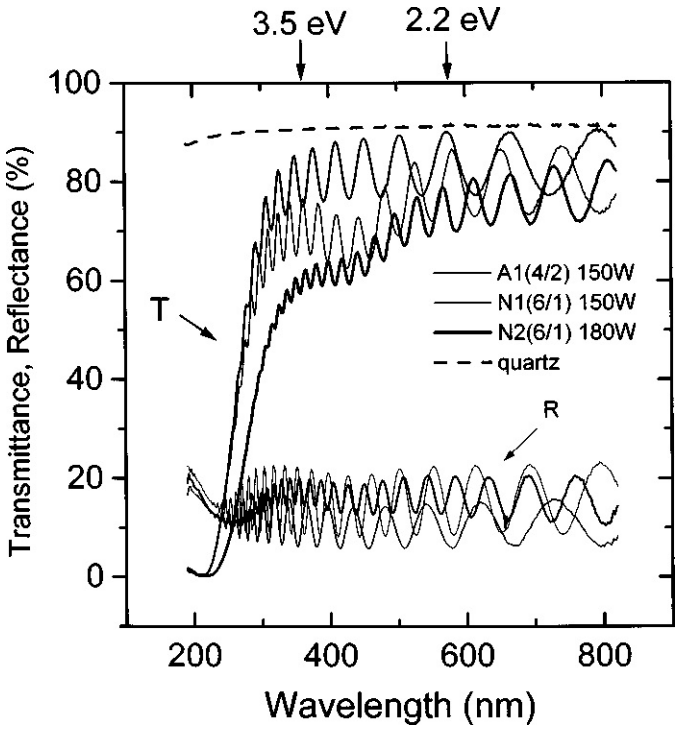

Figure 2.12: Transmittance and reflectance spectra of AlN films showing various absorption features [90].

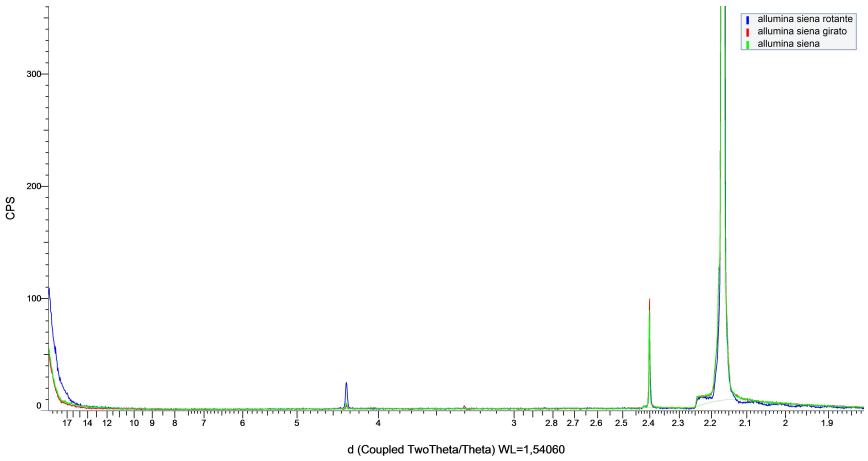

Figure 2.13: X-ray diffraction pattern of the 300 nm alumina sample.*(green line):* measurement performed on the substrate side, *(red line):* measurement performed on the NP alumina film side, *(blue line):* measurement performed with the rotating sample.

on the nanoporous alumina sample and the last X-Ray diffraction measurement was performed with the rotating sample. The nanoporous film presents an amorphous structure, hence the main expected effect on the diffraction pattern is to broad the peaks due to the crystal structure of the α-Al_2O_3. However, as can be seen in 2.13, the three lines are pratically overlapped; only the peak of the blue line at $\theta = 4.3°$ shows a remarkable increase in amplitude.

The reason why it is impossible to see a broadening of the peaks, is likely due to the fact that the deposited alumina film is too thin to be appreciated by the X-Ray. The penetration depth , which is defined as the length at which the intensity radiation inside the material falls to $1/e$, in alumina is expected to be in the range between some μm and tenths of μm [91], depending on the beam incident angle and X-ray beam energy, hence it is possible to affirm that the X-ray beam is not affected by the presence of the 300 nm nanoporous film.

2.3 Adsorption and desorption processes

The term *adsorption* refers to a complex series of phenomena that make possible to a particle (an atom, an ion or a molecule from a gas, a liquid or a solid phase) being captured by a surface in a different phase. It is a characteristic of the interfaces, then it is mainly governed by the surface energy balance [92].

The adsorption phenomena take place at a close range distance, that means distance of the order of the external radius of the adsorbed particle. This may change the internal degrees of freedom of the particle because of the high inhomogeneity of the surface potentials. Therefore, it can be expected a change in the response of the adsorbed particle to an external excitation, such as a red-shift of the energy levels [93, 94].

There are two fundamental classes of adsorption, depending on the energy range involved in the process and the type of interaction between the particles [68]:

- **Physisorption:** the adsorbed particle interacts with the surface by weak Van der Waals forces with an interacting energy of $\sim 10 - 100$ meV. The attractive force is due to correlated charge fluctuactions in the two bonding partners. The adsorbed particle can diffuse on the surface and can be detached from the surface with relatively low energy.

- **Chemisorption:** the adsorption process is characterized by the formation of covalent or ionic bonds. The electronic structure of the adsorbed particle is strongly perturbed and cannot be distinguished by the substrate. The energy involved is of the order of some eV up to tens of eV.

Because of the two different forces involved, the two processes correspond to different interaction times: in the chemisorption the particle may lie in the adsorption site indefinitely. In the case of the physisorption, instead, the contact interaction is produced for a short time, defined as the sticking time, and then the particle is naturally released.

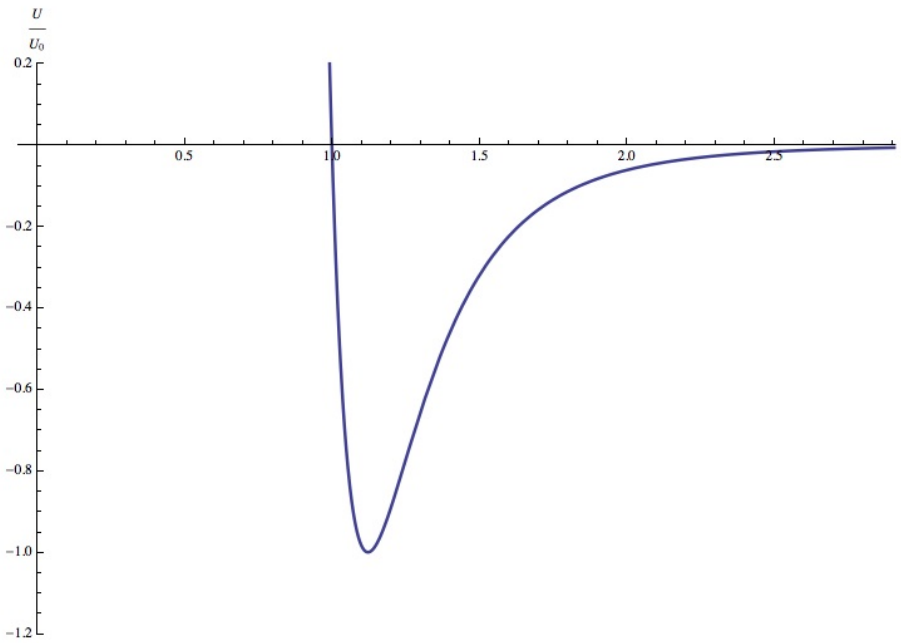

Figure 2.14: Lennard-Jones potential (Eq.2.14) normalized to the potential wall depth U_0 [95].

From now on, because of the interest in the photodesorption process of this work, only the case of the physisorption will be treated in detail.

The van der Waals interaction involves forces between permanent electric dipoles (Keesom forces), between a permanent and an induced electric dipoles (Debye forces) and between two mutually induced dipoles moment (London dispersion forces) and to the Pauli repulsive force, due to the exclusion principles.

The first successful description of the van der Waals forces was the Lennard-Jones potential:

$$U(r) = \left(\frac{b}{r}\right)^{12} - \left(\frac{a}{r}\right)^{6} \tag{2.14}$$

where the two terms on the right side refers respectively to a short distance repulsive force ($\sim r^{-12}$), arising from an overlapping of the electrons wavefunctions, and to a long range attractive potential ($\sim r^{-6}$). As shown in fig. 2.14, at long distances (few Å) the attractive term dominates, in such a way to allow for the formation of the weak bonding between the surface and the adsorbed particle.

More in detail, in the physisorption, when an atom interacts with a dielectric surface, the interaction is due to a mirror dipole at the surface induced by the adsorbed particle instantaneous dipole, hence the process can be described by the London force previously mentioned. This is true also for particles with no electric dipoles, like alkali atoms [96]. In fact, in a neutral atom, an external electric field **E**

can induce an instantaneous dipole by displacing the center of the charge distribution. Hence an induced electric dipole is generated:

$$\vec{P}_{ind} = \alpha(\omega)\vec{E}_{ext} \tag{2.15}$$

with α the polarizability of the atom, that, in general, depends on the frequency.

Hence, the term $\sim r^6$ of the eq. 2.14 is due to the mutually induced deformation of the electronic cloud; in fact one dipole p_1 formed by charge fluctuations induces an electric field $\varepsilon \propto p_1/r^3$ at the site of the other molecule at a distance r. The induced dipole moment is $p_2 \propto \alpha p_1/r^3$ [68], then the potential of this dipole p_2 in the field of the first dipole is proportional to ε and to p_2: this is the reason for the r^{-6} dependence in the 2.14. The interaction energy between two atoms whose mass centers are separated by r is [92]:

$$U_{int} = -\frac{3}{2} \cdot \frac{\alpha_1 \alpha_2}{(4\pi\varepsilon_0)^2} \cdot \frac{I_1 I_2}{I_1 + I_2} \cdot \frac{1}{r^{-6}} \tag{2.16}$$

where $I_{1,2} = h\nu_{1,2}$ are the first ionization energies and $\alpha_{1,2}$ the polarizabilities of the two atoms.

It must be noted that such forces are responsible not only for the physisorption of non-polar particle onto a dielectric surface, but are also responsible for other phenomena, like the liquefaction of noble gas [97].

2.3.1 Atomic adsorption from gas phase

There is a certain probability (approximately between 0.3 and 0.6 [98]) that an atom in gas phase, when hits a surface, interacts with the same and sticks on it if energetically favorable. For a full understanding one must take into account even the diffusion of the adsorbed particle at the interface. Mechanism like that are exploited, for example, in deposition process like the epitaxy [99]. However, while the process goes on, the available adsorbing sites saturate, hence the adsorption probability will drop down. So, when there are not anymore available adsorbing sites, at the interface it will be present a layer of adsorbed atoms that prevents further adsorption on the surface [2].

Considering pure elastic interaction between the atom and the surface, the sticking time coincides with the interaction time and it is of the order of $\tau_0 \approx 10^{-12}s$. The average time spent by an atom on the surface is proportional to the local adsorption energy E_a, which is defined as the kinetic energy needed for an atom to escape the

[2] In general a growing process does not imply the formation of an ordered crystalline structure

van der Waals force:

$$\tau_s = \tau_0 \cdot e^{E_s/k_B T} \tag{2.17}$$

where $k_B T$ is the average thermal energy, τ_0 is the interaction time. In the case of physisorption E_a can range between few meV for light gases atoms up to eV [3] for heavier organic molecules [97]. Because of the relatively low binding energy, the adsorbed atoms maintains a certain degree of mobility on the surface, accordingly with the surface local potentials.

For a more realistic modeling, it is possible to consider a local variation, on length scales of the order of the atomic size, of the adsorbing energy: $E_a = f(\mathbf{d})$, where $\mathbf{d}$ is the vector position on the surface. This assumption has two consequences:

1. the adsorption coverage on the surface is not uniform,

2. the energy needed for an atom to move from a site $\mathbf{d_0}$ to a site $\mathbf{d_1}$ is of the order of $E_a(\mathbf{d_0}) - E_a(\mathbf{d_1})$.

In steady state conditions, the Langmuir equation gives an estimation of the surface atomic density. Defined the sticking time as:

$$\sigma = \frac{n}{4} v_{th} \tau_s \tag{2.18}$$

where n is the atomic gas density and $v_{th} = v_{rms} = \sqrt{\int_0^\infty v f(T,v) v}$ is the mean thermal velocity of a gas with a Maxwell-Boltzmann distribution. For example, for a vapor of potassium atoms at T = 300K, $v_{th} \approx 438 m/s$.

For what concerns the physisorption from gaseous phase, this phenomenon has a relevant consequence: the adsorption process implies the thermalization of the adsorbed species with the adsorbing surface, and then, atoms diffusion on the surface is energetically unfavorable. In fact, the average kinetic energy quickly becomes of the same order of the energy difference between two neighbour sites on the surface. However, interaction with light may enhance the mobility of the adsorbed atoms.

Photodesorption from organic compounds is also used to obtain large alkali vapor density in nanometric volumes, like hollow core photonic band-gap fibers [100] and also it turned out to be the only technique to obtain large enough atomic density for non-linear optics in fiber structures without damaging it [101, 102] .

[3] Typically binding energies involved in chemisorption are of the order of some eV [68]

2.4 Light Induced Atomic Desorption

The Light Induced Atomic Desorption effect (LIAD) [103] is a non-thermal, non-resonant process due to the exposure of adatoms stuck on a dielectric surface to IR - visible - UV light, even if non coherent and low intensity. The illumination produces a sudden release of the adsorbed atoms, increasing the atomic vapor density up to several orders of magnitude above the thermal equilibrium at room temperature [104].

The first evidence of LIAD was obtained in 1993 by [31] in a polydimethylsiloxane (PDMS) coated Pyrex cell filled with Na vapor: a very intense fluorescence of the sodium D_1 line was observed at room temperature (when the sodium density is very low) for a resonant dye laser beam crossing the cell. In 1994 the same effect was observed in PDMS coated cells with Rb vapor [103].

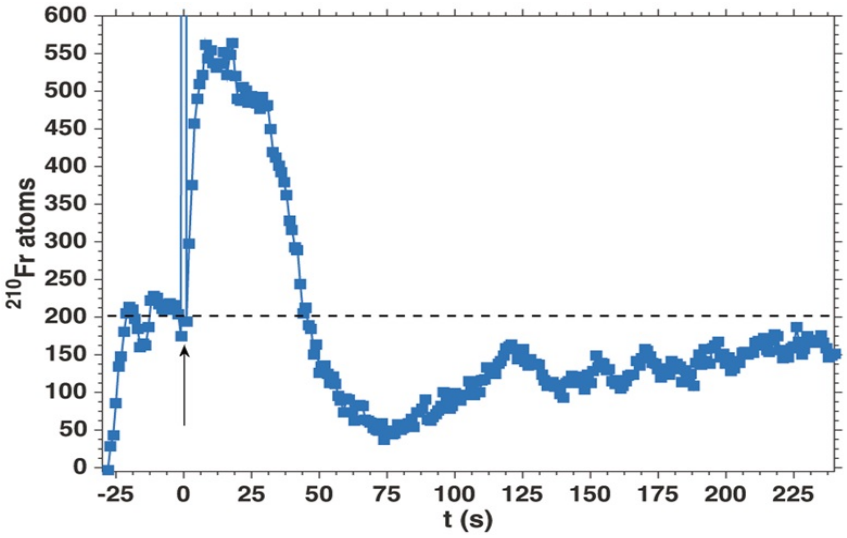

Figure 2.15: Time evolution of ^{210}Fr MOT population after a broadband light pulse, indicated by the arrow mark, at $t = 0$ s.The horizontal dashed line indicates the equilibrium population [105].

Since then, the LIAD effect was studied from PDMS coated cells with Rb and Cs [33, 106–108], Na and K [108–110] with K, Rb and Cs from bare borosilicate glasses [26, 111–113], from octamethylcyclotetrasiloxane (OCT, $[(CH_3)_2SiO]_4$) coated cells with Cs [114], from dry film coated cells [29] and from porous alumina with Rb [11]. It is worth to say, that in the case of PGs, the large surface/volume ratio, compensates the much lower desorption efficiency with respect to conventional organic coatings, due to the higher adsorption energy of uncoated glasses.

LIAD effect is in general used when an increase of atomic density is required, for example, it has been used in microfabricated vapor cells (in the scale of mm and lower) to increase the atomic vapor density in order to overcome the problem of the

reduced optical path [115]. LIAD effect is also exploited for the loading of Magneto-Optical Traps (MOTs)[116, 117], even with Fr atoms [105] and also to improve the loading and transport efficiency for the Bose-Einstein Condensation [118, 119].

In fig. 2.15 is reported the result for LIAD in the case of a ^{210}Fr MOT, where the population variation is continuosly monitored by the fluorescence produced by the MOT. The population at the equilibrium, indicated by the dashed line, is of about 200 atoms. The LIAD effect is triggered by a broadband light pulse of 2 ms duration. The energy carried by the photons induces a release of adsorbed atoms generating a net flux towards the vapor phase of Fr atoms which are then cooled and trapped in the MOT. By means of LIAD effect, the population of trapped ^{210}Fr atoms increase up to 570 with a relative increase of 190 % [105].

Just for completeness, it must be said that LIAD effect takes place also on not dielectric surface, like in the case of Rb and K from stainless steel [120] or Cs from aluminum [117].

2.4.1 LIAD phenomenology

Beside the dynamics of the Light-Induced Atom Desorption are strongly dependent on the characteristics of the system under investigation, some general features can be outlined.

LIAD is a non-thermal effect, since the desorption rate scale laws are completely different from the typical heating process behaviors. For example, the number of desorbed atoms does not grow exponentially with the intensity of light [103]. On the contrary, at lower temperatures, the density yield is enhanced, since, in this condition, the sticking probability of the vapor phase atoms on the substrate is favoured.

The effect of light-induced desorption, from the discussion in sec. 2.3, is clearly linked to the physisorption only [103]. In general, the effect of the light is the break of the van der Waals bonds between an adsorbed atom and the surface; the previous dynamical equilibrium is moved, as the action of light is contrasted by the continuous adsorption of fresh atoms refurbished by the reservoir [121]. Therefore, the effect of the light is to increase the average atomic mobility [33]. The macroscopic consequence is a sudden release of the adsorbed atoms in the vapor phase, drastically increasing the vapor density.

The gain in density can even exceed the equilibrium by several orders of magnitude, but just for a short time interval, because of the progressive depletion of the substrate [109, 121, 122]. Indeed, in presence of an "infinite" source of atoms, during the illumination, the process will tend to the thermal equilibrium between the adsorbed and desorbed atom fluxes.

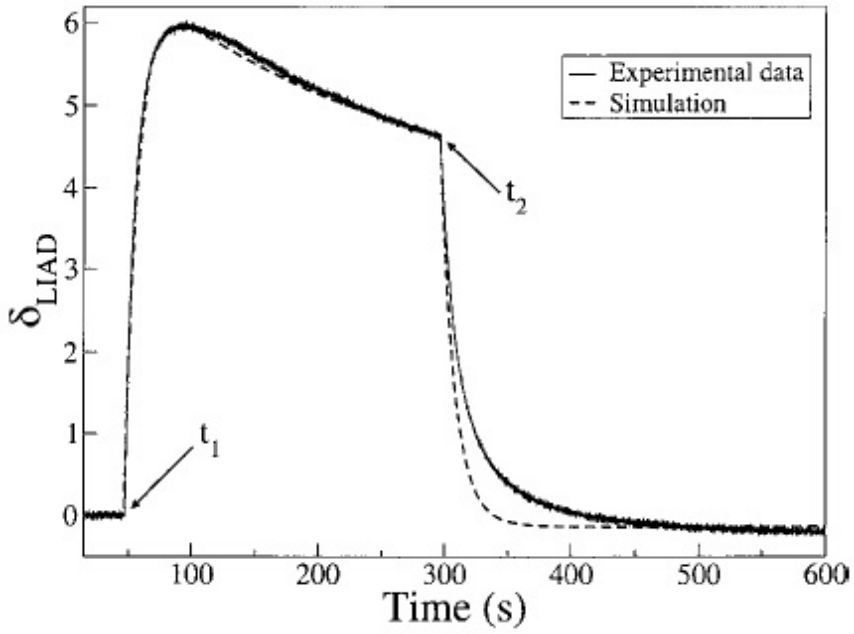

Figure 2.16: Measured δ_{LIAD} *(solid line)* and simulation *(dashed line)*, obtained with a desorbing light wavelength of 514 nm and an intensity of 6 mW/cm^2. The desorption light is switched on and off at t_1 and t_2 respectively [29].

In fig. 2.16 is reported the variation in the atomic vapor density, $\delta(t)_{LIAD}$, defined as:

$$\delta(t)_{LIAD} = \frac{n(t) - n_0}{n_0} \tag{2.19}$$

where $n(t)$ is the the atomic vapor density and n_0 is the value of density at thermal equilibrium. This measurement has been performed on a coated cell with a octadecyltrichlorosilane ($C_{18}H_{37}Cl_3Si$) dry-film and filled with Rb atoms. When the desorbing light is switched on the vapor density increase up to about six times the equilibrium vapor density, then starts decreasing. At t_2 the light is switche off and the vapor density drops to the thermal equilibrium value.

Beyond this, the main features of the LIAD effect are:

a) its non resonant nature,

b) the possibility of applying it on any element/molecule of interest interacting with any substrate,

c) the monotonic increasing efficiency with desorbing photon energy.

However, the details of this dependence can be significantly different as a function of the specific experimental conditions. For example,in the case of photodesorption from organic coatings, which generally have a low average adsorption energy ($E_a \sim 0.1\,eV$).

The desorbing yield increases with the square of the light frequency [31, 103, 109, 123] as can be seen in fig. 2.17, where the desorption efficiency, γ_{Rb} is plotted versus the desorbing photon energy [107]. The desorption efficiency is defined as the number of atoms desorbed per photon and it is of order of 10^{-8} atoms/ph. This measurement has been performed on a polydimethylsiloxane (PDMS) coated Pyrex cells filled with Rb atoms at room temperature and at low light intensity.

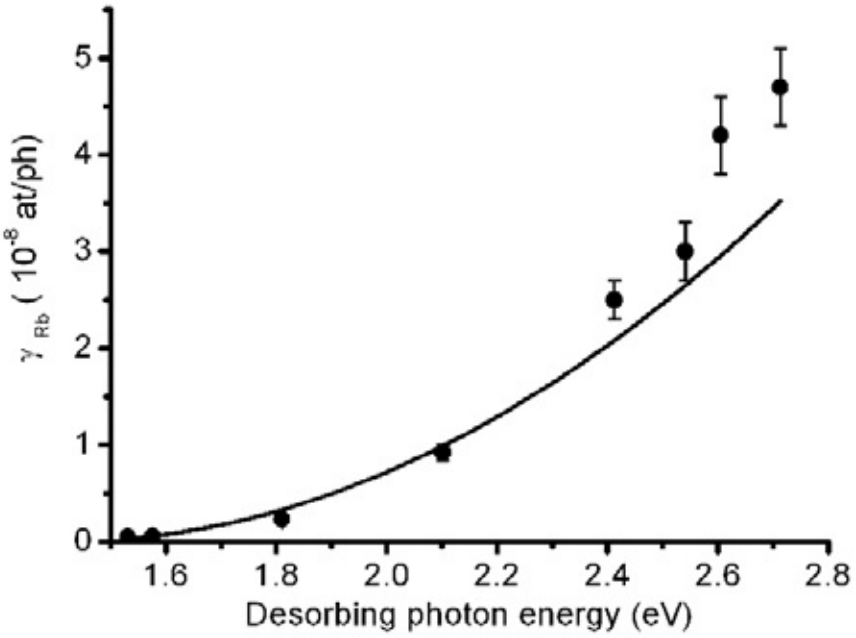

Figure 2.17: Experimental desorption efficiency γ_{Rb} as a function of the desorption photon energy. Continuous line is the fit with the function 2.20 [107].

In order to extrapolate the threshold frequency, the points have been fitted with the function:

$$\gamma = \alpha(h\nu - h\nu_{th})^2 \tag{2.20}$$

where $h\nu_{th}$ is the threshold frequency. The value obtained by the fitting is $h\nu_{th} = 1.4eV$.

A feature of the LIAD effect still under discussion is the eventual presence of a photon energy threshold. Apparently, it depends on the atom/surface pair.

For example, thresholds from PDMS coating seems to be at $1.40eV$ ($901nm$) for Rb [123] and at $1.18eV$ ($1053nm$) for Na [124]. For different substrates and atomic species involved, the threshold value drastically changes: for example, for K from fused silica, it results of about $3.04eV$ ($407nm$) [32].

2.4.2 Light-induced process in porous materials

The high surface/volume ratio makes the PG particularly suitable as host environment for photodesorption experiment. The first proof of the atomic desorption induced by the exposure to light from PG was found at the University of Siena in 2004 [112].

For what concerns PGs, the adsorption energy is relatively high, roughly of the order of $E_a \sim 1\,eV$ [125] (this part will be further explained in sec. 2.3). The drawback of the higher adsorption energy is compensated by the much larger available exposed surface provided by the internal structure of the PG. So the light yield is larger, even if the physical mechanism involved in the adsorption process is the same for both PGs and pure silica, where the effective surface is much smaller.

The exposition of a dielectric surface of SiO_2 to an atomic alkali vapor, and the adsorption of the latter on the surface, causes the growth of randomly distributed atomic layers [126].

The larger number of available sites of PGs, then, results in a larger number of adsorbed atoms which can be exposed to light. The yield of photodesorption in PGs has been proved to be higher even with respect on organic compound, such as polydimethylsiloxane (PDMS, $[-SiO(CH_3)_2-]_n$) [109], paraffin [122, 127] and octadecyltrichlorosilane (OTS, $CH_3(CH)_{17}Cl_3$) [29, 128] which have a lower adsorption energy ($E_a \sim 0.1\,eV$) and hence the desorption is favoured.

The presence of the pores, and hence the spatial confinement, gives rise to the spontaneous self-assembly of alkali aggregates, in other words, nanoparticles. This mechanism has been proved to occur more efficiently in presence of LIAD [26, 111]. This phenomenon, even if it is a peculiar characteristic of the PGs, take place also in other kinds of substrates, such as Vycor [129] and porous alumina [11]. The details of this process will be discussed in the following sections.

On the other side, there are no evidence of formation of such nanoparticles in substrate in which a strong confinement of the desorbed atoms is not guaranteed.

By illuminating the surface with near-infrared (near-IR) light, it is possible to make alkali atoms desorb from the nanoclusters. This is a consequence of the so-called Surface Plasmon Induced Desorption (SPID) [26]. Even if the results obtained by the illumination of the surface show similar features, as, for example, the increase of the atomic vapor density and the increase of atomic motion, the basic principles are completely different and different dynamics are observed. This topic will be treated more in detail in sec. 3.5.

In recent years, the interest in porous materials has increased in the branches of Atomic and Solid State physics. The first spectroscopic study of Rb atoms in a random porous material was performed by Villalba et al. in [130]. Porous materials strongly scatter the light, resulting in a randomization of the photon trajectories,

called "*integrating-sphere effect* ". The atoms confinement in the cavities influences the light emission and adsorption of the Rb atoms: an increase in the atomic vapor density corresponds to an increase in the probability of a non-radiative decay of the atoms due to collisions with the surface walls of the pores. Also the emitted photons have a significant probability of being re-absorbed by other atoms. Both these effects cause an increasing in the decay time of the fluorescence.

2.4.3 LIAD from porous silica

The LIAD effect has been observed in different porous material, such as Rb and Cs from porous glass [72, 112, 129], Vycor glass [131] and from porous alumina with Rb atoms [132]. In 2010 Villalba et al. [11] developed a 1-D model for the LIAD effect after experimental evidence of the light induced desorption of Rb atoms from nanoporous alumina; details of this models will be given in sec. 2.4.4.1.

The main difference between the LIAD from a smooth surface with respect to porous silica is the larger vapor density yield obtained in similar condition. As already said, the porous silica is characterized by a larger total surface and this allows for a much larger amount of adsorbed atoms per volume. So, even if the adsorbing energy is higher ($E_a \sim 1\,eV$, [125]), the greatly larger number of adsorbed atoms compensates the higher energy needed and the photoejection of a greater quantity of atoms is achieved.

Similarly to the case of an organic polymer, the relative increase of the alkali vapor density demonstrates a square root dependence on the desorbing light intensity [112], with a monotone increase of efficiency with the photon energy [26, 30]. On the contrary, the dependence on the frequency in PGs differs from the square relation observed in the organic coatings, as can be seen in fig. 2.18.

Another big difference with the LIAD in organic coatings is the structure of substrate itself: PGs are in fact characterized by a complex random oriented structure of pores and cavity. This implies that the desorbed atoms on a PG sample, are confined in nanometric volumes, helping the formation of metallic aggregates in presence of surface defects. A proof of such a behaviour is the appearance of a Gaussian-shaped band in the Near-IR region for Rb, where the density variation shows a resonant behaviour [26, 30]. In fig. 2.18 the plot of the relative density variation of Rb vapor versus desorbing photon energy is reported: a broad peak which overlaps the exponential background, is clearly visible between $1.3eV$ and $1.8eV$ [111]. This topic will be further discussed in Chap. 3.

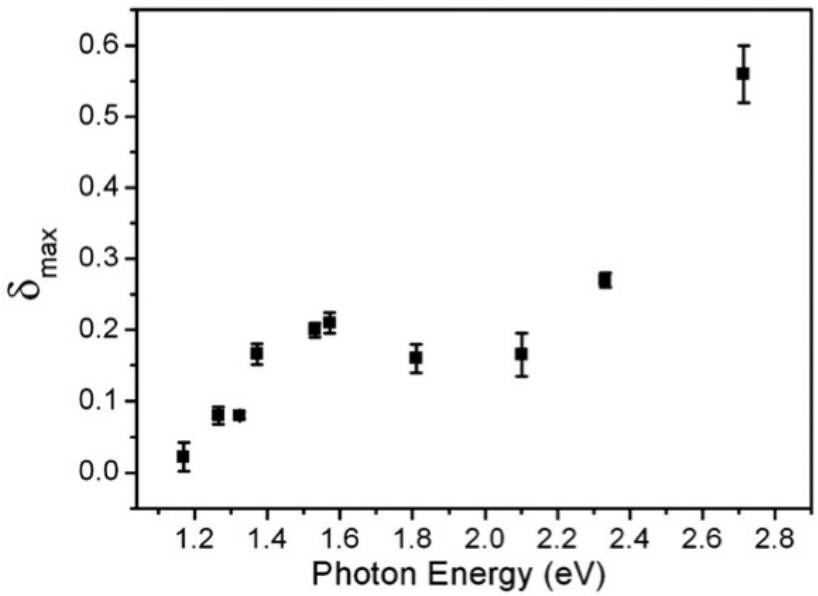

Figure 2.18: LIAD from PG: relative density variation of Rb vapor versus desorbing photon energy [111].

2.4.4 LIAD in vacuum

The study of the LIAD in a Ultra High Vacuum (UHV) condition is becoming more interesting because of the free environment condition present in such a context: better understanding and possibly better control of the growing process.

LIAD, as already stated, can be efficiently used as a tool to achieve an higher density of a certain atomic species, when needed. One limitation of LIAD is that the desorption is promoted for any species present in adsorbed state on the surface, without a real selection. If an experiment is performed in a chamber with Ultra High Vacuum (UHV) condition, the presence of unwanted species can be a severe limitation. However, the injection of a specific element in the chamber at a certain time often requires some heating procedure, high temperatures for low pressure vapors, i.e. contamination with high mean velocity atoms/molecules: the advantage of LIAD is to deliver in vapor phase species at room temperature, at high density, in very short time intervals. In fact, as discussed in par. 2.4, LIAD is widely used for the loading of Magneto-Optical Traps [105, 116] and to improve the loading efficiency for Bose-Einstein condensation [118, 119].

It is possible to use other method to load and modulate the partial pressure of the atomic gas for a MOT, such as pulsing alkali-metal dispenser [133, 134]. However, LIAD effect was proven very effective for ultra-cold atoms trapping [135]. In ref.[135], a simple LED light was used to activate LIAD and hence modulate the partial vapor pressure. A model based on rate equations can be applied to describe the

exchange of the population among surface and the volume. In the following, we will briefly report on this modeling.

In absence of LED light, the rate equation for the adsorbed atoms is:

$$\frac{dN_s}{dt} = -k_d N_s + k_a N_v \tag{2.21}$$

where N_s is the number stuck on the surface, N_v is the total number of atoms in the volume of the cell, k_d and k_s are, respectively, the desorption and adsorption rates; the latter is proportional to the surface cell area, while the former is inversely proportional to the sticking time τ_s (the average collision time of an atom taking into account the adsorption energy on the surface):

$$\tau_s = \frac{1}{k_d} = \tau_0 e^{E_a/k_b T} \tag{2.22}$$

where T is the surface temperature, E_a the adsorption energy and $\tau \simeq 10^{-12} s$ the oscillation time of the bond [136].

By switching on the desorption light, a new dynamical equilibrium is attained for N_v. It has been found that a steady state solution for the new equilibrium condition can be written in terms of the loading rate R (which, in turn, depends on N_v) as [135]:

$$R(I) \propto \frac{1 + \frac{k}{k_d} I}{1 + \frac{k}{k_d} I + \frac{k_a}{k_d}} \tag{2.23}$$

where I id the LED current and k is a constant proportional to LIAD cross-section.

Eq. 2.23 has been successfully used to fit the experimental curve in fig. 2.19 The

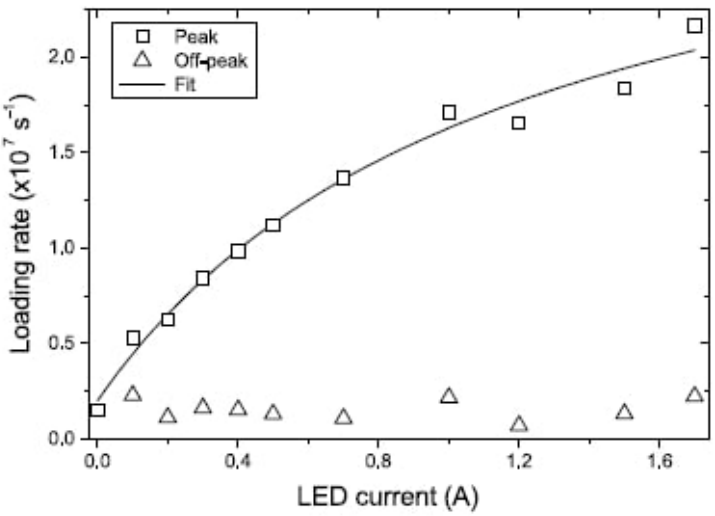

Figure 2.19: Loading rate measurements as a function of LED current during the LED pulse (peak) and before the pulse (off-peak). The solid line is the fit of eq. 2.23 to the experimental data [135].

off-peak constant value in fig. 2.19 confirms that the variation in the loading rate is due to the LIAD.

LIAD dynamics, with alkali atoms, has been investigated on nanoporous alumina samples in a vacuum chamber with a pressure of the order of $\sim 10^{-8} mbar$ [20]. Two different powerful light sources, the first in the violet (445 nm) and the second in the green (532 nm) range of the visible spectrum, were used to study the LIAD effect, over different thicknesses of porous alumina (100 nm and 300 nm). However, this argument will be further described in chap. 5, since it is part of this thesis work.

2.4.4.1 LIAD from porous alumina

In 2010 Villalba et al. [11] provided a 1-D model based on their study on atomic desorption of Rb atoms by nanoporous alumina. According to the hypotheses of this work, derived by other groups experimental evidences, the atoms are released from the internal pore surface with thermal velocities and are randomly emitted with a Lambertian probability distribution [137].

In fig. 2.20 the scheme of the one-dimensional model used in the following equation is shown. The pore is considered a cylindrical tunnel, closed on one side and with a total length L, which is much larger than its diameter. To the other side, the pore is connected, at a distance L_0, to a reservoir accounting both for the Rb stem and the vacuum pumping.

For pores with a diameters of hundreds of nanometers, the atom will be re-adsorbed by the surface after few nanoseconds of free flight. Since the diameter of pores is much smaller than the mean free path (MFP), $d \ll L$, it is possible to consider that the released atoms run a one-dimensional random walk along the pore axis, characterized by the diffusion constant D [11]:

$$D = \frac{\langle l^2 \rangle}{2\tau} = \frac{d^2}{3\tau} \tag{2.24}$$

where $\langle l^2 \rangle$ is the mean square displacement per step in the random walk and τ is the mean time interval between two steps: it is essentially determined by the sticking time, $\tau \simeq \tau_s$.

Light induces a reduction of the sticking time τ_s, which in turn causes the atomic desorption. Taking, for simplicity, a linear dependence of τ_s:

$$\tau_s = \tau_{s0}(1 - \kappa(\lambda)I) \tag{2.25}$$

where τ_{s0} is the sticking time in the dark, I is the light intensity and κ is a coefficient that depends on the wavelength.

Different values of κ have been obtained experimentally for different wavelength of the illumination light: for example, the maximum value of the coefficient

has been obtained with wavelength in the red part of the light spectrum and it has a value of $\kappa_{red} = 7.8 \pm 0.7 \times 10^{-3} (mW/cm^2)^{-1}$. The value of coefficient, however, does not vary monotonically with the wavelength of the desorbing light [11].

Then substituting 2.25 in 2.24:

$$D = \frac{D_0}{(1 - \kappa(\lambda) I)} \tag{2.26}$$

with $D_0 = d^2/3\tau_{s0}$ tha atomic diffusion constant in the dark.

The linear density of atoms $\mu(y,t)$, at room temperature, inside the pore can be described by the diffusion equation:

$$\frac{\partial \mu}{\partial t} = D \frac{\partial^2 \mu}{\partial y^2} \tag{2.27}$$

where y is the position along the pore length. Note however, that the linear density $\mu(y,t)$, depends also on the intensity of the light, since the diffusion constant D depends on τ_s and hence on I.

It is worth noting the variation due to the LIAD effect on atomic density inside the cell. The total number of atoms is $N = N_g + N_w$, where N_g are the atoms in gas phase and N_w are the atoms stuck to the cell walls.

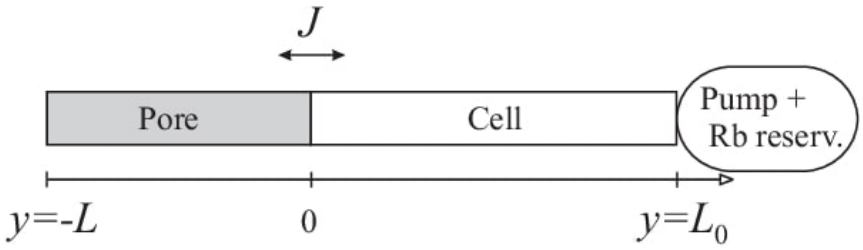

Figure 2.20: Scheme of the 1-D model used for the system. $y = 0$ is placed at the pore-vapor interface[11].

For a given temperature and illumination condition, the fraction of atoms in the gas phase with respect to the total number of atoms is taken to be a constant [136]:

$$\frac{N_g}{N} = \frac{L_0}{L_0 + \Delta} \tag{2.28}$$

where Δ is an effective cell length corresponding to the adsorbed atoms. Since the sticking time τ_s depends, in principle, linearly by the intensity of light, it is possible to define in a similar way Δ as $\Delta = \Delta_0(1 - \zeta I)$, where ζ is a coefficient that depends on wavelength.

The following equation describes the the evolution of the atom number N in the cell:

$$\frac{dN}{dt} = \frac{dN_g}{dt} \left\{ 1 + \frac{\Delta}{L_0} \right\} = J - \gamma(N_g - N_{g0}) \tag{2.29}$$

the rate γ is a coefficient describing the return to the equilibrium state N_{g0}, which is determined by the Rb reserve. If the Rb dispenser is switched off, the vacuum pump provides to bring the pressure, and hence the atomic density in the chamber, in a few seconds.

J is the net atomic flux at the pore-vapor interface and it can be separated into two contributions, $J = J^+ + J^-$, describing respectively the incoming and outgoing flux of atoms in the pores. J^- can be defined as:

$$J^- = -\left(\frac{\bar{v}}{2L_0}\right) N_g \tag{2.30}$$

where $\bar{v} \equiv \langle |v_y| \rangle$ is the mean velocity of the atoms along the pore direction y.

Given the simple geometry of the system, J^+ can be evaluated by considering that an atoms, starting from the pore end, and with a mean step length l, have a probability of 0.5 to leave the pore in a time interval τ, and so:

$$J^+ = [\mu(0)l]\frac{1}{2\tau} \simeq \mu(0)\frac{D}{l} \tag{2.31}$$

with the approximation of $l \simeq \langle l^2 \rangle^{\frac{1}{2}}$.

Now it is possible to write down the equations describing the time evolution of the atomic densities μ and $n \equiv N_g/L_0$ inside the pore and in gas phase, which are respectively:

$$\frac{\partial \mu}{\partial t} = D\frac{\partial^2 \mu}{\partial y^2} \tag{2.32}$$

$$\frac{\mathrm{d}n}{\mathrm{d}t} = \frac{D}{lL_c(1-\sigma I)}\mu(0) - \frac{\left(\tilde{\gamma} - \frac{\bar{v}}{2L_c}\right)}{(1-\sigma I)}n + \frac{\tilde{\gamma}}{(1-\sigma I)}n_0 \tag{2.33}$$

where n_0 represents the equilibrium value of the atomic density in the vapor cell and the parameters $\sigma \equiv \frac{\zeta}{\left(1+\frac{L_0}{\Delta_0}\right)}$, $L_c \equiv (L_0 + \Delta_0)$ and $\tilde{\gamma} \equiv \frac{\gamma L_0}{L_c}$ have been introduced.

The steady-states densities without illumination inside the pores μ_0 and in the vapor cells n_0 are related by the relation:

$$J = \frac{D_0}{l}\mu_0 - \frac{\bar{v}}{2}n_0 = 0 \tag{2.34}$$

and the boundary condition at $y = 0$ and $y = -L$ are respectively:

$$-D\frac{\partial \mu}{\partial y}\bigg|_{y=0} = \frac{D}{l}\mu(0) - \frac{\bar{v}}{2}n, \tag{2.35}$$

$$-D\frac{\partial \mu}{\partial y}\bigg|_{y=-L} = 0. \tag{2.36}$$

When the Rb dispenser is switched off, eq. 2.33 can be written as:

$$\frac{\mathrm{d}n}{\mathrm{d}t} = \frac{D}{lL_c(1-\sigma I)}\mu(0) - \gamma_1 n - \gamma_2 n, \tag{2.37}$$

where γ_1 and γ_2 represent respectively the loss of the atomic density due the atoms adsorbed on the wall of the chamber and the atoms removed by the pumping system.

As said earlier, the coefficient κ and then the variation of the atomic densities inside the pores, presents a nonmonotonic dependance with the desorbing light wavelength. This suggests that the atomic desorption depends, in part, by the atoms released from the rubidium clusters, hence, the surface plasmonic resonances may play a key role to the light absorption spectrum [11].

It must be noted that this model is not complete. The main problem is probably the simple geometrical modeling of the pores using a cylindrical shape, furthermore with the approximation $l \gg d$. In this way it is not taken into account the random orientation of the porous structure, assuming instead a regularity that does not belong to such structures.

For what concerns the theoretical part, eq. 2.25 and 2.26 can be negative for value sufficient large of the light intensity [138]. However this model has been proven in agreement with the experimental results [11].

2.5 Microscopic interpretation of LIAD

It is difficult to have a general and satisfactory theory of the LIAD effect, mainly for two reasons. The first is the high number of parameters involved in LIAD process, such as the substrate, the involved atomic species and their interactions, causing apparently inconsistent phenomenology and dynamics. The other is the technical difficulties in obtaining direct, and at the same time, non-destructive imaging and information of the system as well as to separate the bulk effects by the surface ones.

There are, however, some theories able to replicate groups of experimental results, that will be briefly summarized in the following sections.

2.5.1 Light-induced charge transfer

Some LIAD models of the photoejection effect are based on the charge transfer induced by the desorbing light. The first explanation of this model was provided in [31, 139], together with the first experimental data. The authors have introduced the concept of "photoatomic effect" because of the similarities with the photoelectric effect.

In the paper, the adsorption of Na atoms into the PDMS coating is explained in terms of Van der Waals interactions: the alkali atoms interact with the H atoms of the coating, which in turn interact with the wall glass through the Si and O atoms, leaving the methyl group CH_3 acting as interface for the vapor phase. This consideration leads to the fact the adsorption and desorption processes are indeed surface effects, while the bulk does not contribute to the relevant processes.

Specifically, the idea is that the alkali atoms, similarly to the alkali metal solvation reaction [31], either exchange an electron with the coating

$$Na \rightarrow Na^+ + e^- \tag{2.38}$$

or are able to form a cation/anion couple

$$2Na \rightarrow Na^+ + Na^-. \tag{2.39}$$

The Na^+ ion is complexed by the coating which behaves as a solvent. The result is indeed a chemisorption:

$$2Na^+ + PDMS \rightarrow Na^+(PDMS). \tag{2.40}$$

The hypothesis is that while the cations are stuck at sites of the long organic chains, the anions can diffuse freely onto the surface to neutralize the complexed cations. As a consequence of this, macromolecules with the structure Na^+(PDMS)Na^- are formed.

At this point, the light-induced ejection is explained by the neutralization of Na^- ions by the interaction with photons:

$$Na^+(PDMS)Na^- + h\nu \rightarrow Na^+(PDMS) + Na + e^-. \tag{2.41}$$

This model successfully explains the observed frequency threshold as well the desorption result in pulsed regime, where green (532nm) and infrared (1064) light allow the excitation of different energy levels of alkali/PDMS complex [108]. However the

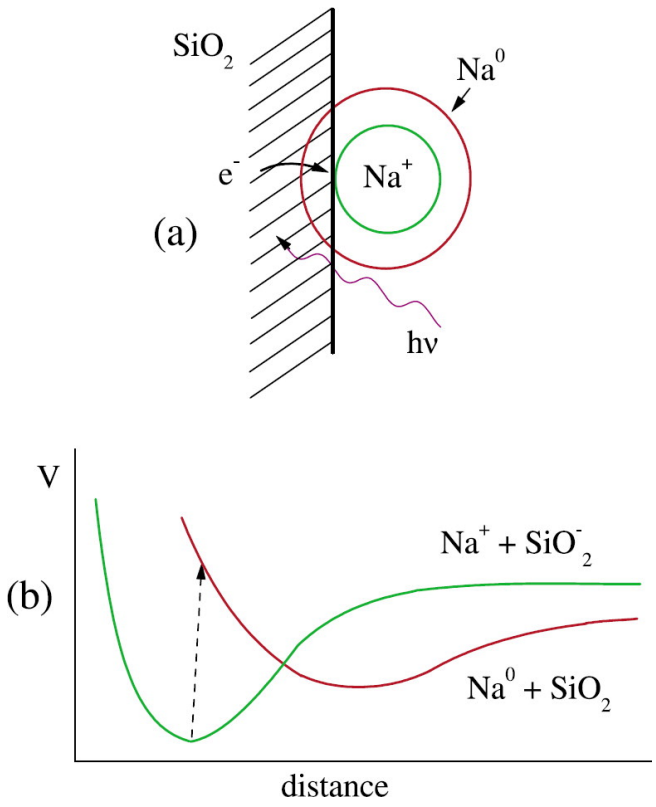

Figure 2.21: Scheme for the photon stimulated desorption of Na from porous SiO_2 at moon surface: **(a)** a solar UV photon excites an electron from the substrates, which is captured by the Na^+ and hence converted to neutral Na. Because of the larger atomic radius the atom can desorb. **(b)** The interaction potential V as a function of distance from the surface [140].

models presents some drawbacks, it is strictly dependent on the atomic species involved and on the particular energy level structure of the same.

The charge-transfer approach was also used to explain the presence of alkali atoms in the moon atmosphere [140]: Na atoms are adsorbed at the interface between porous SiO_2 in the form of Na^+ ions (see fig.2.21).

2.5.2 Light-induced local oscillations

The idea behind this second model is based on the vibrational relaxations induced by a photon which may cause the desorption of an atom from the substrate. In this framework, LIAD can be seen as local oscillations excited by the absorption of a photon by an alkali atom or a coating electron that may cause the release of the adsorbed atom. The authors in [103] presented a first proper theory about LIAD

in which they proposed a link between LIAD and physisorption due to a discrepancy between the adsorption energy of Rb onto the PDMS, considering only surface effect, and the expected value. The physisorption leaves enough mobility also perpendicularly to the surface, so also the bulk is involved. LIAD was explained as a local oscillations induced by the absorption of a photon by a Rb atom or by a coating molecule. It must said that this model successfully explains the non-resonant behaviour, excluding as well a direct heating of the interface.

The local mechanism for excitation was further extended in the context of non-resonant inelastic scattering. This idea comes from the observation of an equal dynamics and dependencies for the desorption of Rb and Cs atoms from PDMS, thus excluding a relation with the energy level structure of the atoms [107]. In terms of local excitations, the adsorbed atoms can be thought as confined in potential wells exhibiting just a few bound vibrational states because of the low adsorption energy. These bound states lose their stationary character if a polymer chain vibration is excited by a photon and therefore the adsorbed atoms can diffuse freely to nearest-neighbor sites by phonons. In other words, atoms can freely diffuse on the coating, provided the presence of coating phonons.

If an external illumination is introduced, the inelastic scattering between the incident photons and the chain of the coating brings to the formation of phonons. This may increase the local atomic kinetic energy up to overcome the adsorption energy, thus causing the desorption of the atoms into the vapor phase.

Chapter 3

Optics of Nanoparticles

This chapter is dedicated to the description of atomic aggregates, commonly known as nanoparticles, and their optical properties. A general introduction of nanoscale optics is given in sec. 3.1. Sec. 3.2 describe more in detail the the Localized Surface Plasmon resonances happening in metal nanoparticles. The Mie-Gans theory for light scattering on nanoparticles is given in sec. 3.4. Finally in sec. 3.5 a description of the Surface Plasmon-Induced Desorption (SPID) from nanoparticles is provided.

3.1 Optics at nanoscale

Usually, nanoparticles (NP) are defined as an aggregates of single atoms or molecules, with dimension between 1 and 100 nm. Their importance crosses through many fields, such as fundemental physics [141–143], nanotechnology [144–147], energy, environmental [148–150] and health science [151–153].

For what concerns transport and interaction properties with the external environment, NPs behave as a single object with different features with respect to a bulk sample of the same material. The different behaviour between the NP and the bulk object and single atoms is due to the nanometric confinement, the geometry and the interaction between the atomic electrons composing the cluster. In this picture, NPs can be seen as an intermediate state between the single element, like an atom or a molecule, where the system behaviour is described by the law of the quantum mechanics, and the bulk material, having macroscopical dimension and hence can be

studied with a semiclassical approach.

More specifically, at nanometric length scales, the electrons interactions are ruled by spatial confinement and cooperative effect. In this sensee it is possible to divide the size effects of nanoparticles into two main classes [154]:

- **intrinsic size effects:** the dimension and the shape of the cluster affect its energetic, electronic and structural properties;
- **extrinsic size effects:** the dimension and the shape of the cluster affect the response to external perturbation.

The first class of effects are directly linked to the spatial confinement of the electrons motions and are relevant in systems such as nanowires or nanodots, where the shape factor dominates. However, since the optical response of a metal nanoparticle embedded in a dielectric substrate can be considered as an extrinsic effect, the intrinsic properties will not be treated in this section. On the other side, in metallic NPs, the electronic interactions with the external environment are governed by cooperative phenomena. Considering the high number of electrons involved in the system response, it is possible to study the latter case with a semiclassical approach [155].

Taking into account another property of NPs, i.e. the large number of surface atoms in the NPs with respect to the number of internal atoms, the surface processes are enhanced as well the interaction with the surrounding medium. This characteristic is one of the reasons of the growing of nano-optics research. It is possible, for example, to design and build up practical systems with an interaction between photons and matter localized below 10^2 nm.

From our point of view, the optical response of a NP is mainly due by extrinsic factors such as its geometry and the interactions with environment and with neighbor nanostructures [156]. However, it is difficult to develop a general theory if one takes into account all the possible configuration, like shape, size, surrounding medium [154]. In the case of large (more than tens of atoms) clusters, it is usually possible to introduce an electrodynamical approach.

In general, when a photon hits a metal nanoparticle, it induces electronic and vibrational excitation which can lead to the breaking or the evaporation of the same[154]. These effects will be studied more deeply in the following section.

3.2 Localized Surface Plasmon

A metal nanoparticle can be viewed as an aggregate of atoms kept together by the balance of Van der Waals force and surface tension. The NPs are surrounded

by a cloud of delocalized electrons, namely the conduction electrons of the metal structure that form a free electron gas at the surface [157]. This means that NPs can be approximated by a Drude metal.

In general, in presence of an external electromagnetic perturbation, the electrons at the surface react as a collective object. Light absorption by a metal nanoparticle is well explained by considering coherent oscillation of the interface electron gas induced by an electromagnetic field. The coupling of a E.M. wave with a charge oscillation, called Plasmon waves, generates the quasi-particle *Plasmon Polariton*, whose properties strongly depend on the geometry of the metal/dielectric interface. For example, in the case of a planar interface, the excitation can move parallel to the interface and it is called **Surface Plasmon Polariton** (SPP), while in metal NPs, because of the space confinment of the electron gas, the plasmon polariton cannot propagate. On the contrary, the conduction electrons oscillate coherently: this latter case is defined as **Localized Surface Plasmon** (LSP).

As a consequence of the localized nature of the LSP, this quasi particle has a zero wavevector ($\mathbf{K_{LSP}} \equiv 0$) and therefore there is no phase shifting with respect to the incoming photon [158].

More in detail, let's consider the interaction between a photon with wavelength λ and a the metal NP that can be approximate as a sphere of diameter $2a$. If the relation

$$2a \ll \lambda \tag{3.1}$$

is verified, it is possible to neglect the spatial dispersion of the photon over the volume of the sphere and the so-called quasi-static approximation is valid. For visible light, the quasi-static approximation holds for $2a \lesssim 20nm$ [154]. In the context of the

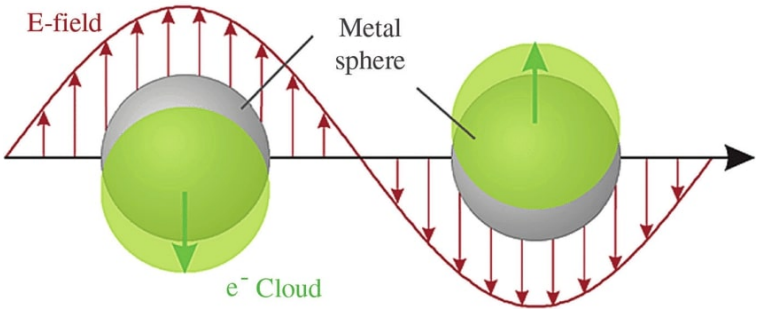

Figure 3.1: Schematic of plasmon oscillation for a sphere, showing thedisplacement of the conduction electron charge cloud relative to the nuclei. [155].

Drude model, which is at the basis of this analysis, the mean free path (MFP) of the electrons is a key parameter to take into account. In the case of small nanoparticles, MFP is smaller than both the particle size and the skin depth of the E.M. field; therefore, the field can be considered uniform inside the volume and the NP electrons can react coherently to the external field.

The external electric field causes a collective displacement of the electron over the NP surface, producing then a net polarization. The Coulomb interaction between the displaced electron cloud and the fixed positive charge of the nuclei produces a restoring force able to force coherent oscillations of the conduction electrons. These oscillations produce the LSP in the reference frame of the nuclei, as shown in 3.1.

3.2.1 Electrostatic approximation

Let's take into account the following assumptions:

1. the NP is a homogeneous, isotropic conductive sphere, with radius a and relative dielectric function $\varepsilon(\omega)$.

2. the dielectric environment completely surrounds the NP and it is homogeneous, isotropic and non-absorbing, with a constant relative dielectric function ε_m.

3. the incoming electric field can be considered spatially uniform over the NP volume and constant in time:

$$\mathbf{E}(\mathbf{r},t) = \mathbf{E_0}. \tag{3.2}$$

With these approximations the problem can be solved by using the Laplace equation formalism [155], for example, as presented in [159, Chapter 5]. The geometry of the problem is described in fig. 3.2. Considering the incoming electric field parallel to the $\hat{z}$ axis ($\mathbf{E} = E_0\hat{z}$) and indicating the electric potential with ϕ, the electric field in the surroundings of the metal NP, $\mathbf{E}_{loc}$ is [160]:

$$\mathbf{E}_{loc} = -\nabla\phi \tag{3.3}$$

and the electrostatic Laplace equation is:

$$\nabla^2\phi = 0 \tag{3.4}$$

with the following boundary conditions:

- continuity of the tangential component of the electric field (E_θ) at the sphere/dielectric interface:

$$-\frac{1}{a}\frac{\partial\phi}{\partial\theta}\bigg|_{r=a^-} = -\frac{1}{a}\frac{\partial\phi}{\partial\theta}\bigg|_{r=a^+} \tag{3.5}$$

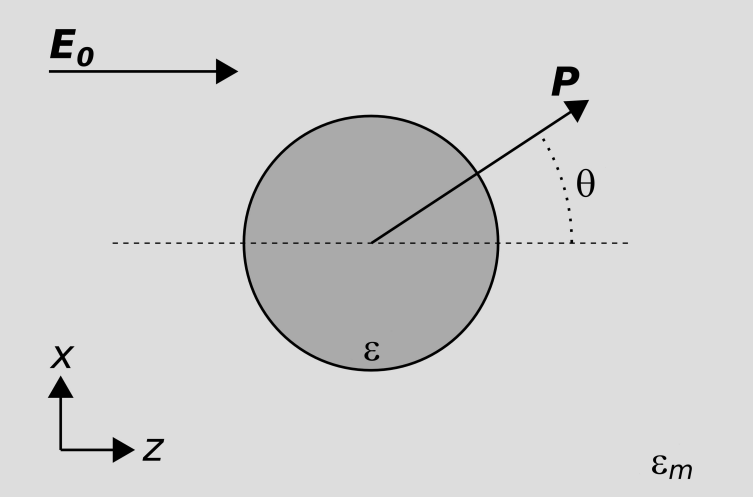

Figure 3.2: Scheme of the interaction on an external static electric field $\mathbf{E}_0$ with a metal sphere.

- continuity of the radial component of the electric displacement vector $\mathbf{D} = \varepsilon\mathbf{E}$ (D_r):

$$-\varepsilon(\omega)\frac{\partial\phi}{\partial\theta}\bigg|_{r=a^-} = -\varepsilon_m\frac{\partial\phi}{\partial\theta}\bigg|_{r=a^+} \tag{3.6}$$

- the potential ϕ has a far-field behavior related to the E.M. field only:

$$\phi(r\to\infty) = -E_0 z = -E_0 r\cos\theta \tag{3.7}$$

With these boundary conditions, the general solutions for the angular and the radial coordinates 3.4 are respectively the spherical harmonics ($P_l(\cos\theta)$) and functions of the form r^l and r^{l+1}, where l is the azimuthal quantum number determining the atomic angular momentum. Hence:

$$\phi(r,\theta) = \begin{cases} \sum_{l=0}^{\infty} A_l r^l P_l(\cos\theta) & \text{for } r \le a \\ \sum_{l=0}^{\infty} [B_l r^l + C_l r^{-(l+1)}] P_l(\cos\theta) & \text{for } r > a \end{cases} \tag{3.8}$$

From the conditions 3.5 and 3.6, we get:

$$A_l = C_l = 0 \quad \text{for} \quad l \neq 1 \tag{3.9}$$

and from 3.7

$$B_l = \begin{cases} -E_0 & \text{for } l = 1 \\ 0 & \text{for } l \neq 1 \end{cases} \tag{3.10}$$

Hence the solutions of the Laplace equation 3.4 are:

$$\phi(r,\theta) = \begin{cases} -\frac{3\varepsilon_m}{\varepsilon+2\varepsilon_m} E_0 r\cos(\theta) & \text{for } r \le a \\ E_0 r\cos(\theta)(\frac{\varepsilon-\varepsilon_m}{\varepsilon+2\varepsilon_m} - 1) & \text{for } r > a \end{cases} \tag{3.11}$$

In terms of the dipole moment $\mathbf{p}$:

$$\mathbf{p} = 4\pi\varepsilon_0\varepsilon_m a^3 \frac{\varepsilon-\varepsilon_m}{\varepsilon+2\varepsilon_m}\mathbf{E}_0 \tag{3.12}$$

so the potential ϕ in the external region becomes:

$$\phi(r,\theta) = -E_0 r\cos(\theta) + \frac{\mathbf{p}\cdot\mathbf{r}}{4\pi\varepsilon_0\varepsilon_m r^3} \quad \text{for} \quad r > a \tag{3.13}$$

As a consequence, the electric field outside the sphere results enhanced: it is given, indeed, by the superposition of the external field $\mathbf{E}_0$ and the local dipole field proportional to E_0 and centered in the NP:

$$\mathbf{E}(r>a) = \mathbf{E}_0 + \frac{3\hat{n}(\hat{n}\cdot\mathbf{p}) - \mathbf{p}}{4\pi\varepsilon_0\varepsilon_m r^3} \tag{3.14}$$

Introducing the polarizability α as $\mathbf{p} = \varepsilon_0\varepsilon_m\alpha\mathbf{E}_0$, from eq. 3.12 it is possible to write:

$$\alpha = 4\pi a^3 \frac{\varepsilon-\varepsilon_m}{\varepsilon+2\varepsilon_m} \tag{3.15}$$

which descibes the polarizability of a sphere with diameter $a < \lambda$. According to eq. 3.15, α has a maximum for $|\varepsilon + 2\varepsilon_m| \to 0$. As shown in fig. 3.3, polarizability has a resonant behaviour when the following identity, named the Frölich condition, is verified [159, Chapter 5]:

$$\mathrm{Re}(\varepsilon) = -2\varepsilon_m \tag{3.16}$$

Relation 3.16 explains the resonant onset of the LSP at the metal nanoparticle interface after the interaction with an external electromagnetic field, in the quasi-static approximation. In fact, considering a sphere in the Drude model [159, Chapter 5], the complex dielectric function is:

$$\varepsilon(\omega) = 1 - \frac{\omega_p^2}{\omega^2 + i\gamma\omega} \tag{3.17}$$

where $\gamma = 1/\tau$ is the damping constant and ω_p^2 the bulk plasma frequency:

$$\omega_p^2 = \frac{n_e e^2}{m^*\varepsilon_0} \tag{3.18}$$

Here, n_e is the average electron density and m^* the effective mass of the conduction electrons.

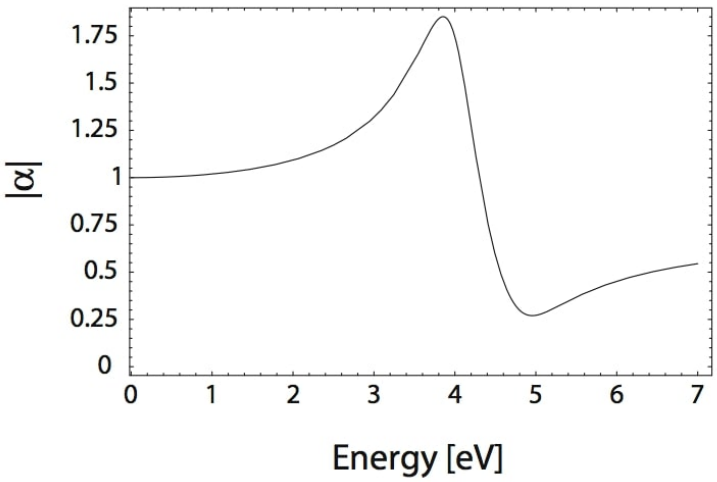

Figure 3.3: Absolute value of the polarizability α of a metal nanoparticle with respect to the energy of the driving electric field [159, Chapter 5].

One point to highlight in the resonance condition 3.16 is the explicit dependence on the dielectric constant ε_m of the surrounding medium, in such a way that the frequency position of the LSP is directly related to the embedding medium.

Another important aspect is the strong dependence of the LSP on the size a and on the shape of the nanoparticle.

3.2.2 Quasi-static approximation

In order to properly describe the process of light absorption of a metal NP, an oscillating external electric field must be taken into account. Then, replacing the constant field in eq. 3.2, we get:

$$\mathbf{E}(\mathbf{r},t) = \mathbf{E_0} e^{-i\omega t} \quad \text{for} \quad 2a \ll \lambda \tag{3.19}$$

where $\omega = 2\pi\nu = 2\pi c/\lambda$. The metal sphere can be seen as an oscillating dipole in phase with an external electric field [159, Chapter 5]:

$$\mathbf{p}(t) = \varepsilon_0 \varepsilon_m \alpha \mathbf{E_0} e^{-i\omega t} \tag{3.20}$$

The absorption of a resonant photon brings to the emission of radiation of an induced dipole moment centered into the metal NP, that can be seen as a scattering process of the incoming wave by the NP.

By taking into account the expression of the Poynting vector, the scattering cross section, σ_{sca}, and the absorption cross section, σ_{abs}, can be computed [159, Chapter 5]:

$$\sigma_{sca} = \frac{k^4}{6\pi}|\alpha|^2 = \frac{8\pi}{3}k^4a^6\left|\frac{\varepsilon-\varepsilon_m}{\varepsilon+2\varepsilon_m}\right|^2 \tag{3.21}$$

$$\sigma_{abs} = k\,\mathrm{Im}(\alpha) = 4\pi ka^3\,\mathrm{Im}\left[\frac{\varepsilon-\varepsilon_m}{\varepsilon+2\varepsilon_m}\right] \tag{3.22}$$

where k is the wave vector modulus.

It is also possible to compute the total extinction cross section of the NP, which is directly related to the absorbance spectra of the cluster:

$$\sigma_{ext} = \sigma_{sca} + \sigma_{abs} = 9\frac{\omega}{c}\varepsilon_m^{3/2}V\frac{\varepsilon_2(\omega)}{[\varepsilon_1(\omega)+2\varepsilon_m]^2+\varepsilon_2^2(\omega)} \tag{3.23}$$

where V is the volume of the particle and $\varepsilon(\omega) = \varepsilon_1(\omega) + i\varepsilon_2(\omega)$.

This model, even if obtained with several limiting approximations, correctly predicts the resonant local field enhancement whenever the condition 3.16 is verified and is usually effective in the description of the LSP physics for NP with $a \ll \lambda$ [159, Chapter 5]. The theory takes into account the embedding medium properties as well as the dipole-like behaviour of the NP. However, this model fails in predicting the response of non-spherical NPs with a non-uniform distribution.

3.3 Mie theory

An exact electrodynamical theory of optical scattering and absorption by a metal sphere was developed by G. Mie in 1908 [161], implementing multipolar contributions and sum rules over size and geometry distributions. The following treatment will follow the approach presented in [154, Chapter 2].

The issue of light scattering by a metal sphere can be divided into two parts:

- electromagnetic field problem, solved exactly from first principles
- matter description, that can be given by introducing a phenomenological dielectric function $\varepsilon(\omega, \alpha)$

For what concerns the electromagnetic problem, Mie introduced sets of electric and magnetic scalar potentials, $\Pi_{e,m}$, for the incident plane wave, that in spherical coordinates take the form:

$$\Pi = R(r)\Theta(\theta)\Phi(\phi) \tag{3.24}$$

representing the wave propagating inside the sphere as well as the scattered wave outside its volume. Using eq. 3.24 to solve the wave equation in the limit $ka \ll 1$ (small particles), it leads to the extinction cross-section by making use of a series of partial wave expansion of the fields:

$$\sigma_{ext} = \frac{2\pi}{k^2} \sum_{L=1}^{\infty} (2L+1)\,\mathrm{Re}(a_L + b_L) \tag{3.25}$$

$$\sigma_{sca} = \frac{2\pi}{k^2} \sum_{L=1}^{\infty} (2L+1)(|a_L|^2 + |b_L|^2) \tag{3.26}$$

$$\sigma_{abs} = \sigma_{ext} - \sigma_{sca} \tag{3.27}$$

where

$$a_L = \frac{m\psi_L(mx)\psi_L'(x) - \psi_L'(mx)\psi_L(x)}{m\psi_L(mx)\eta_L'(x) - \psi_L'(mx)\eta_L(x)} \tag{3.28}$$

$$b_L = \frac{\psi_L(mx)\psi_L'(x) - m\psi_L'(mx)\psi_L(x)}{\psi_L(mx)\eta_L'(x) - m\psi_L'(mx)\eta_L(x)} \tag{3.29}$$

with $m = \tilde{n}/n_m$ ratio between the complex refractive index of the particle and the real refractive index of the surrounding medium; $x = |\mathbf{k}|a$ the size parameter; ψ_L and η_L the Riccati-Bessel cylindrical functions and L the partial wave order, labelling the multipole order.

For a given L, the electric contributions are related to the SPP modes, the magnetic contributions to the eddy currents formed at the surface. In order to obtain the dipole order which correctly approximates the results described in the previous section, the sum must be truncated to $L = 1$ and the magnetic contribution must be neglected [162]. For example, the field lines of force for different electric multipole orders in the far field, are shown in fig. 3.4. As a general rule, for spectra calculations,

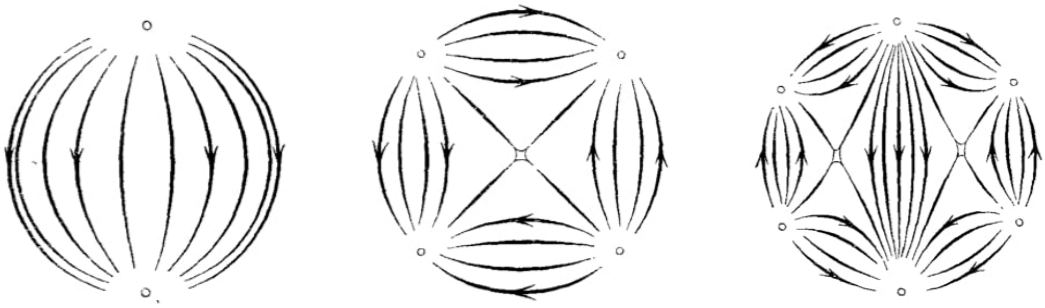

Figure 3.4: Electric field lines in the far field associated to the partial waves in the case, from left to right, of $L = 1$ (dipole), $L = 2$ (quadrupole), $L = 3$ (octupole) modes, for Mie theory [161].

the cross-sections in eq. 3.25, 3.26 and 3.27, must be weighted with the total oscillator strength of all the electrons involved in the localized plasmon resonance. This can be

obtained by integrating the spectrum of the Mie extinction constant $\gamma_{ext} = \sigma_{ext} n_{cluster}$, with $n_{cluster}$ the cluster density [163]:

$$Q_{eff} = 2c \frac{(1+2\varepsilon_m)^2}{9\pi^2 \varepsilon_m^{3/2} \omega_p^2} \int_0^\infty \gamma_{ext}(\omega) d\omega. \tag{3.30}$$

For Drude metals, like alkali atoms, it results $Q_{eff} = 1$ around the plasma resonance, that means that all the available conduction electrons participates in the formation of the LSP resonance. This entails a remarkable difference between the case of a bulk structured metal and a nanoparticle: in the first case, the oscillator strength is spread continuously in the region $\omega < \omega_p$, while for NP this region is confined in a relatively narrow band of frequencies around the surface plasmon resonance; that is why metal nanoparticles are transparent outside the resonance band [154, Chapter 2].

In general, because of the complexity of the problem, the solution of the Mie problem is computed numerically [154, Chapter 2]. However, in the limit $a \ll \lambda$, the terms a_L and b_L in eq. 3.28 and 3.29, are proportional to $(ka)^{2L+1}$, then, the summation can be stopped to the lowest term and the Mie formula for the extinction corss-section 3.25 reduces to the extinction cross-section computed in the quasi-static approximation in eq. 3.23.

For a Drude metal nanoparticle, if the electron damping constant $\gamma = 1/\tau$ is negligible with respect to the electromagnetic wave frequency ω, the real and imaginary parts of the metal dielectric function can be approximated as:

$$\varepsilon_1(\omega) \approx 1 - \frac{\omega_p^2}{\omega^2} \tag{3.31}$$

$$\varepsilon_2(\omega) \approx \frac{\omega_p^2}{\omega^3} \frac{1}{\tau} \tag{3.32}$$

which can be used in eq. 3.23 to obtain a Lorentzian-shape resonance for wavelengths in the near infrared and visible region:

$$\sigma_{ext} = \sigma_0 \frac{1}{(\omega - \omega_{LSP})^2 + (\gamma/2)^2} \tag{3.33}$$

where the resonance frequency for the LSP ω_{LSP} can be expressed in terms of the plasma frequency ω_P as:

$$\omega_{LSP} = \left. \frac{\omega_P}{\sqrt{1 + (L+1)\varepsilon_m / L}} \right|_{L=1} = \frac{\omega_P}{\sqrt{1+2\varepsilon_m}} \tag{3.34}$$

It must be noted the dependency of eq. 3.34 on the surrounding medium via the dielectric constant ε_m: by increasing the dielectric constant ε_m, the LSP resonance will be progressively red-shifted. For what concerns, for example, the influence of

a substrate, it is possible to use an effective dielectric constant, which is an average of the dielectric constants of all the component of the surrounding medium [154, Chapter 2]. This is the case of porous glasses, in which the dielectric function is taken as an average over the vacuum in the pores and the bulk material.

3.4 Gans theory

If a non-spherical NP is taken into account, the solution of the exact electrodynamical problem becomes more challenging from a mathematical point of view. The cross-section in closed-form expression is available only for special cases, like in the quasi-static approximation. A theory that treats nanoparticles as randomly oriented spheroids was originally presented by R. Gans for Au and Ag [164, 165] as an extension of the Mie theory.

Geometrically, a spheroid is a rotational ellipsoid, i.e. it is obtained by rotating an ellipse about one of the principal axes. Indicating with a, b and c the three orthogonal main axes lengths and taking a as the axis of revolution, it is possible to separate the following cases:

- **Prolates:** the rotational axis is longer than the other ones:

$$a > b = c \tag{3.35}$$

  obtaining a cigar-like shape spheroid, and minimizing the contact surface between the NP and the substrate.

- **Oblates:** the rotational axis is shorter than the other ones:

$$a < b = c \tag{3.36}$$

  obtaining, in this case, a flattened shape, like rotating planets, that maximize the contact surface on the substrate.

Spheroids are generally characterized by their axis ratio AR:

$$AR \equiv \frac{b}{a} \tag{3.37}$$

hence $AR < 1$ indicates a prolate shape while $AR > 1$ an oblate one and, obviously, $AR = 1$ corrsponds to a sphere. In fig. 3.5, an example of oblate spheroid (left) and prolate spheroid (right) is reported.

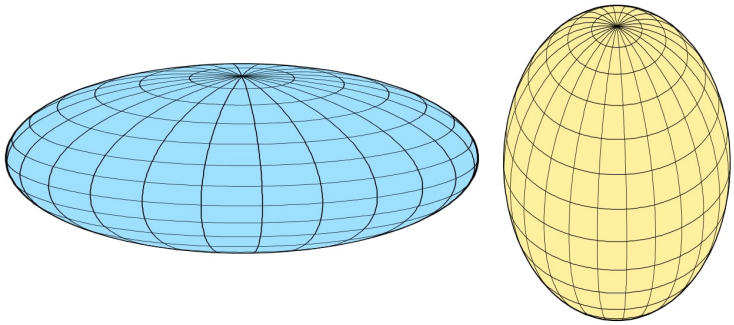

Figure 3.5: *left:* oblate spheroid, *right:* prolate spheroid

The asymmetry of the axes is taken into account by the geometrical depolarizing factor, L_j, where $j = a,b,c$. Because of the sum rule $\sum_j L_j = 1$, only two depolarizing factors are independent.

The electric polarizability, derived in eq. 3.15 for the spherical case, in the quasi-static approximation for a field parallel to the j-axis is [164]:

$$\alpha_j(\omega) = \varepsilon_0 \frac{\varepsilon(\omega) - \varepsilon_m}{\varepsilon_m + (\varepsilon(\omega) + \varepsilon_m)L_j} V \tag{3.38}$$

where V, the particle volume, is given by $4\pi abc/3$.

The resonant behaviour of α is still evident, but because of the geometry depolarizing factor, there are three different resonances for the ellipsoid depending on the relative orientation of the particle axis with respect to the direction of the electric field of the electromagnetic wave. Hence, the degeneracy present in the case of a spherical particle is broken. In fact, for any spheroid with $a \neq b \neq c$, up to three resonances will be present, depending on the relative orientation of the particle with respect to the incoming electromagnetic wave.

A consequence of the orientation dependence in eq. 3.38 is that, in principle, it should be possible to excite different resonances by changing the light polarization. For a randomly oriented distribution of ellipsoids with respect to the electric field orientation, it is possible to average eq. 3.38 over all directions. This will give a general expression for the polarizability, without explicit dependence on the j index [164, 165]. As a proof of this, in fig. 3.6 the absorption spectrum for ellipsoid NPs randomly oriented, according to the Gans model is reported. The three resonance peaks present in the spectrum, of about equal amplitude, are due to the plasmonic oscillations along each of the three axes. These peaks can be actually described by a Lorentzian curve by using eq. 3.33. The central peak (dotted line) has been calculated using the Mie theory for Al spheres.

In fig. 3.6, it has been taken into account a sample of randomly oriented generic ellipsoids with an axes ratio of a : b : c $\approx$ 1 : 2.3 : 23. The well-separated peaks are due to the depolarizing factors ($L_a = 0.69$, $L_b = 0.3$ and $L_c = 0.01$).

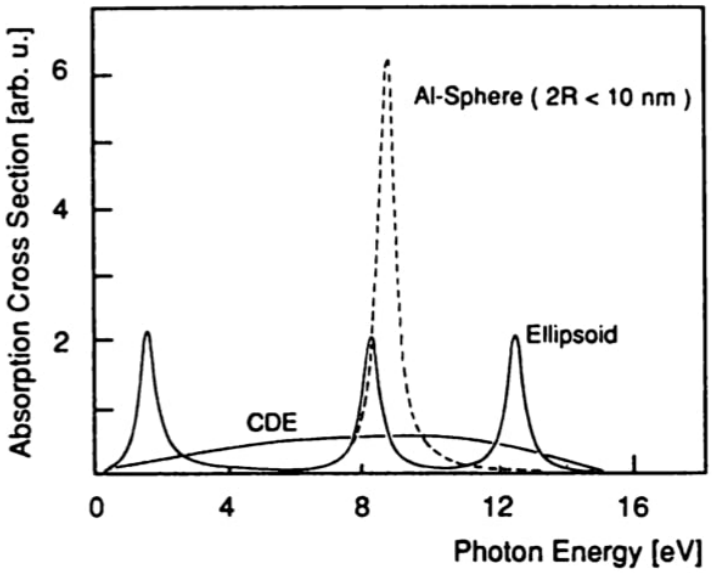

Figure 3.6: Example of absorption cross-section calculated for Al spheres (dotted line, Mie theory) and randomly oriented Al ellipsoid using the quasi-static approximation (Gans model). It is also shown, for comparison, the spectrum obtained with a continuous distribution of ellipsoids (CDE) shapes[154, 166].

If a continuous size distribution is added to the random orientation, the spectrum result in a smoothed, "bump-like" line (CDE curve in fig. 3.6). That means that when there is a population of randomly oriented NPs with different size and geometry, it is not possible to distinguish the single contribution to the spectrum, as a continuous distribution of LSP resonances is obtained. It is worth noting that the three peaks structure is expected to collapse into a two peaks spectrum if the sample of NPs is composed of oblates and prolates ($a \neq b = c$) with different peaks amplitude due to the 2-fold degeneracy of the mode. The extinction cross-section for random oriented nanoparticles in the quasi-static approximation, obtained by eq. 3.5, can be written as [26, 167]:

$$\sigma_{ext}^{Gans} = V\frac{\omega}{3c}\varepsilon_m^{3/2}\sum_{j=a,b,c}\frac{\varepsilon_2(\omega)/L_j^2}{\varepsilon_2^2(\omega)+\left(\varepsilon_1(\omega)+\varepsilon_m\frac{1-L_j}{L_j}\right)^2} \tag{3.39}$$

From ref. [156], assuming a as the rotation axis, the explicit form of the depolarizing factors L_j, in the case of prolate NP, can be written as:

$$\text{Prolates:}\quad a > b = c \Rightarrow \begin{cases} L_a = \frac{1-e^2}{2e^3}\left[\ln\left(\frac{1+e}{1-e}\right) - 2e\right] \\ L_b = L_c = \frac{1}{2}(1-L_a) \end{cases} \tag{3.40}$$

where $e = \sqrt{1 - \frac{b^2}{a^2}}$, while

$$\text{Oblates:} \quad a < b = c \Rightarrow \begin{cases} L_a = \frac{1+e^2}{2e^3}\left[e - \tan^{-1}(e)\right] \\ L_b = L_c = \frac{1}{2}(1 - L_a) \end{cases} \tag{3.41}$$

where now $e = \sqrt{\frac{b^2}{a^2} - 1}$.

By using these relationships and eq.3.39, it is possible to evaluate the extinction cross-section for a set of randomly oriented nanoparticles, like for the case of alkali atoms in a PG matrix with random network of pores [26].

3.5 Surface Plasmon Induced Desoprtion

Light absorption by a metal cluster also provokes the excitation of several vibrational modes [168, 169]. This mechanism is intensified at LSP resonance because of collective behaviour of the conduction electrons. Generally speaking, these oscillations may result in two different ways:

1. when the coupling between the phonons and the surrounding material takes place with a time scale that ranges from few picoseconds to some nanoseconds, the vibrations are damped [170],
2. the oscillations remove from the surface a fraction of the atoms contained in the nanoporous network.

It seems that the exposure of a porous glass loaded with NPs of alkali atoms to a high intensity resonant light does not damage the PG structure [30], as well as an important can be excluded when cluster evaporation takes place. Moreover, in the present work, it can be assumed that only a localized surface is actually heated, even considering the heating transport properties of the alumina and porous glass.

The main usage of this process is the possibility to release atoms from NPs by irradiating the latter with resonant light at a frequency ω_{LSP} [20, 171], obtaining in this way a light-induced desorption process caused, differently with the LIAD, by the LSPs at the cluster surface. Because of the strong relation with the excitation of surface plasmons, this mechanism is called Surface Plasmon-Induced Desorption (SPID) [26, 172].

Similarly to LIAD (sec. 2.4), this process produces an increase of the atomic vapor density, but the mechanism behind it is intrinsically different. The main difference is the resonant nature of SPID and because of LSPs involvement, SPID exhibits a Gaussian shape profile. Moreover, generally it requires relatively high intensity to induce a significant increase in vapor atomic density and it removes only

atomic structures, such nanoparticles, from NPs matrices, due to its resonant character. Therefore, SPID allows, in principle, a selective desorption which is impossible with LIAD since it acts indiscriminately on all the adsorbed atomic species. SPID

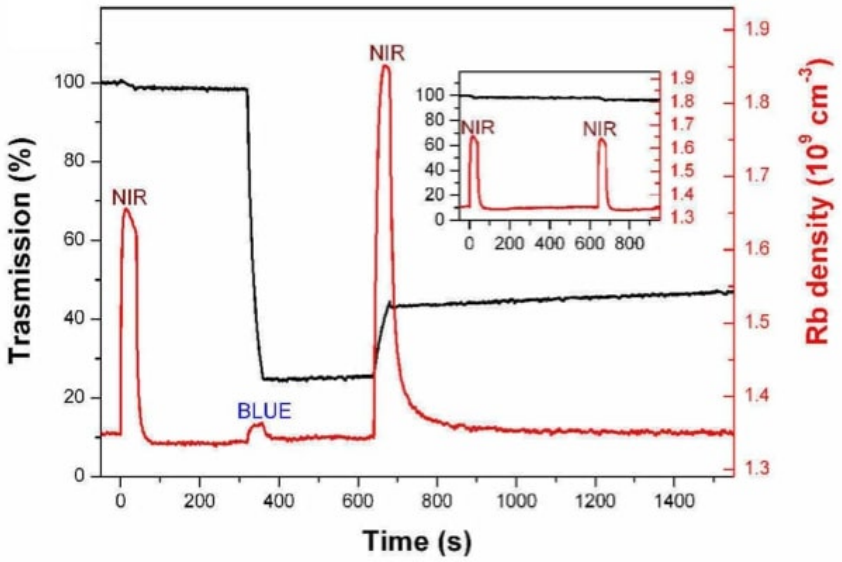

Figure 3.7: SPID effect in a PG loaded with Rb atoms[30] : Rb vapor density *(red line)* and sample transmission at 785 nm *(black line)* after axposure at 5.6mW/cm^2 at 488 nm ("BLUE") and 2.2W/cm^2 at 808 nm ("NIR"). **Inset:** sequence of two exposure to 2.2W/cm^2 at 808 nm ("NIR")

has been demonstrated in different contexts: for Rb NPs from a film immersed in liquid He [173], Na, K and Ag NPs supported on a single-crystal surface [174] and for Rb, K and Cs atoms in porous glasses substrates [26, 111, 113]. It is used in chemical engineering as a catalytic method [175] and it is also exploited for size-selective laser-ablation process to manipulate size distribution of metal NPs [176] and to build up spatial periodic structures in GaAs films [177].

SPID effect has also been used to achieve completely reversible transfer of Rb atoms from layers to nanoparticles and vice versa [30], in this way opening a completely new way for optical storage, considering the sensitivity of the process to the illumination sequence. A demonstration of the vapor density variation under the SPID effect and its influence on the PG transparency, is reported in fig. 3.7 from ref. [30]. In this work a PG matrix is loaded with Rb atoms and then it is exposed to three light pulses, two of NIR light (808 nm) at 2.2W/cm^2, that is resonant with the Rb NPs formed in pores network, and one of blue light (488 nm) at 5.6mW/cm^2. The red line represents the Rb vapor atomic density variation, while the black line the PG transmission at 785 nm. The 808 nm illumination leads to a progressive reduction of absorbing Rb clusters by the SPID and hence the increase of the PG sample transmission.

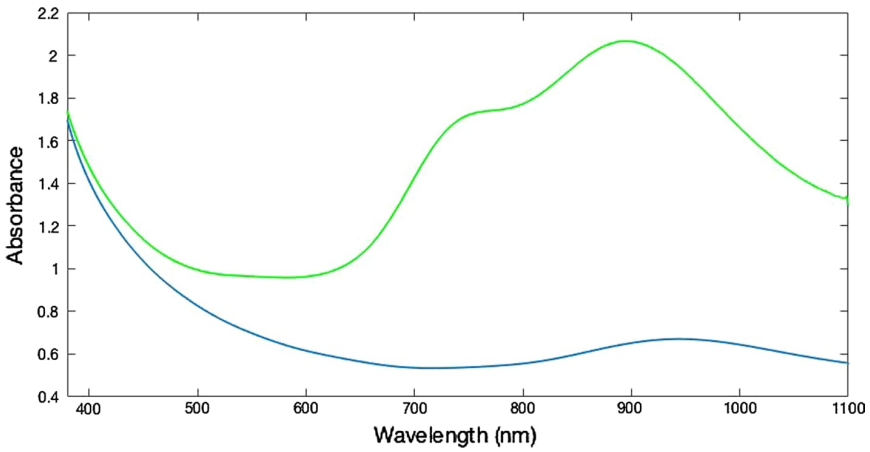

Figure 3.8: Absorbance spectrum of a nanoporous glass sample enclosed in a Rb cell. *Blue curve*: spectrum of the sample before the illumination. *Green curve:* spectrum of the sample after 10 min of illumination of a 50 $\mathrm{mW/cm^2}$ green laser beam at 532 nm [20].

It must be noted that the SPID may be overlapped with the LIAD effect. In fact, once the atoms are desorbed from a surface by SPID, a part of them can be adsorbed again as being part of new cluster structures, and hence desorbed again by SPID, but also can be adsorbed in atomic layers, unaffected by resonant effects. In this way, SPID tends to accumulate atoms into layers and, if the LIAD efficiency is not negligible, these atoms will be removed by non-resonant light desorption, decreasing the concentration of atoms in layers. In this sense, SPID and LIAD can be seen as two effects working in opposite direction, even if the net result is an increase of the atomic vapor density [26].

In fig. 3.8, the absorbance of a porous glass sample with an average pore diameter of $17nm$, in a cell filled with Rb vapor with a density at the equilibrium of $1.6 \cdot 10^9 \mathrm{atoms/cm^3}$, is reported . The absorbance spectrum is taken by using an UV-Vis Spectrophotometer Agilent Cary (see sec. 4.1). The blue line is the response of the sample before the illumination, while the green line is taken after a $10min$ long illumination at $532nm$ and 50 $\mathrm{mW/cm^2}$.

The spectrum evidences two overlapping broad peaks centered at $899nm$ and $751nm$; they are due, respectively, to prolate and oblate ellipsoidal NPs of Rb, which were already revealed in previously experiments [30]. This case can be interpreted by applying the Gans theory in the interaction between light and ellipsoidal metal NPs, which predicts a shift in the atomic line as a consequence of the surface plasmonic resonances [20].

This means that, if a light beam resonant with the absorption plasmonic band of a NP impinges on it, its photons are able to destroy the aggregates by excitation. This is another example of SPID effect. Further details will be given in par. 5.3.2.

Chapter 4

Experimental Apparatus

This chapter presents a detailed description of the experimental apparatus exploited for this work. The details are provided in order to have a background in order to fully appreciate the data obtained and their interpretation, as given in the following chapter.
A first introduction on the setup is given in sec. 4.1. In the following sections, technical features of the instrumentation, as well as a description of the Data Acquisition (DAQ) system and of the data analysis procedure, will also be provided, in order to supply a background for the interpretation of the data.
In sec. 4.1.1 the light sources used to activate the LIAD effect and to study the porous matrices are described more in details. Sec. 4.2 is dedicated to the data acquisition system, both the hardware construction and the software development.

4.1 Instrumentation

The apparatus where the experiments have been performed consists of a vacuum chamber made by a low degassing stainless steel six way cross, closed with CF63 flanges, plus two CF35 feedthrough flanges for the electrical connection. The chamber is completed by the connection ports towards the vacuum pumping system and the pressure measurement components. The scheme of the setup is shown in fig. 4.1.

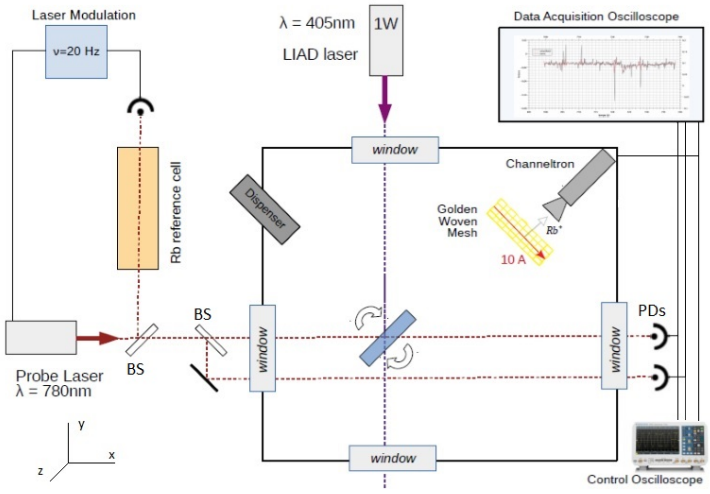

Figure 4.1: Schematic representation of the experimental apparatus. The dashed red-line shows the probe laser beams path. The dashed violet line corresponds to the desorbing laser beam propagation. BS = Beam Splitter.

Along the $\hat{x}$ and $\hat{y}$ direction, the chamber ports are closed by optical quartz windows, allowing, respectively, the transmission of the probe laser beam and the desorbing laser beam. The sample is placed in the chamber through a home-made PVC holder, in such a way to select any direction respect to the laser beams. By means of a steel rod connected to the PVC holder through the flange, it is possible to translate and rotate the sample along/around the $\hat{z}$ axis and also to tilt it by 90° along the $\hat{x}$ axis, by an electromagnet placed along the rod. This last choice allows for a correct placement in view of the loading process. Fig. 4.2a, 4.2b show the lodging of the sample into the chamber, from two orthogonal points of view, the side window and the top window, respectively.

Through the CF35 flanges, on the **xz**-plane at about 45° with respect to the sample, the Rb dispenser produced by the SAES Getters Group and a Photonics R 5901 Magnum channeltron, connected to an high voltage supply, are placed .

The Rb dispenser is placed at $2-3$cm from the sample in order to maximize the loading efficiency. By heating the dispenser with a current flow of the order of a few Amps, because of the Joule effect, Rb atoms are emitted in vapor phase. Up to $4.5A$ the dispenser temperature is dependent on the environmental temperature [178]. In fig. 4.3, the current/temperature plot, as given by the producer SAES, is reported .

A qualitative measurement of the Rb emitted by the dispenser and how long the same lasts in the chamber has been made by using the VitaWave ECDL7830 R $780nm$ laser source (see par. 4.1.1).

In the apparatus used for this experiment, the Rb emission was detectable from about $4A$ for a fresh dispenser. As usual, the current has to be progressively increased

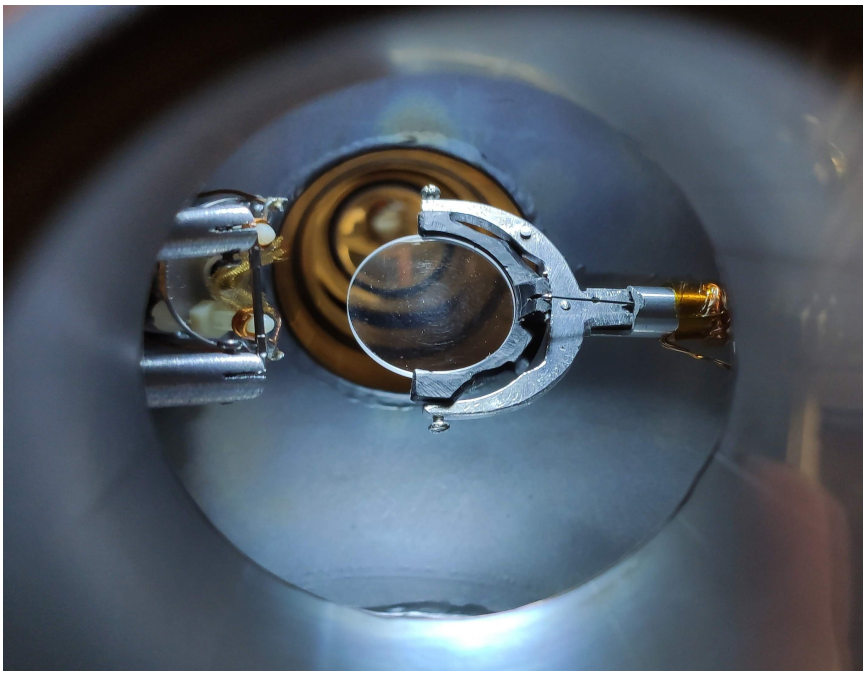

(a)

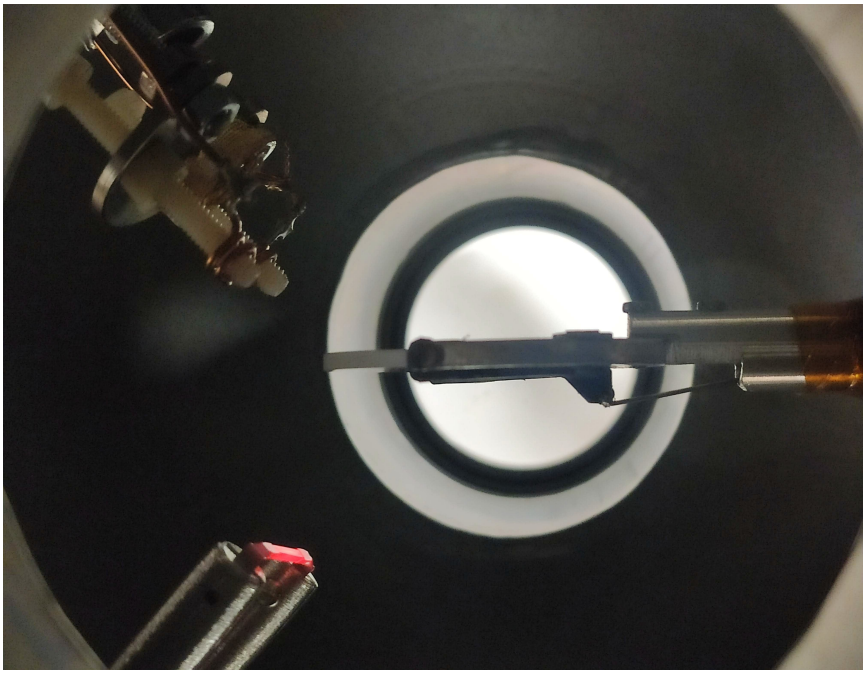

(b)

Figure 4.2: **(a)** View of the alumina sample in the chamber along the $\hat{x}$ axis. On the left in the foreground can be see the Rb dispenser while in the background the golden mesh placed in front of the channeltron window. **(b)** Top view of the chamber: on the bottom left of the image the glowing red dispenser can be seen, while on the top left the golden mesh and the channeltron are distinguishable.

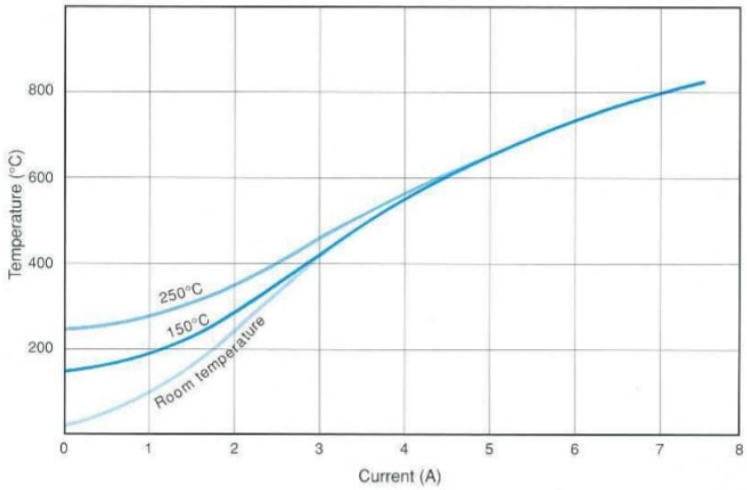

Figure 4.3: Temperature vs current plot for alkali metal dispensers as a function of the tube temperature [178].

for obtaining the same atomic yield because of the degradation of the dispenser during its usage. The experimental data of this work have been taken with current values in a range of $5-7A$, depending on the degradation of the dispenser, in order to obtain a constant Rb emission during the time needed for the measurement.

The Channeltron Electron Multiplier (CEM) is a continuous dynode electromultiplier, as schematized in fig. 4.4. In order to detect positive ions (Rb^+), the input is kept at a negative potential of $-2490V$ and the output is at ground. This device is used to detect charged particle, both positive or negative according to the voltage supplied to the electrodes. When a charged particle strikes the input face of the device typically produces 2-3 secondary electrons. These electrons are accelerated down the channel by a positive bias while hitting the channel walls producing additional electrons for an output pulse of 10^7 to 10^8 electrons[179].

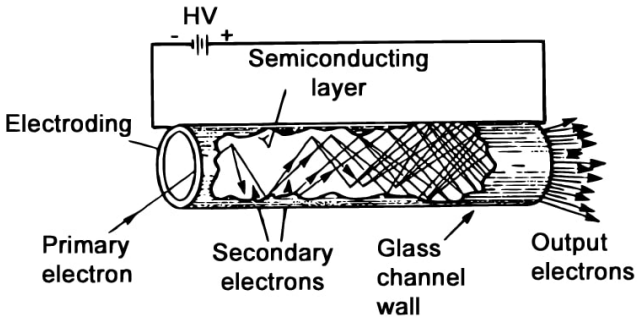

Figure 4.4: Scheme of electron-multiplier[180].

It is therefore necessary to ionize neutral Rb. To do that, in front of the channeltron, a 99.9% pure golden woven mesh kept at high temperature by a current

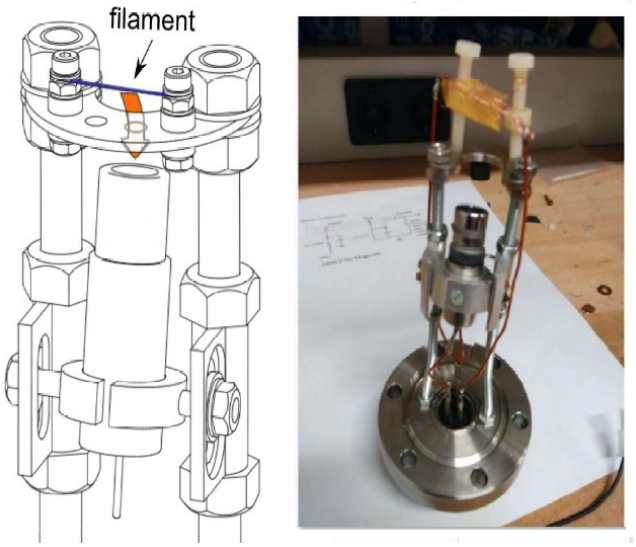

Figure 4.5: Scheme and picture of the electron-multiplier mounted on its support .

flowing has been placed. The mesh intercepts the neutrals atoms coming in the channeltron input window and ionize them. The measured signal is proportional to the ionized particles arriving on the channeltron. The arrival of an ion on the channetron will cause an increase in amplitude of the output voltage signal. The channeltron is power supplied via the second CF35 flange and it is mounted on an home made support which is used also to keep the golden woven mesh in front of the channeltron input, as can be seen in fig. 4.5.

In order to get a Ultra High Vacuum (UHV) condition in the chamber, two pumps put in series have been employed. The first one is a rotary vane pump used to reach a preliminary pressure of the order of $10^{-2} - 10^{-3}$mbar. The second one is a Turbomolecular Pfeiffer TC600 pump, allowing for a limiting pressure of $7 \cdot 10^{-8}$ mbar when the Rb dispenser is not active. Switching on the dispenser increases the value of the pressure up to about $7 \cdot 10^{-7} - 9 \cdot 10^{-7}$ mbar.

Since the LIAD effect causes a release of atoms in the vapor phase, it would be interesting to know how much time the atomic cloud survives in the chamber. The desorbed atoms have two ways out:

- re-adsorption on the chamber walls,
- exit by the pumping port,

Both these processes contribute to the lifetime of the atoms in the gas phase: with a proper measurement strategy this two contributions can be separated and estimated.

By using a flash to induce the LIAD effect from the chamber walls, which are filled by Rb adatoms after several loading processes by the dispenser, two measurements have been performed by acquiring the transmission signal of the diode laser

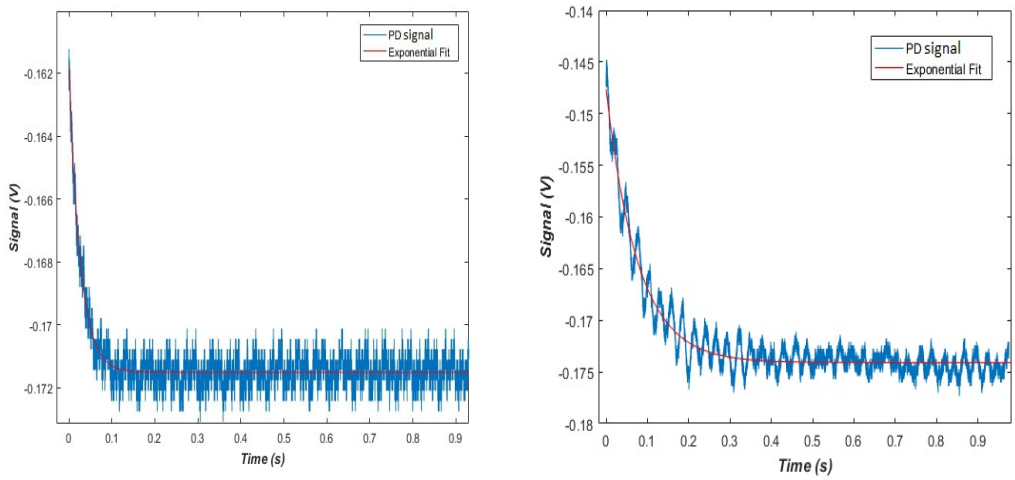

(a) $\tau_{open} = 26.6 \pm 0.2ms$ **(b)** $\tau_{close} = 81.1 \pm 0.3ms$

Figure 4.6: Fitting of the flash light LIAD signal of Rb. **(a)** Pumping valve opened **(b)** Pumping valve closed.

crossing the chamber by a photodiode. The diode laser is tuned on the maximum of one of the resonance Doppler broadened hyperfine ground peaks; the photodiode is screened by the environmental light by an interference filter at $780nm$. The first measurement has been obtained with the valve connecting the chamber to the pumps opened and the other one with the valve closed. The results are reported in fig. 4.6. The t = 0s corresponds to the maximum of the flash, that lasts about $2ms$.

The signals have been fitted with an exponential function in the form $A \cdot e^{-t/\tau}$, in order to get the value of the typical lifetimes τ. The results show that without the pumping system (fig. 4.6b) the decay time is more than three times larger. We can conclude that $\cdot 1/\tau_p$ gives an estimation of the pump rate, while $\cdot 1/\tau_{ads}$ is an estimation of the adsorption rate. The time τ_{ads} is a function of the geometrical parameters of the chamber and of the Rb - stainless steel van der Waals interactions. If one consider:

$$1/\tau_{open} = 1/\tau_p + 1/\tau_{ads} \tag{4.1}$$

$$1/\tau_{close} = 1/\tau_{ads} \tag{4.2}$$

the value of τ_p can be easily obtained by substituting eq. 4.2 in eq. 4.1, obtaining then a value of $\tau_p = 39.6ms$.

In order to measure the absorbance (defined in eq. 2.12) of the samples, before and after the exposition to the Rb vapor, and to verify the eventual presence of nanoparticles in the porous films, an Agilent Cary 60 UV-Vis Spectrophotometer has been used .

It makes use of a xenon flash lamp at 80 Hz, with a spectral range of $190nm -$

1100*nm* and a spectral bandwidth of 1.5*nm*. A beam splitter generates two beams in order to use one of them as a reference for the calibration. An internal monochromator decomposes the white beam, and two silicon photo detectors simultaneously record the sample beam and the reference beam intensities (fig. 4.7a). The light beam size corresponds to a surface of less then 1.5 mm $\times$ 1.0 mm at its focal plane.

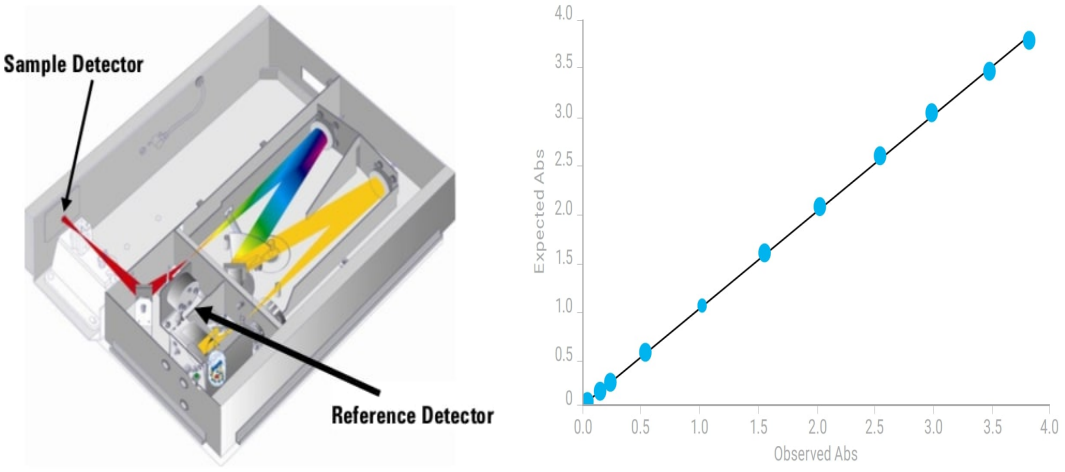

(a) **(b)**

Figure 4.7: **(a)** UV-Vis Spectrophotometer Agilent Cary 60. **(b)** Photometric range extends for 3.5 absorbance units mantaining its linearity.

The measured signal depends both on the transmittance of the sample and on luminosity of the xenon lamp B. The intensity of the bare light beam (in absence of any sample), I_0, and the reference beam I_{ref} are both proportional to B:

$$I_0 = k_1 \times B \tag{4.3}$$

$$I_{ref} = k_2 \times B \tag{4.4}$$

where k_1 and k_2 are two proportionality factors.

The transmittance will be then $T_0 = I_0/I_{ref} = \beta$, as calculated by the dedicated software CARY Win-UV for each wavelength, together with a conversion of the transmittance into absorbance, *abs*. This provides the baseline to be subtracted to the acquired data.

The resulting absorbance of the sample will be then obtained with the following equations:

$$T_{sample} = T_0 \times \frac{I_{sample}}{I_{ref}} \tag{4.5}$$

$$abs_{sample} = -\log_{10} T_{sample} \tag{4.6}$$

In fig. 4.8 it is shown the schematic representation used to illuminate the PG sample

before the spectra analysis with the UV-Vis Agilent spectrophotometer. The diverging lens is used to enlarge the laser beam in order to cover a larger surface of porous glass.

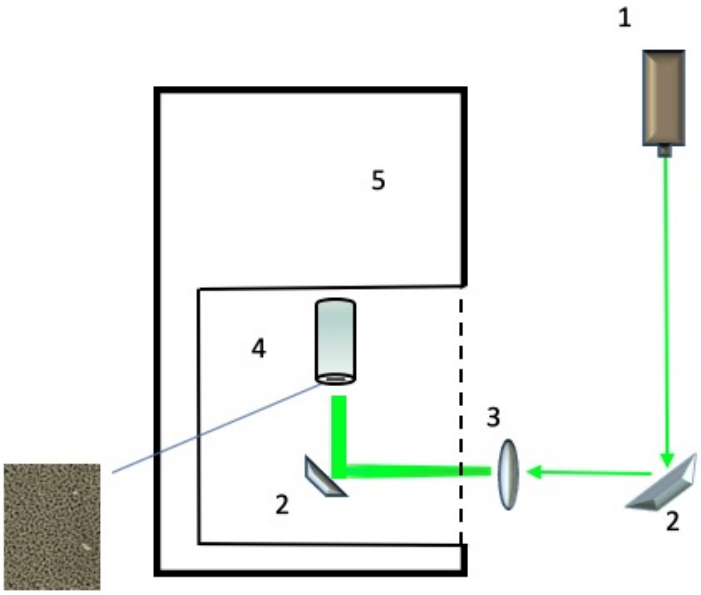

Figure 4.8: Experimental setup:*1)* light source, *2)* mirrors, *3)* diverging lens, *4)* cell containing the PG sample, *5)* spectrophotometer.

In the following sections the other components of the apparatus and their usage will be described more in details.

4.1.1 Light Sources

During the experimental work different lasers have been used, each of them with a different purpose. Since the light sources are an integral part of the experiment, this section is dedicated to describe the characteristics of the sources used.

The laser used as a probe beam is an external cavity diode laser system VitaWave ECDL7830 R which has a declared output power of 15 mW at 66 mA operating current. The beam shape is elliptical with a waist of 5×1.5 mm^2. The frequency of the beam can be modulated by scanning either the voltage of a piezo-element, which changes the incident angle formed by the laser beam with the external diffraction grating (working at the second order) [181] or/and the Laser Diode (LD) current.

The laser beam has a bandwidth of about 500 kHz. In the usual settings, the intensity of the laser beam is strongly attenuated in order not to have both optical pumping and saturation effects on both the vapor and the signal.

This laser has been used both modulated over the Rb spectrum, as reported on the right side of fig. 4.9, and tuned on the absorption maximum of a single resonance of the Rb, in particular on one of the two transitions of the D_2 line of the isotope ^{85}Rb, starting from either the level $F_g = 3$ or $F_g = 2$. In the first case, the peak has the higher amplitude, in the second one the peak is more isolated in frequency from the other resonances.

The hyperfine structure of the excited level is hidden by the Doppler broadening, of the order of 500 MHz; it results impossible to discriminate the hyperfine excited peaks.

A single mode diode free running diode laser SDL-5401-G1 with a wavelength of 852 ± 10 nm, a declared output of 50 mW and a spectral width of 3 nm was also used. This wavelength has been employed since it is resonant with the Rb nanostructures but not resonant with the Rb atoms.

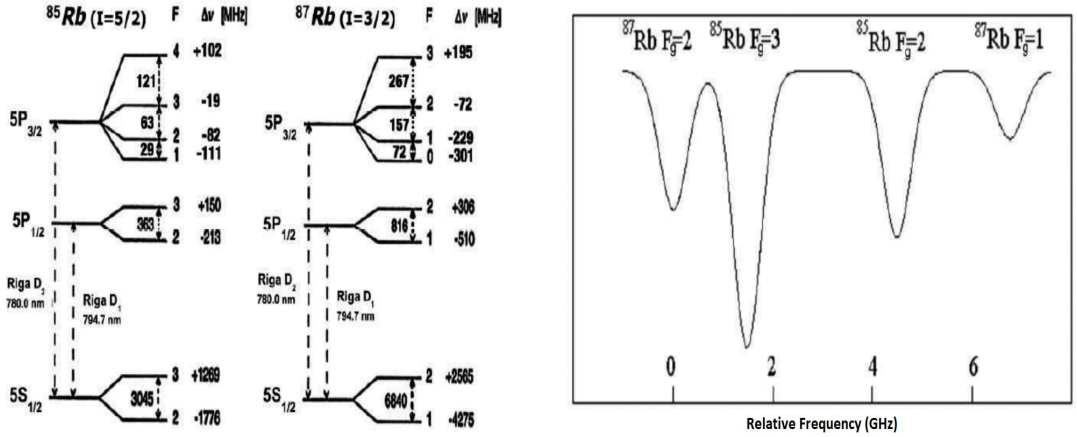

Figure 4.9: (Left) Scheme of the D_2 and D_1 lines of the ^{85}Rb and ^{87}Rb. (Right) Experimental recorded spectrum of the D_2 line of a mixture of of Rb isotopes.

As can be seen in fig. 4.1, the probe laser is divided by a beam splitter (BS) 90/10 placed in front of the laser diode. The weaker beam is sent in a reference cell filled with a natural mixture of ^{87}Rb/^{85}Rb isotopes, whose respective fractions are 72.2% and 27.8%, in order to easily tune the laser on a resonance frequency.

Depending on the measurement to be performed, the laser beam can be further split by a second BS 50/50 placed just before the entrance window of the chamber, as shown in fig. 4.1. Both the beams cross the chamber, passing either through the alumina sample or beneath the sample. This is done in order to have a background (or blank) signal and discriminate eventual fake signals that can be due to some noise source, as , for example, by a drift in the laser wavelength, or a contribution of

LIAD from the cell walls.

In order to obtain a desorbing effect which is independent on the plasmonic resonances, and able to induce the nanostructure formation inside the nanoporous network, a laser source whose wavelength emission lies as far as possible from the Rb plasmonic resonance IR peaks has been chosen, with an accompanying request of the highest possible output power.

The laser selected for the desorbing effect and for the building of the nanostructures is a continuous wave (CW) diode laser CNI laser-III-445, whose output wavelength is in the blue-violet zone of the visible spectrum, at 445 ± 5 nm, corresponding to a photon energy of about 2.7 eV. The maximum output power is $1W$ for an ellipsoidal beam shape of $< 2.5 \times 5.2$ mm^2 at the output coupler.

The controller of the laser does not allow for modifying the current (and the power), hence both the frequency and the intensity can not be modulated. In order to have a control on the power delivered on the sample, a round variable neutral-density filter has been placed in front of the diode laser. The laser is placed on a dedicated holder above the chamber and the beam crosses the sample along the $\hat{z}$ axis.

For the same kind of application, a CW diode pumped Nd:YAG solid state laser has also been used, operating at the second harmonics, $532nm$, with a maximum output power of $150mW$. The diameter of the laser spot at the output is $\simeq 0.9$ mm.

For inducing the LIAD effect only, since it is not required a coherent light source, a flash SUNPAK auto zoom 3600 has been used which has a duration of the peak of the about 2-3 ms.

For what concerns the study of the porous glass in alkali vapor cells, described in section 5.3 different light sources have been employed to illuminate the PG:

- Manual Tunable Littman-Lion System Infra-red laser with emission wavelength in a range of 750-1064 nm. The laser has been tuned on two wavelengths for the measurements: 986 nm at a 60 mW output power, 950 nm at a 65 mW output power.
- DLX 110 TOPTICA High-Power Tunable centered at 780 nm, a single mode external cavity diode laser, with a maximum output power of 1 W.
- High pressure Hg vapor lamp at 340 mW. It emits white continuous light with a strong near-UV component in the range $300 - 450$ nm with the maximum intensity at 380 nm.

4.2 Acquisition method

Amplified Photo Diodes (PD) are used to acquire the probe laser transmission signals. Each PD is equipped with an interference filter as a narrow pass band filter, centered at 780nm and a 20nm bandwidth, in order to remove any stray light.

The output electrical signals from the PDs are split in two branches: one goes to a LeCroy 9304AM digital oscillope, which features a four channels input and a bandwidth of 200MHz, for an online screen visualization of the behavior. At the same time, the other is collected by a data acquisition system on the PC, i.e. is sent to a NI USB 6210, a compact device with 16 available channels, a single channel maximum acquisition rate of 250 kHz and a time resolution of 50 ns.

4.2.1 MATLAB Software Acquisition System

The acquired data are then processed with a Matlab dedicated program.

The raw data from the photodiode intrinsically present a white gaussian noise, mainly due to the impedance of the PDs, so each point can be written in the form:

$$y_i = f(x_i) + \varepsilon_i \tag{4.7}$$

where $f(x_i)$ is a function of the x_i and ε_i is the noise indipendent on the x_i.

In order to extract the signal out of the electrical noise present in the acquired data, two statistically smoothing method have been used: the *Standard Moving Average* (SMA) and the *Locally Weighted Scatterplot Smoothing* (LOWESS).

SMA is a simple, but strong method. It consists in averaging a set of points $y(i)$ over a certain span, according to the following equation:

$$y_s(i) = \frac{1}{2N+1}(y(i-N) + y(i-N+1) + \ldots + y(i) + \cdots + y(i+N)) \tag{4.8}$$

where $2N+1$ is the span of the SMA.

By taking, for example, a span $2N+1=5$, the first four smoothed points $y_s(i)$, according to eq. 4.8, will be:

$$\begin{aligned} y_s(1) &= y(1) \\ y_s(2) &= \frac{y(1)+y(2)+y(3)}{3} \\ y_s(3) &= \frac{y(1)+y(2)+y(3)+y(4)+y(5)}{5} \\ y_s(4) &= \frac{y(2)+y(3)+y(4)+y(5)+y(6)}{5} \\ &\vdots \end{aligned} \tag{4.9}$$

Therefore, the problem reduces to find the appropriate span to be applied.

As an example, in fig. 4.10 the smoothing of a LIAD signal obtained with the flash is reported; 3 different spans, respectively 0.1%, 1% and 10% of the total points have been chosen. It must be noted that by increasing the value of the span, the peak amplitude (in this case, due to the electrical noise introduced by the flash light) decreases, until it even disappears in fig. 4.10c.

The second method, namely the LOWESS, is often used in statistical applications and for noisy data [182]; it is a non-parametric regression, well suited when the signal or the noise taken into account presents a strong non-linear trend. In these situations the linear regression is not recommended. As already stated, our noise ε_i, is independent on the x_i and it is, in general, non linear.

The idea behind LOWESS method is that for each x_i one tries to estimate $f(x_i)$ by using its k-nearest neighborhoods, $x' = x_{i-k}, x_{i-k+1},..., x_{i+k}$. The k nearest neighbors are found by using a simple Euclidean distance, obtaining in this way an ordered set D.

Then the set D of the k distances must be converted into an ordered set W containing weights that will be later used in the linear regression process. The weight function $w(x)$ is defined by the tri-cubic expression:

$$w(x) = \begin{cases} (1-|x|^3)^3 & \text{for } |x| \leq 1 \\ 0 & \text{for } |x| \geq 1 \end{cases} \tag{4.10}$$

that it is positive only for $|x| \leq 1$. The function $w(x)$ must be then normalized to the maximum value observed in the set D:

$$w(x) = \begin{cases} (1-|\frac{d(x,x')}{max_i d(x_i,x')}|^3)^3 & \text{for } |x| \leq 1, x_i \in D \\ 0 & \text{for } |x| \geq 1 \end{cases} \tag{4.11}$$

where $d(x,x')$ is the distance between x and its kth neighbour x'.

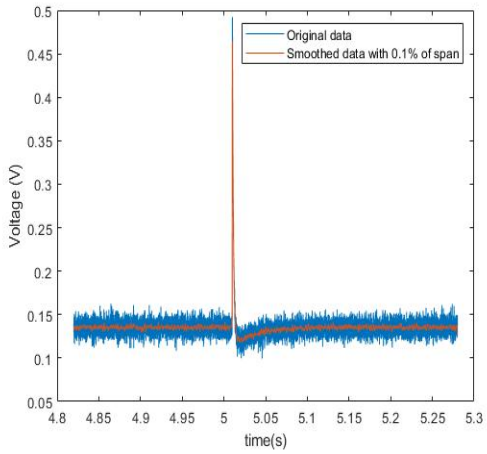

(a) 0.1 % of span

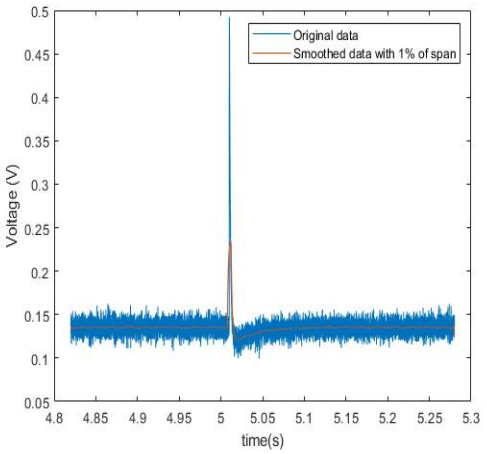

(b) 1 % of span

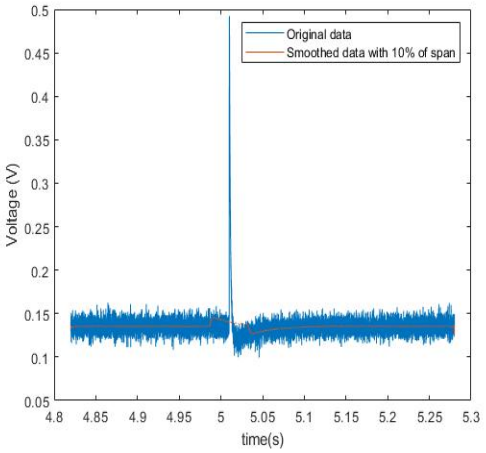

(c) 10 % of span

Figure 4.10: Smoothed data using the SMA with 3 different span values.

The effect of eq. 4.11 is to associate higher weights to shorter distances hence to a distance $d(x,x)$ will correspond a weight $w(x) = 1$.

These weights are then used to set up a linear regression model that will calculate, for each x', the corresponding output y', using the k nearest neighbors of x'. The local linear regression models a polynomial of degree $g = 1$: $\hat{y} = \beta_0 + \beta_1 x$.

In the case of a linear without weight function the relation to use is:

$$\beta = (X^\intercal X)^{-1} X^\intercal Y \tag{4.12}$$

where β is a vector of the linear parameters and X is the matrix containing all the measured x, with dimension $n \times m$ where n is the number of measurements and m the observations of each one:

$$X = \begin{pmatrix} x_1^{(1)} & x_2^{(1)} & \dots & x_n^{(1)} \\ x_1^{(2)} & x_2^{(2)} & \dots & x_n^{(2)} \\ \vdots & \vdots & \ddots & \vdots \\ x_1^{(m)} & x_2^{(m)} & \dots & x_n^{(m)} \end{pmatrix} \tag{4.13}$$

Once obtained the vector β, the new value of the y may be calculated by:

$$\hat{y} = \beta^\intercal X \tag{4.14}$$

In our case, we wish to introduce the weights $w(x)$; from eq. 4.11, the terms of the vector β become:

$$\beta = (X^\intercal W X)^{-1} X^\intercal W Y \tag{4.15}$$

where W is the diagonal matrix of the weights $w(x_i)$.

The detailed MATLAB code used for the acquisition and study of the LIAD dynamics is reported in appendix A.1.

Chapter 5

Experimental Results

In this chapter the data obtained during my PhD work period will be presented. The discussion will be around both the techniques used to acquire the data and how they are processed and interpreted. The chapter will be divided according to the kind of sample analyzed. In par. 5.1 two types of PG have been studied: the Vycor 7930 in 5.1.1 and the 200nm pore diameter glass in 5.1.2. In par. 5.2 the results obtained on the alumina samples are reported, more specifically the 100nm thick sample in 5.2.2 and the 300nm thick sample in 5.2.1. Finally, in sec. 5.3 the results obtained from a porous glass integrated in a cell filled with alkali vapor, in particular Na (in par.5.3.1) and Rb (in par. 5.3.2), are presented and discussed.

5.1 Nanoporous Glasses

The first part of this chapter is about the study of PGs samples, in particular Vycor 7930 and a sample of porous silica. The Vycor glass is generally composed of 96% Sio_2 and 4% B_2O_3. The specific sample used for this work is a Vycor 7930 whose composition, as anticipated in sec. 2.1.2, is SiO_2 (96%), B_2O_3 (3%), Na_2O (0.4%) and traces of other compounds, such as Zr_2O, which are due to the leaching process. Its size are a diameter of 10.0*mm* and a thickness of 2.0*mm*. The average pore size is declared to be 4*nm*; the volume porosity is 28%.

The other sample of porous glass consists in a disk of pure porous silica (SiO_2) with an average pore size of 200*nm*, a diameter of 30.0*mm* and a thickness of 2.0*mm*.

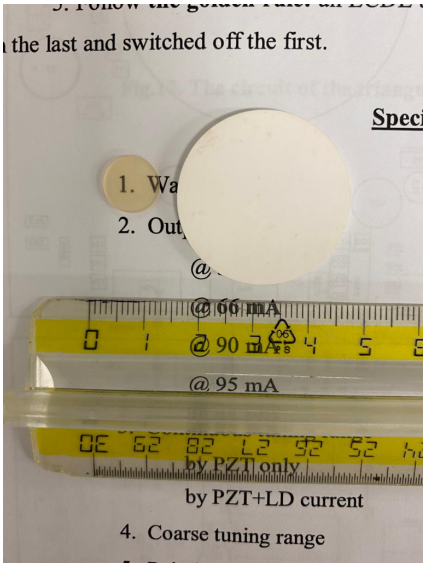

Figure 5.1: Comparison between the Vycor 7930 *(left)* and the porous silica *(right)* samples.

As can be seen in fig. 5.1, the samples, in particular the porous silica sample, are not transparent to the visible light. The whitish color of the silica depends on the larger dimension of the pores which allows for a better diffusion of visible light at the air/glass interface. As a consequence, we have been forced towards measurements on reflection, instead of transmission. It is worth noting to underline that Vycor has become yellowish during several years after the purchase: the free volume is progressively filled by air and, presumably, water vapor. In fact, when conserved in the most conservative and prudential way, for example either in an envelope or protected by tinfoil, this process seems to be slowed. This choice has needed a rotation of the sample by 45° respect to the horizontal plane, as schematized in fig. 5.2, and the positioning of one of the photodiodes on the window along the y-axis direction, next to 445*nm* laser source.

For what concerns the Vycor, even if it is not completely transparent, it was possible to perform measurement in transmission. In this case, the transmitted laser beam emerges quite diffused but it was sufficient to focus the scattered beam with a proper lens.

Anyway, some of the measurements on the Vycor have been performed by simultaneous acquisition of the reflected and the transmitted beam.

In the next two sections, the measurements and the results obtained on the two different samples are separately reported.

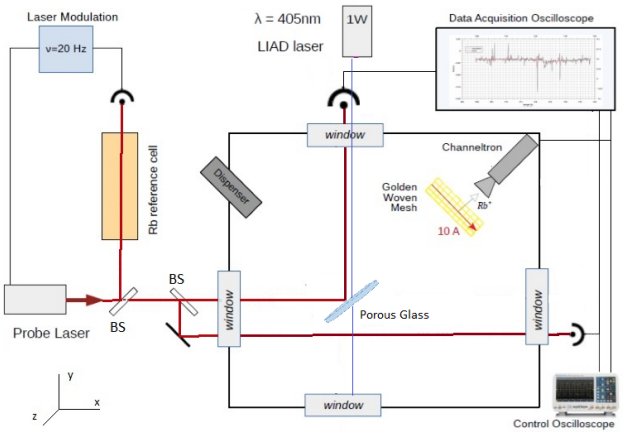

Figure 5.2: Scheme of the apparatus to measure the reflected beam from the PG samples.

5.1.1 VYCOR 7930

In this section the results obtained with the Vycor 7930 sample are discussed. All the measurements have been performed after 3 hours of Rb loading, with a current dispenser in the range $4.5 - 5.0A$. The increase in the current is due to the natural degradation of the dispenser during its usage, for which a higher current in order to obtain the same atomic release is required.

Here, we report on measurements both A) with the ECDL laser scanned at a frequency of $25Hz$ for a frequency bandwidth covering the 4 peaks of the Doppler broadened Rb $D2$ line (as shown in fig. 4.9) and B) tuned on a single frequency, in particular on the maximum of the transition starting from the ground hyperfine level $F_g = 3$ of the ^{85}Rb.

In the following, the reported data have been calculated as the difference between the signal values, as acquired from the transmitted or reflected beam, and the reference beam signal values. This operation has been done in order to remove eventual laser frequency drifts or other noise contributions.

The first measurement lasts $60s$, at a ECDL laser fixed frequency. After about $15s$ from the start, the $445nm$ desorbing laser has been switched on; it hits the sample with a power of about $200mW$ in order to induce the LIAD effect on the sample, and it is kept on for all the rest duration of the measurement. The sample is tilted by 45° respect to the horizontal plane and the ECDL and LIAD laser overlap on the Vycor in the same area. The raw data and the fit are reported in fig. 5.3 as well as the time of lightning of the blue laser.

The absorption signal evidences a small increase, manifestation of a slow desorption of Rb atoms by the porous sample.

The atoms sitting on the surface should be released on a much shorter time

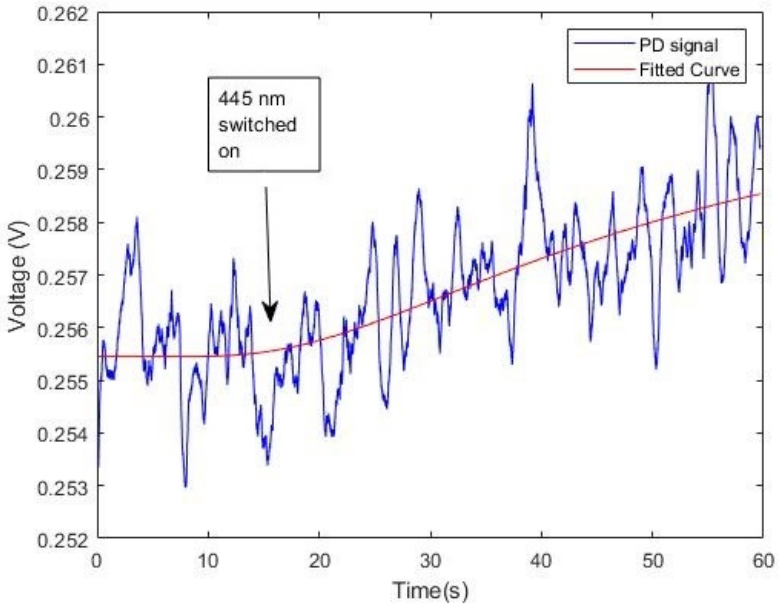

Figure 5.3: Probe laser absorption signal and fit on a 60s measurement.

scale, but there is not any clear contribution by them in the signal. The time scale of the absorption changes indicates the activation of both a detachment from the pore network surface and a diffusion out of the sample. In other words, the inner released atoms in the sample induced by light, diffuse in the nanoporous structure before arriving to the interface and then freely fly into the vacuum chamber. Therefore the problem can be mathematically treated as a diffusion problem in a medium constituted by the pore network: atoms perform several cycles of adsorption/desorption, moving from one another bonding site. Macroscopically, the light changes the diffusion properties [183]. Therefore the data have been fitted with the following function:

$$f(t) = \frac{a}{\sqrt{t}} \cdot e^{-b/t} + c \tag{5.1}$$

The parameter b is physically related to the time interval needed for emptying by Rb atoms the volume fraction irradiated by the laser beam. The result of the fit 5.1 is reported in fig. 5.3; it gives a value $b = 85.65s$. This result may be an underestimation, if considering that the curve has not reached its maximum value.

For this reason, a longer measurement have been repeated in order to try to get a saturation value and/or even a change in the signal derivative. In fig. 5.4a the fit on a set of data from a measurement lasting 900 s is shown. In this case, a small sudden bump at the lighting time seems to be present, The desorbing laser has been switched about 60s after the beginning of the acquisition. It is here evident that the signal starts flattening around time 600s. This is a proof of good loading of the

sample, with atoms able to deeply penetrate in the nanoporous structure. By fitting the data with the function 5.1, a value of $b = 529.25s$ is deduced, much longer than the one obtained in fig. 5.3.

We have simultaneously taken the signal from the channeltron output for a cross check of the optical transmission result. The electrical response is shown in fig. 5.4b. The result was unexpected and needs a completely different explanation. The time behavior of the signal is not synchronized with the Rb vapor density changes. It seems that other species have been ejected by the desorbing light, again accompanied by a diffusion process, characterized by a different diffusion constant. The origin of the signal is probably due to the release of what was inside the sample, rendering it of yellowish color. This adatoms (or molecules) have filled the pore network, also creating some plug or shrinkage in the nanotubes, whose $4nm$ average diameter represents a size comparable with atom aggregates, as seen in other PGs. The bump appeared after around $120s$ suggests a sudden massive release and the beginning of deliverance of the "alien" species in the vacuum volume. The desorption seems to be concluded at the end of the acquisition, after $840s$ of illumination, when Rb still is ejected. A confirmation of this interpretation comes from the visual observation of the sample when extracted by the chamber: its transparency was much higher in the surface area shined by the desorption laser. After several months in the box in air, the sample has become back yellowish. .

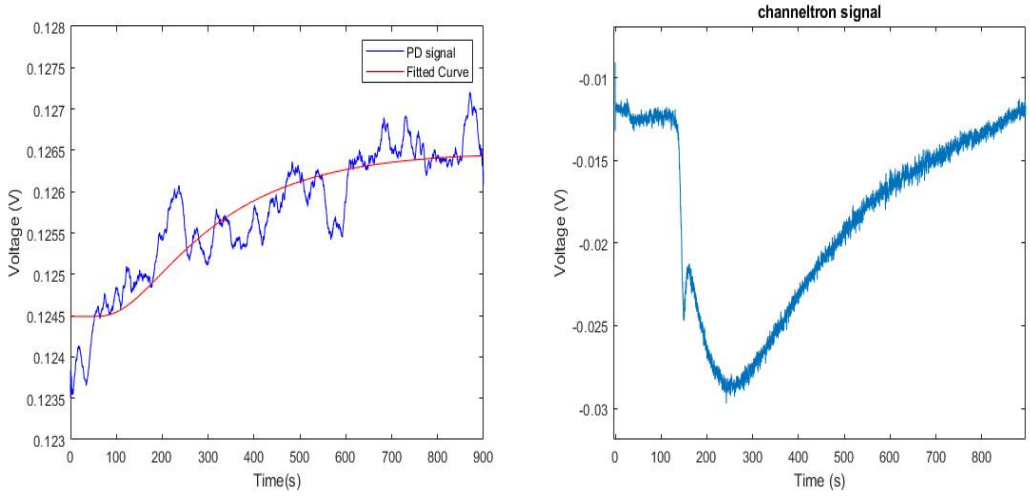

(a) PD signal plot and fitted curve. **(b)** Channeltron signal plot.

Figure 5.4: (a) Fit on a $900s$ measurement. **(b)** Channeltron signal of the same measurement. The signal shows desorption by other species

We have then tried to compare the total detection efficiency of the optical and the electronic systems. In order to do that, other measurements have been performed by sweeping the ECDL current at $25.0Hz$ in order to scan the laser frequency over the natural mixture Rb D_2 line peaks. The modulation has been introduced by a periodic

triangular current change.

In fig. 5.5 the signal of the transmitted and reflected probe beam together with the channeltron output are reported. In this case the desorption source for the activation of the LIAD effect is the light flash.

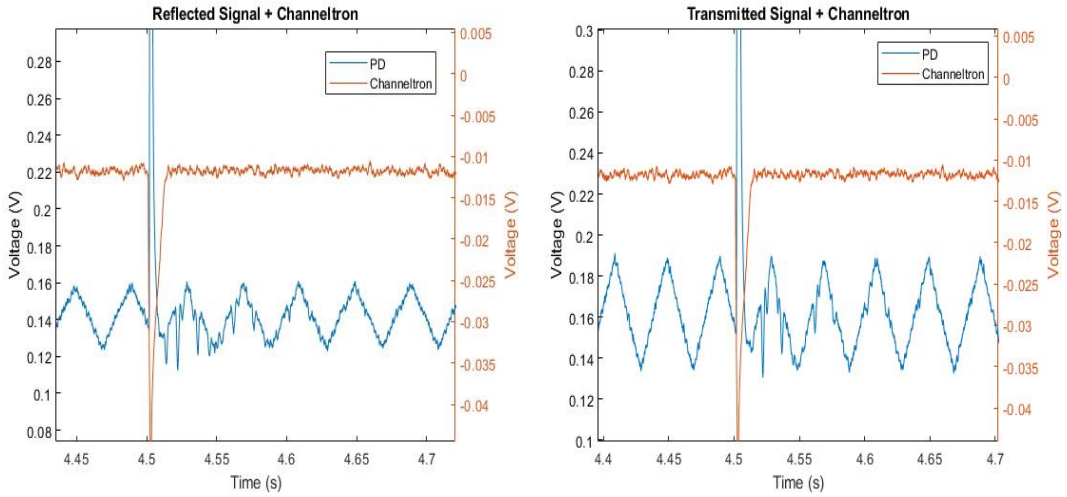

(a) Reflected beam plot + channeltron. **(b)** Transmitted beam plot + channeltron.

Figure 5.5: Plot of the 780 *nm* beam and channeltron during flash LIAD. **(a)** Reflected beam signal. **(b)** Transmitted beam signal.

Both in the transmitted and in the reflected PD response, the typical resonance peaks on the uphills and downhills of the modulation clearly appear. In both cases, the Rb resonances last for almost three frequency sweeps, namely $\simeq 0.12$ s, before being reduced to zero by the loss mechanisms.

For what concerns the channeltron, only a spike ($\sim$ ms) associated to the flash has been recorded, without the equivalent time behavior of Rb. We can conclude that the total detection efficiency of the electronic setup is smaller than that of the optical system. The absolute efficiency of an ionization detection is for sure higher, but the distance of the golden mesh from the sample and the angle of view (the solid angle under which the channeltron sees the nanostructured surface) is pretty small.

5.1.2 200 nm porous size

In this section the studies performed on the porous glass sample with an average pores size of 200*nm* will be reported. As can be seen in fig. 5.1, this sample is completely opaque to light, so all the measurements have been performed by acquiring the reflected beam by tilting the sample of 45°, as sketched in fig. 5.2.

Nevertheless the reflected beam, because of the porous structure and the surface

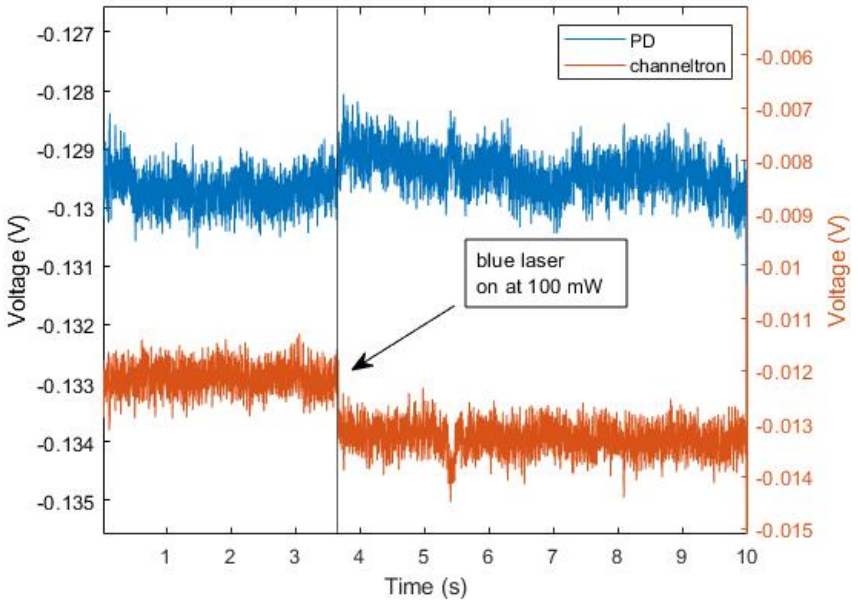

Figure 5.6: Plot of the 780 *nm* reflected beam *(blue line)* and channeltron signal *(orange line)*. The vertical line indicates the moment in which the blue laser has been switched on.

roughness of the sample, results very much diffused and attenuated; a short focal lens was used before the PD aperture. Anyway, the obtained signal resulted more noisy and with a worse signal-to-noise ratio. Because of this, all the measurements reported in the following have been taken without sweeping the laser frequency since the reflected scanned beam would have been impossible to read. Even in this case the Rb loading took 3 hours with a dispenser current in between $4.5A$ and $5.0A$.

In fig. 5.6 a measurement of $10s$ during which the blue laser has been switched on at $t = 3.6$ s is shown. The beam is reflected by the surface directly exposed to the dispenser, so it is expected to be more loaded with Rb with respect to the opposite face.

Both the blue track (photodiode) and the orange one (channeltron) show a bump close to the 445 nm laser ignition.

Another interesting fact is the spike which simmetrycally appears in both registrations at about $t = 5.4$ s. Since it is also evidenced in the channeltron plot, a drift in the laser frequency can be excluded: it seems a sudden and short release of Rb atoms, even if the possible explanation is lacking.

A longer measurement of $t = 20$ s, presented in fig. 5.7, has been done right after the one reported in fig. 5.6; the blue laser has been switched on and off during the acquisition procedure. The channeltron presents a similar step-jump as before, and it goes back to the zero value as soon as the blue laser is switched off. At $t = 13.3$ s there is a spike in channeltron signal of a duration of $1s$. It seemingly appears in the PD

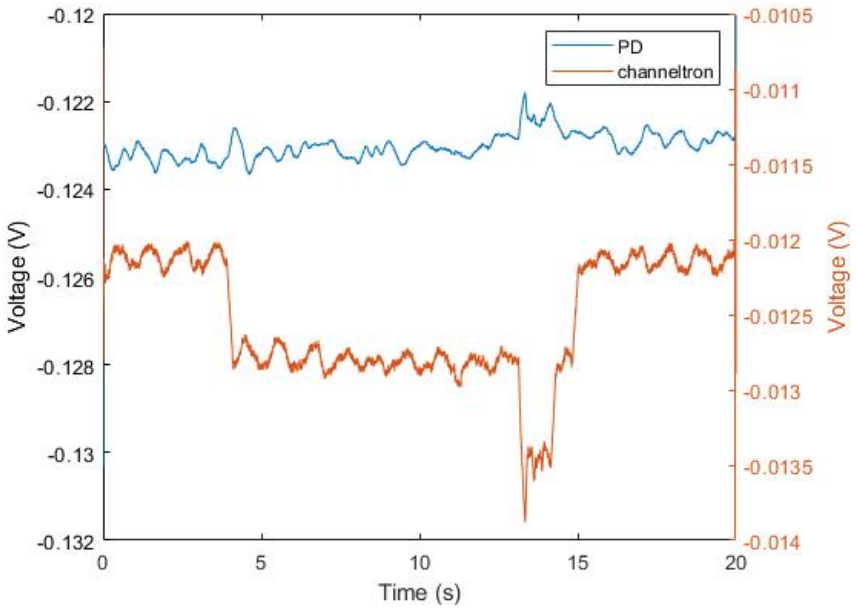

Figure 5.7: Plot of the probe 780 *nm* reflected beam *(blue line)* and channeltron output ionization signal *(orange line)*.

signal; the origin of such a bump cannot be attributed to any physical phenomenon of interest.

Since the 445 *nm* laser spot excites the same area of the sample as the previous measurement, the flatness in the probe laser transmission can be explained considering that the previous illumination completely removed the loaded Rb present in the irradiated are, while the channeltron signal output is due to the detection of some other atomic species.

We decided to compare what happens by shining the sample facet not exposed to the dispenser Rb beam. In fig. 5.8 the corresponding result is reported. Even at the first illumination with the desorbing laser, no appreciable change in the transmission probe laser beam has been detected.

Finally, a control on a much longer time scale has been tempted, in order to detect a behavior similar to the diffusion induced process of the Vycor sample, but, again, no result was obtained.

5.2 Alumina Substrate

In this section the studies performed of the alumina samples with thicknesses of 300 *nm* and 100 *nm* will be reported. The first investigation concerns the dynamics of

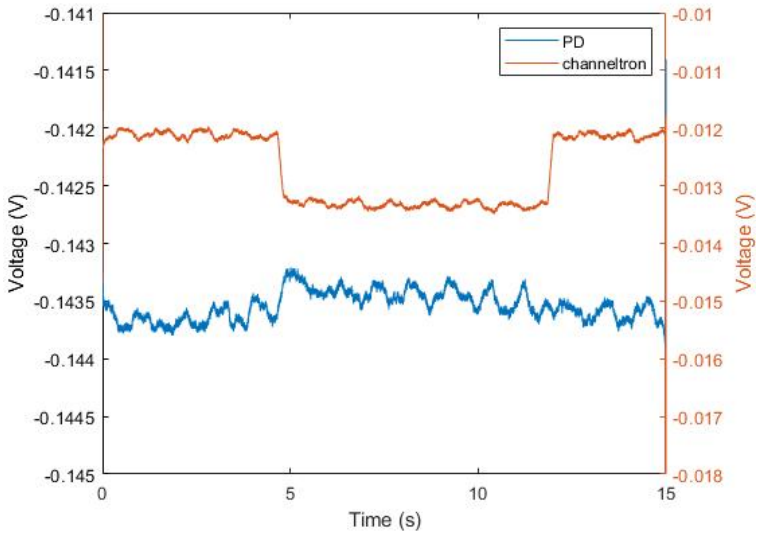

Figure 5.8: Plot of the 780 nm reflected beam *(blue line)* and channeltron output ionization signal *(orange line)*.

the loading process of the samples in order to understand if a scattering process of the Rb beam by the surface is taking place. Anyway, the main finding of this section regards the detected formation of NPs in the nanoporous structure.

We do not have many information about the nanoporous alumina; most of the data of some interest for us have been collected by the researchers of the PhysNano laboratory at the Saint Petersburg National Research University of Information technologies, Mechanics and Optics (ITMO). For example, the adsorption energy for Rb atoms on a substrate of bare sapphire has been estimated by them as $\sim 0.7\ eV$. They have also studied the velocity distribution features of the desorbed atoms, finding that the average kinetic energy decreases for photon energies $> 2.3\ eV$ [184]. This measurement goes against the hypothesis of LIAD as a "photoatomic effect", where we should eventually observe an increase of the square mean velocity.

In fig. 5.9, as a preliminary information, the calculated refractive index $n(\lambda)$ for α-Al_2O_3 from $\lambda = 0.2\ \mu m$ to $\lambda = 2\ \mu m$ [185] is reported. We have replicated in Siena the absorbance spectra for the porous alumina samples. The corresponding plots have been obtained via the Agilent Cary WinUV Software. In fig. 5.10, the spectrophotometer measurements on the samples with alumina thicknesses of 100 *nm* (5.10a) and 300 *nm* (5.10b) are reported together with the comparison with the spectrum of the clean substrate of Al_2O_3 (without any deposition). The wavelength scan ranges from 200 *nm* up to 1100 *nm*. The Optical Density or absorbance on the y axis is defined by the eq. 2.12. Note that the measured Optical Density of the alumina substrate has the same trend of the refractive index in fig. 5.9.

As we have already previously discussed, the substrate shows an almost flat trend in all the IR and visible part of the spectrum with a rise in the UV zone. The 100

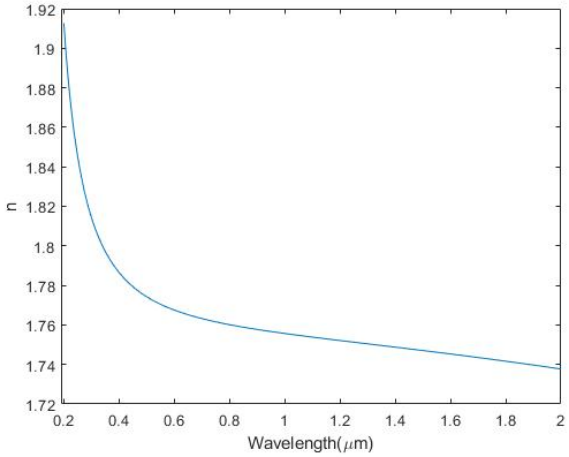

Figure 5.9: Refractive index of α-Al_2O_3[185].

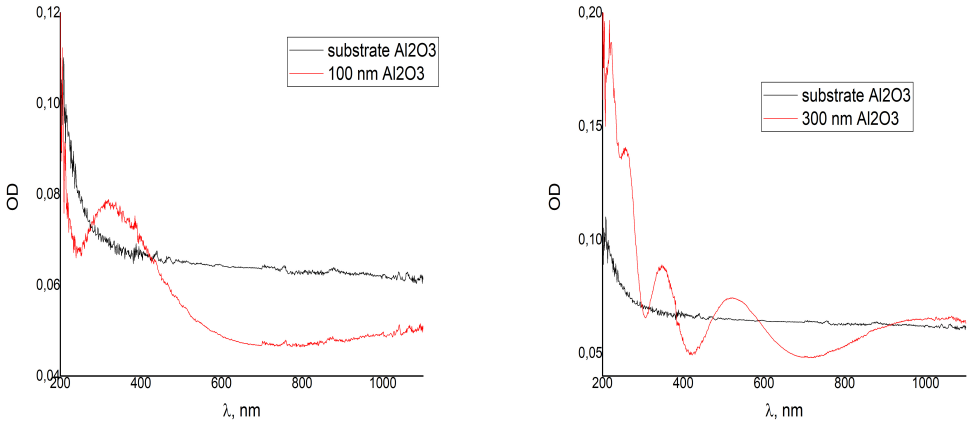

(a) **(b)**

Figure 5.10: Spectral absorbance of the 100 nm and 300 nm alumina samples compared with the spectral absorbance of the α-Al_2O_3 substrate. **(a)**: absorbance of the sample with 100 nm thickness, **(b)**: absorbance of the sample with 300 nm thickness.

nm thickness sample presents a single broad peak around 320*nm*, then the spectrum decreases in the visible and IR zone. Finally, the 300*nm* thick sample presents an oscillatory behaviour, with sharper peaks of different amplitude in the UV and one broad peak centered at 540*nm*. This latter feature gives the motivation for the naked eye observable halo of the 300*nm* deposition.

5.2.1 300 nm

In figures 5.11 and 5.12 the signal obtained, respectively, by the channeltron and the PDs during the loading process of the sample are reported. The dispenser has been left on for about 480s, while the whole data acquisition lasts 600s. We recall here that both PDs detect the probe transmission signal, the first on the same side of dispenser emission, the second one on the other side.

The PDs' data have been fitted with a decay exponential function:

$$f(t) = a \cdot e^{(-b \cdot t)} + c \tag{5.2}$$

In the following table the extrapolated value of $\tau = 1/b$ are reported; this parameter measures the time interval needed to the dispenser to establish a dynamical equilibrium regime for the Rb density.

The angles $\theta = 0°/90°$ refer to the orientation of the sample with respect to the optical table: 0° means that the sample is parallel to the horizontal plane, while 90° means that the sample is vertical, with the alumina surface faced towards the Rb dispenser.

In the table 5.1 τ values as deduced by the exponential fitting procedure shown in fig. 5.11 are reported. While these lifetimes are comparable between the two photodiodes, as expected, (the final density has to be detected in the same way by the transmission probe beams), there is a large difference between the two inclination measurements. This can be explained in terms of a dependence of the total loss rate for Rb from this apparently simple geometrical factor. Indeed, the beam scattering from the sample becomes a relevant phenomenon and can be indirectly estimated. In fact, an inclination of 90° favors both the adsorption of Rb atoms onto the surface as well as the scattering of Rb atoms in the chamber. Therefore, due the second process, the number of atoms towards the channeltron input increases. All these atoms disappear from the chamber and a new loss rate is introduced. Therefore, the higher number of atoms scattered, and arrived on the channeltron brings to an increase in the time needed to establish an equilibrium condition between the incoming flux of Rb from the dispenser and the atoms lost by the various mechanisms.

In the fig. 5.12 the acquisition of the channeltron output for the same measurement of fig. 5.11 is shown. These signals give a confirmation of the previous interpretation.

The sharp peaks in both the measurements are due to the sudden release of spurious elements by the fresh Rb dispenser. These atoms/molecules are detected by the channeltron since they are getting ionized by the golden mesh in the same way as the Rb atoms. By the way, we want to concentrate here on the maximum value of the

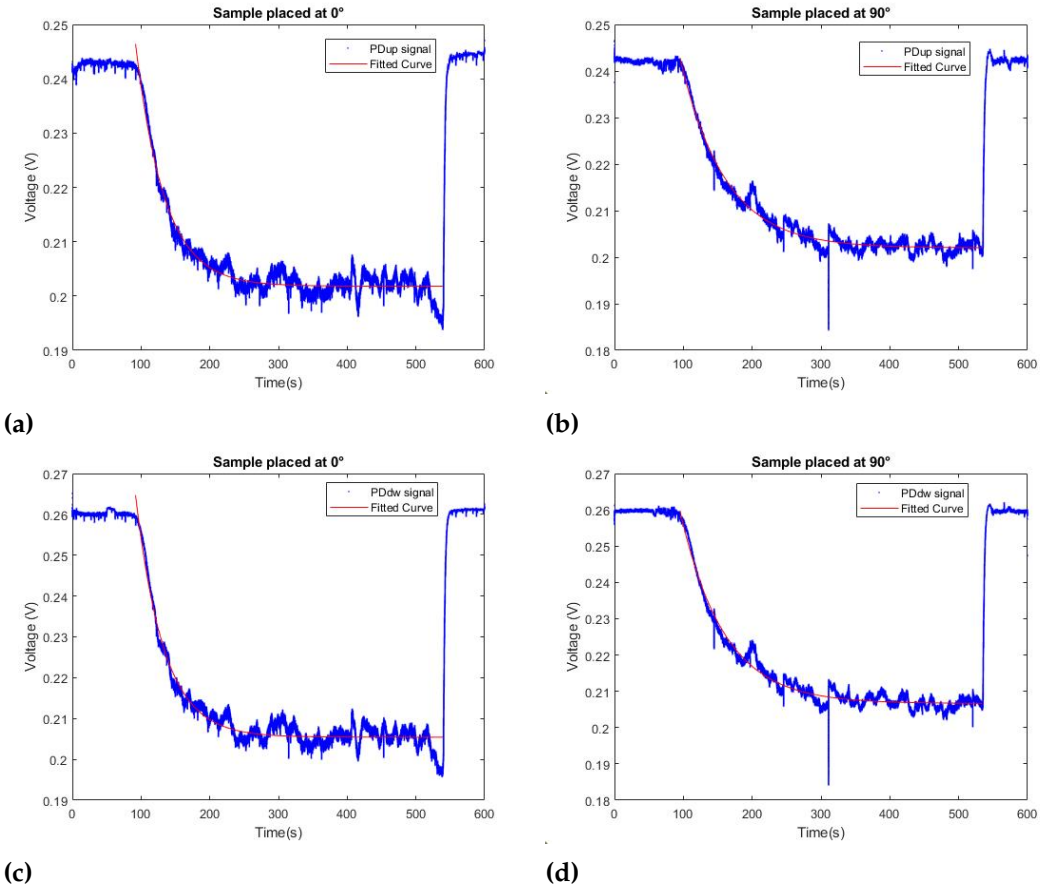

Figure 5.11: Exponential fit of the loading Rb process. **(a)** and **(b)** PDup signal and sample placed at 0° and 90° respectively, **(c)** and **(d)** PDdw signal and sample placed at 0° and 90°.

τ (s)		
	0°	90°
UP	41.49	64.95
DW	40.57	63.58

Table 5.1: Extrapolated values of τ for the two different values of θ and the two acquiring photodiodes.

signal by the channeltron in the two configurations, which corresponds to a drop in the voltage of $\Delta_{max90°=22.87\,mV}$ and $\Delta_{max0°} = 16.24\,mV$. The higher electronic value at 90° is due to the initial higher number of atoms reaching the channeltron due to the scattered atoms by the sample surface.

Another interesting aspect is that after the drop, the orange curve reaches a "plateau", with a value of $\Delta V_{0°} = 10.73\,mV$ at the end of the loading process, named T_{off}. On the other hand the blue line seems to increase during all the measurement, with a value of $\Delta V_{0°} = 7.59\,mV$ at T_{off}. The value of $\Delta V_{0°}$ at T_{off} has been extrapolated

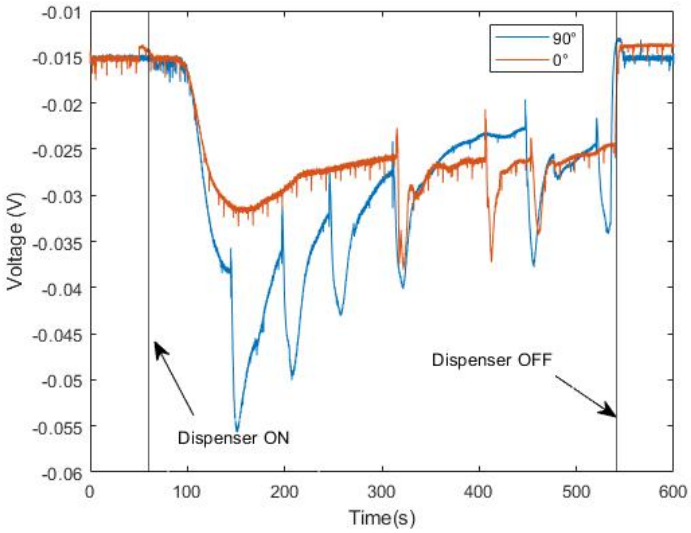

Figure 5.12: Channeltron signal of the loading process. (blue curve) Sample placed at 90°, (orange curve) sample placed at 0°.

by linearly fitting the data between the last two peaks. This reflects the fact that, with an inclination of 90°, the equilibrium condition is reached with longer times, coherently with what seen in fig. 5.11.

In order to verify the presence of the Rb, after 2 hours of loading, a LIAD illumination with a light flash having a strong component in the blue-UV wavelength range was performed , in order to check the release efficiency of Rb atoms in the vacuum from the nanoporous sample. The illumination was made by the upside window. The Rb atom desorption has been detected by scanning the ECDL probe laser at $780nm$. The obtained result are shown in fig. 5.13, where both the beams crossing the chamber are recorded. Again, the labels PDup and PDdw refer to the beam that passes respectively, above and below the sample during the LIAD measurement.

In fig. 5.13 the typical resonance peaks associated to the laser frequency scan are well above the noise in both the PD signals and last for about $0.2s$. This indicates that there is an actual release of Rb in the chamber, but, since during the deposition process, the atoms are also adsorbed by the stainless steel walls, identifying the exact origin of the released atoms may be controversial. In order to overcome this issue, measurements for two different configurations of the sample respect to the probe laser beams have been performed; for example, in the previous figure, the sample was placed with the nanoporous film downwards.

In fig. 5.14, the fits of the two PD curves during the LIAD effect are reported. In this case, to have the precise dynamics of the desorption, the probe laser is tuned at a fixed frequency (on an absorption maximum) and the nanoporous alumina film is faced downwards.

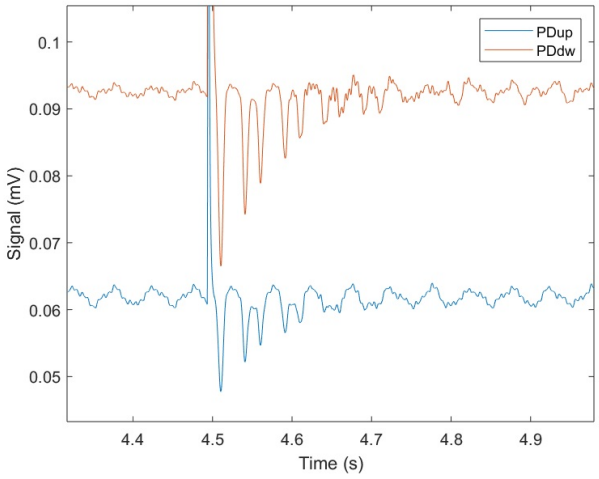

Figure 5.13: LIAD signal seen on both photodiodes where are present the Rb peaks.

If one consider the desorption from the chamber walls uniform and independent on the sample disposition, the laser beam closer to the alumina film should detect more Rb atoms and larger amplitude variation.

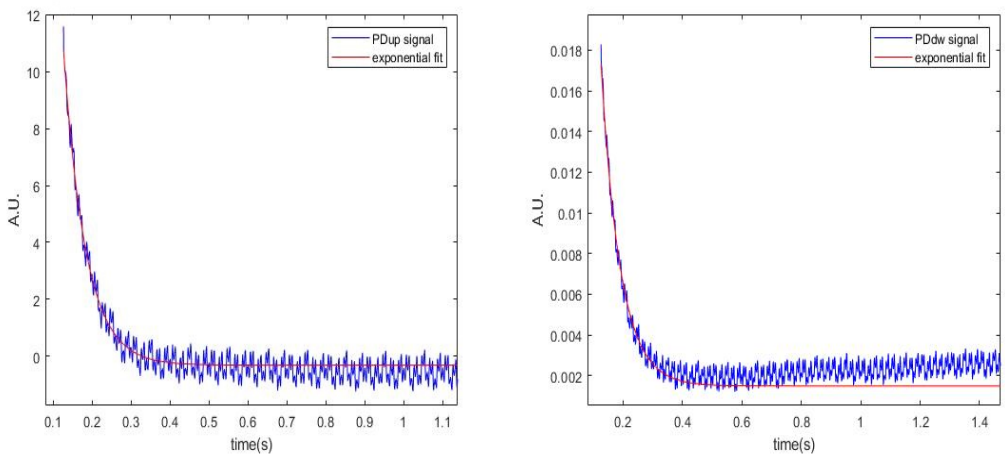

(a) **(b)**

Figure 5.14: (a): exponential fit on the PDup signal. **(b)**: exponential fit on the PDdw signal.

Both the curves have been fitted by a decay exponential function, given by eq. 5.2, in order to obtain 1. the recovery time τ, that is an indication of how long an Rb atom survives in the chamber volume and 2., more important, the variation amplitude. The obtained values of the recovery time are: $\tau_{up} = 56.7 \pm 0.2\ ms$ and $\tau_{dw} = 64.9 \pm 0.2\ ms$. The values of the peak amplitude indicates which beam passes through more Rb atoms. In this case the PDdw signal is expected to result more absorbed and indeed the obtained results are: $A_{up} = 10.7 \pm 0.1\ mV$ and $A_{dw} = 17.1 \pm 0.1\ mV$.

It must be noted that the released atoms come from the most external surface of the porous structure, as for the pore adsorbed atoms, the desorption is mediated by a diffusive process which takes place in a much longer time. Nevertheless from these measurements one can claim that, at least on the most outer part of the film, there is an effective adsorption of Rb atoms.

The most important result of the investigation on porous alumina samples is given by the macroscopic evidence of the formation of Rb nanoparticles induced by the illumination with a laser of wavelength $\lambda = 445\ nm$, at an output power of $1W$ and a laser beam diameter of $< 2.5 \times 5.2\ \text{mm}^2$. The interaction of the blue photons with the porous matrix lasted 30 mins and it was performed just after the Rb loading process, which has lasted $2h$, as usual.

During the exposition to the dispenser Rb beam, the sample was tilted of 90° in such a way to have the nanoporous face towards the Rb dispenser. However, as the sample surface is not orthogonal to the dispenser, the Rb deposition on the sample is not expected to be uniform but growing linearly along the sample diameter.

After the blue illumination on the sample a whitish ellipsoidal spot appeared, as can be seen in fig. 5.15; this spot indicates the possible formation of Rb nanoparticles.

Figure 5.15: Spot on the sample indicating the presence of Rb nanoparticles.

In order to verify this supposition, a diode laser at $\lambda = 852\ nm$ and with a maximum output power of $1.1mW$ has been selected to measure the transmission of quasi resonant light through the sample. In fact, this wavelength does not interact with bare Rb atoms, but it is in the range of the broad peak of oblate and prolate ellipsoidal Rb NPs [20], as shown in fig. 3.8.

In order to have a map of the transmission along the sample diameter, 21 positions, at a 1 mm distance one another, have been tested. Each experimental point has

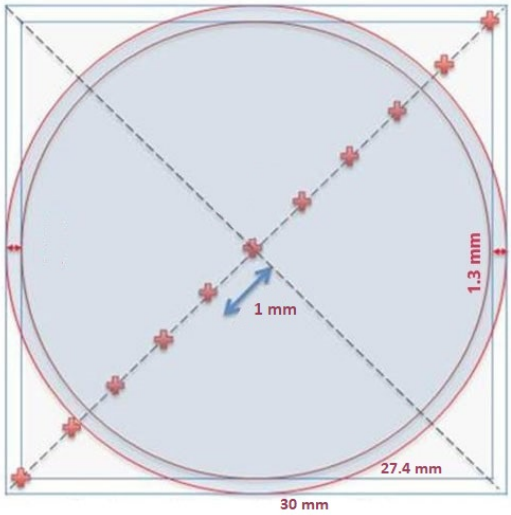

Figure 5.16: Scheme of the points along the sample used to measure the transmission.

been recorded averaging for 10 s. The sample has been shifted by the feedthrough stainless steel translator stage, to whom the sample holder is mechanically fixed. The laser beam has been focused on the sample in order to cover the minimum possible area, for sure, smaller than the spot of the blue laser beam. The sample size and the points used for the light transmission analysis are sketched in fig. 5.16.

In fig. 5.17, the results of the transmission measurements are shown. The values labelling the x-axis refer to the distance along the steel rod: a shorter distance means that the sample is closer to the Rb dispenser and, conversely, the 852 *nm* laser beam crosses an area far away from the dispenser. The amplitude behavior is coherent with what expected, namely a not uniform Rb deposition. Indeed, as can be seen in fig. 5.17a, at points further from the Rb dispenser, the light transmission is higher, i.e. points closer to the dispenser have been better covered by Rb. On the contrary, in correspondence of the spot there is a sudden decrease in the transmission value, due to the interaction between the Rb NPs and the 852*nm* laser beam.

These points have been linearly fitted first, in order to extrapolate the angular coefficient of the straight line, to flatten data and to transform transmission in absorption. The flattened data have been fitted with a Gaussian curve [1]:

$$f(x) = A \cdot e^{(-(\frac{x-b}{c})^2)} + d \tag{5.3}$$

where the Full Width Half Maximum (FWHM) is equal to $2\sqrt{2\ln(2)}\,\sigma = 2\sqrt{\ln(2)}\,c$.

In fig. 5.17b the result of the Gaussian fit is shown. The FWHM is $\simeq 0.15$ cm,

[1] The beam laser has a Gaussian profile, so the spot on the sample is expected to follow a Gaussian profile as well.

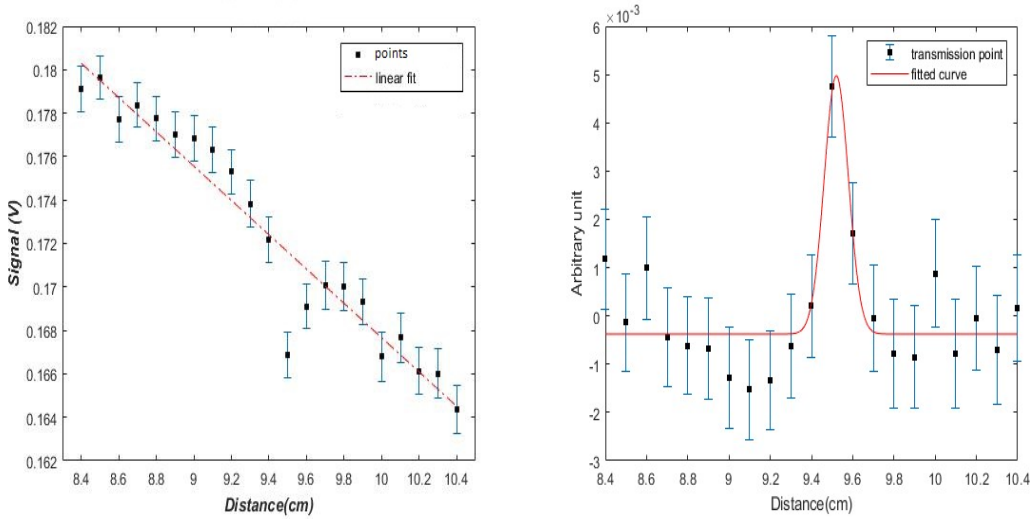

(a) Linear fit of the data transmission **(b)** Gaussian fit

Figure 5.17: (a): Linear fit of the transmission data points. **(b)**: Gaussian fit of the transmission data.

comparable to the short axis of the blue laser beam elliptical spot; the center is positioned at x = 9.5 cm. The percentage variation in transmission is of about the 2%. The detailed MATLAB code used for the acquisition and study of the LIAD dynamics is reported in appendix A.1.

It is worth noting the two negative holes at the edge of the Gaussian profile, which correspond to a local increase of the light transmission. This is due to an emptying effect by the 445*nm* laser which extend for about 0.5*mm* at each side. As already said, the blue laser beam induces a local desorption of the atoms and, in turn, a formation of nanostructures. The formation is favored where the light is more intense; this produces a desorption of the atoms which are located close to the center of the beam spot and a diffusion towards it, for the particular depletion created by the blue laser.

In the next step, after removal from the vacuum chamber, the sample has been analyzed at the spectrophotomer by exploring different zones in order to check the effects of the illumination with the blue laser. In fig. 5.18, four spectra taken in four different points are reported: the measurements are related to the spot position, two side positions outside the spot (named "out1" and "out2"), and a position close to the edge of deposited alumina.

The spectrum of the spot (black line) shows higher values of absorbance for all the wavelength scanned. In particular, taking into account the "edge" line, the absorbances for the peaks at about 320 *nm* and 480 *nm* are the 77% and the 85% respectively of the spot spectrum value.

This difference is the confirmation of the presence of nanoparticles, which behaves as light scattering centers. The fact that no resonance peaks are present is

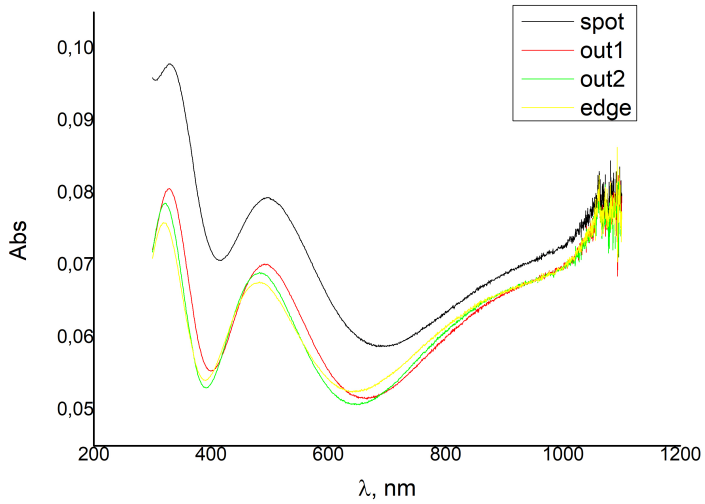

Figure 5.18: Absorbance spectrum taken in different points on the sample: center of the spot *(black line)*, two points close to the spot *(red and green lines)* and on the edge between the substrate and the nanoporous film *(yellow line)*.

probably due to the fact that the size of NPs is randomly distributed, as the pore size in porous alumina is not defined as in the PGs. The removal of part of the nanoporous film by the blue laser can be excluded since as can be seen in fig. 5.10 this kind of phenomenon would cause, passing from the thicker layer to the thinner one, a blue-shifting of the peaks as well as a reduction in number of the same. In the same framework, the $12nm$ black line shift towards longer wavelength can be understood as a difference in the local alumina film thickness.

Finally, the $300nm$ alumina sample has been analyzed at a Scanning Electron Microscopy (SEM). As the images in fig. 2.6, also this picture was taken with an instrument at Dipartimento di Scienze Fisiche , della Terra e dell'Ambiente - sezione di Geologia (courtesy of Giovanna Giorgetti).

This technique allows for an analys of the topology of a surface by means of a focused electron beam with energy in the range of $0.2\ keV$ up to $40\ keV$. In the most common SEM mode, the secondary electrons (which have an energy $< 50\ eV$) produced by inelastic scattering interactions between the electron beam and and the substrate and ejected from conduction or valence bands of the specimen atoms, are detected. The number of the secondary electrons detected depends on the specimen topography. Given their low energy, these electrons are emitted from within a few nanometers from the sample surface. They are then unable to provide information about the most internal structure of the sample.

For usual SEM imaging, the sample surface must be conductive. Nonconductive specimens collect charge when scanned by the electron beam, causing in turn

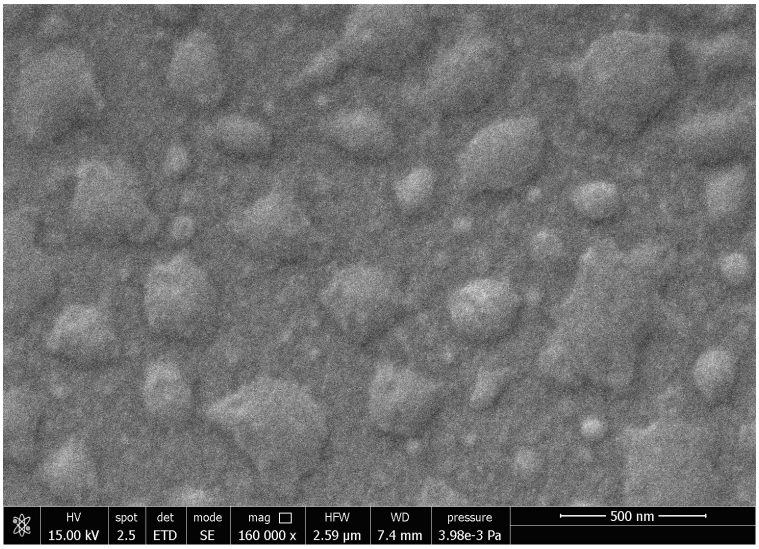

Figure 5.19: SEM image of the 300 *nm* alumina sample after the Rb deposition process.

image artifacts and scanning faults. In order to analyze nonconductive surface, the sample must be coated with an ultrathin film of conductive material.

In fig. 5.19 a SEM image of the 300 *nm* alumina sample with a scale bar of 500 *nm* is shown. In this picture there is a clear evidence of a formation of islands of the order of hundreds of nanometer, much larger than the predicted average pore size. The formation of isolated cluster, instead of a uniform layer, is consistent with the high roughness of the surface. Roughness and defects goes against the growing of a uniform layer of the adsorbed specimen. Unfortunately, given the characteristic of the SEM, it is impossible to put in evidence the internal pore coverage of the sample.

5.2.2 100 nm

In this section the results of the study of the nanoporous 100*nm* thickness alumina sample are reported. The performed measurements have been taken in strict analogy with what has been presented in sec. 5.2.1. We can immediately point out that, due to the thinner layer and the smaller available volume, we have not observed the same behavior, and no evidence of NPs formation has been detected.

After 1 hour of Rb deposition with a dispenser current of $I = 5$ A, we have tried to induce a pulsed LIAD effect by the flash light. In fig. 5.20, the corresponding channeltron signal is shown. The optical signal was simultaneously acquired by the PDs but it did not reveal any presence of desorbed Rb atoms.

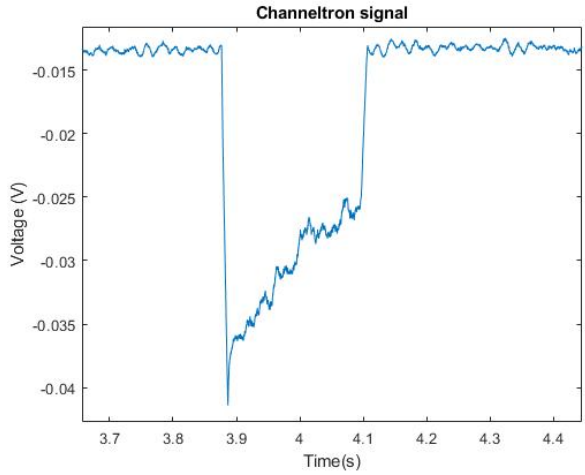

Figure 5.20: Channeltron signal during LIAD flash.

The typical channeltron peak actually reveals the presence of some ions, as highlighted by the slow dynamics towards the nominal zero value of the channeltron voltage. The peak presents a total 210*ms* activation time, much longer than the flash duration. This observation shuold suggest an ejection from the sample, not from the cell walls, of some impurities in the porous alumina. Because of the lack of Rb in the signal, the rest of the data have been acquired after a 2 hours exposition time to the Rb dispenser beam.

The next figures report on the results of an illumination with the 445*nm* laser at a power of 500*mW*, lasting 3.00*ks*; the illumination starts at $t_{on} = 600$ s and it ends at $t_{off} = 1800$ s, as indicated in the plots by the black vertical lines.

The fig. 5.21a shows a small peak when the blue laser has been switched on and a slow rise to the zero value, which however happens before the end of the illumination. This can be due to the fast emptying of the small porous lighted volume.

The fig. 5.21b signal has been obtained by operating a subtraction of signals referred to the transmitted beam (passing close to the sample) and an external (path in air) reference beam. then fitting the signal with a linear function to extrapolate the slope of the line. This procedure has been introduced in order to eliminate the eventual frequency drift in the laser wavelength. Two peaks are present after t_{on} and t_{off} as well as other oscillations during the illumination. It is, however, hard to say if these oscillations in the absorbance are due to release of Rb atoms or to the formation of nanoparticles.

The next measurement, reported in fig. 5.22, was performed with the sample tilted at 45° in order that the blue laser and the probe 780*nm* laser have spatial overlapping in the same zone on the sample. In this case the illumination last for 2700 s and starts at $t_{on} = 300$ s and ends at $t_{off} = 3000$ s at an incoming power of about 900*mW*. Again, the plot was obtained by the subtraction procedure.

The signal was then fitted with eq. 5.1 and it presents the same rise as the one

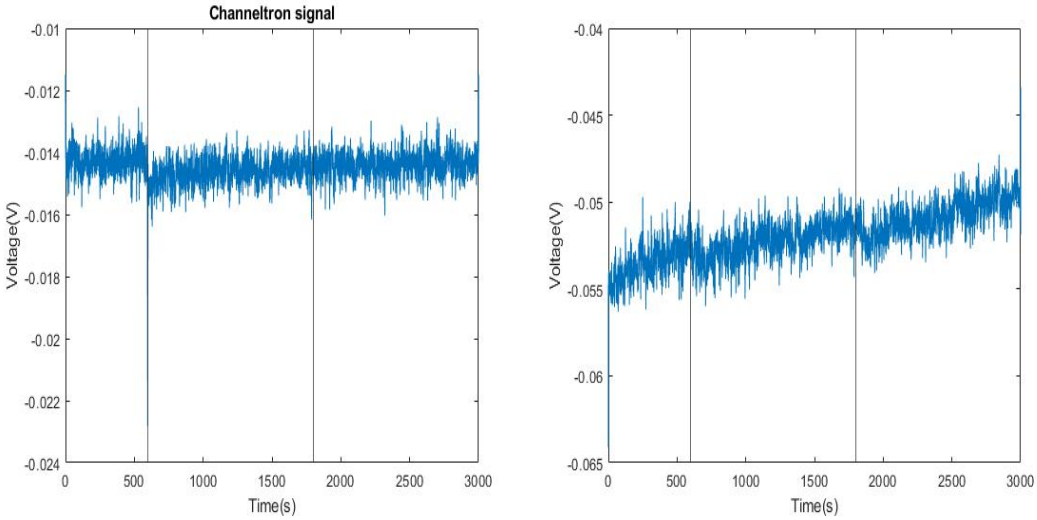

(a) **(b)**

Figure 5.21: Illumination of 1200 s with 445 nm laser. Vertical lines indicate the start and the end of the illumination. **(a)**: Channeltron signal. **(b)**: PDs difference signal.

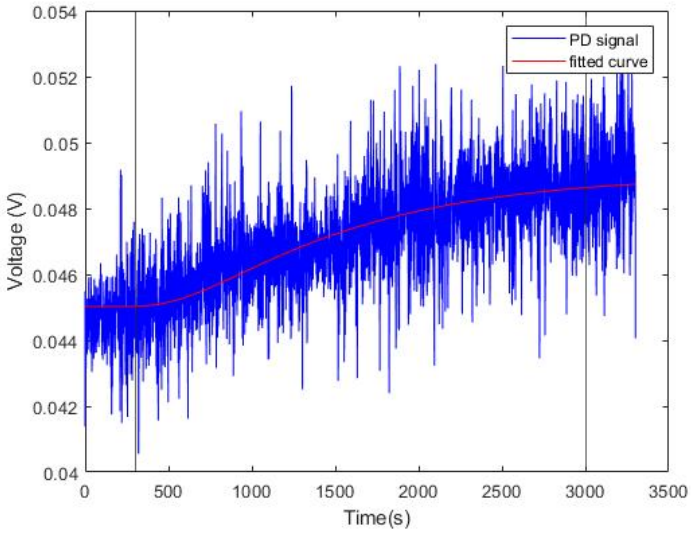

Figure 5.22: Signal obtained during an illumination of 2700 s.

seen on the Vycor sample. With so much laser intensity, some diffusion seems to be promoted, but the release of Rb atoms from the porous structures is strongly contrasted by some internal competition mechanism. Despite the long illumination time and the high power of the laser, there was no spot formation: no Rb nanoparticle has been built, at least in the sensitivity limit of the setup. Spectrophotometer measurements ware not performed on this sample due to the higher and faster oxidation of the thinner layer.

To conclude, despite the evidence of a presence of Rb atoms both deposited on

the porous surface and included in the inner volume, the thickness of the sample seems to inhibit the formation of an adequate effective pore network.

5.3 Porous glass in alkali vapor cells

The main advantage of using a vapor Pyrex cell, is the relatively easier loading process of the porous glass. The cells contain an alkali reservoir which can be heated to increase the vapor pressure, if needed. We have studied the behavior of two PG samples lodged in cells with Rb and Na respectively. The vapor pressure at room temperature $T_{room} = 325$ K for the two alkali species is $P_{Rb} = 5.54 \cdot 10^{-4}$ *Pa* and $P_{Na} = 1.046 \cdot 10^{-7}$ *Pa* [186]. By making use of the ideal gas law one can easily extimate the atomic density of a cell with a reservoir at the equilibrium, which results for the Na atoms:

$$\rho_{Na} = \frac{P_{Na} \cdot N_a}{RT} = 2.3 \cdot 10^7 \frac{atoms}{cm^3} \tag{5.4}$$

From resonant absorption technique, the measured density of Rb at equilibrium results $1.6 \times 10^9 \text{atoms/cm}^3$, smaller than the thermodynamical value by a factor 3. This is a proof that the presence of a porous surface in the cell strongly affects the interplay between the alkali reservoir and the cell volume, given the larger free space available for atoms inside the PG [20]. Note that the two density values differ by two orders of magnitude. In order to overcome this issue, the Na cell has been heated in a home made chalk oven which provides a temperature gradient between the alkali reservoir and the nanoporous surface.

In fig. 5.23 are shown the pictures of the two cells, placed on the home made support, containing Na and Rb vapors, respectively in 5.23a and in in 5.23b.

The two porous glasses differ for size and porosity features. The Na glass has a volume of 14mm $\times$ 13mm $\times$ 1mm, an average pore diameter of 20*nm* and a declared porosity of 55%; the Rb PG has 30mm $\times$ 15mm $\times$ 1mm size, 95% of the total pore number with a 17*nm* diameter, and a 53% free volume, a 50m^2 internal surface. The two cylindrical cells are also slightly different in length and diameter, respectively 8.2 cm, 2.5 cm for the Na one, and 7.4 cm and 3.5 cm for the Rb one.

The light sources employed to illuminate the PGs and induce the formation of NPs are the ones described at the end of section 4.1.1, namely the *Manual Tunable Littman-Lion System Infra-red laser*, *DLX 110 TOPTICA High-Power Tunable* and the *High pressure Hg vapor lamp*.

Later, we have analyzed the absorbance spectrum at the spectrophotometer, in order to see the eventual formation of NPs. The negative values of absorbance in the plot depend on how the zero of the sample was fixed; more in detail, the spectra

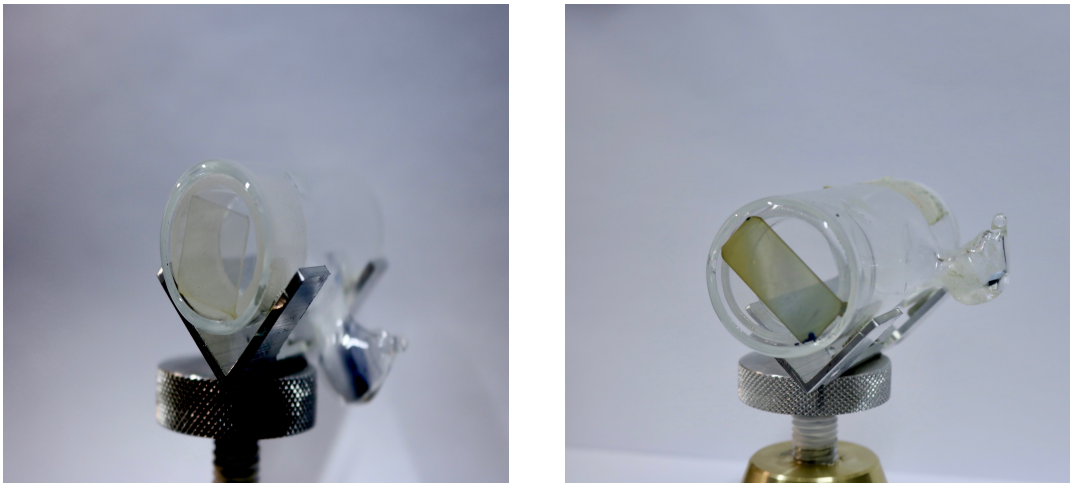

(a) **(b)**

Figure 5.23: Pictures of the sealed cells containing a nanoporous glass sample. **(a)** Cell containing Na; **(b)** Cell containing Rb

in par. 5.3.1 are calculated by subtraction of the baseline of the cell (taken before illumination) and the following measurements.

5.3.1 Na cell

The first step consists in the loading process of PG by the vapor phase atoms. Heating the cell revealed to be a crucial factor in the loading process. In the case of Na, the expected size of NPs is of the order of a few nm, in agreement with the pore diameter, in such a way that the absorbance peak maximum should be centered around 450*nm* [187].

In fig. 5.24 the absorbance spectrum in the range 300 *nm* - 1100 *nm* is reported: the illumination time with the 532 *nm* laser source at an intensity of 50 mW/cm^2 is 30 min. In the plot a 0.1 % decrease in the absorbance values around 500 *nm* is present. The rest of the spectrum presents a flat trend without any other structure. It must be taken into account the quite low atomic vapor pressure which does not favor the adsorption of the atoms on the pore surface. Unfortunately, the Na reservoir appears empty at naked eyes: the distillation of sodium was partially unsuccessful and the whole Na drop evaporated without being able to let the vapor density achieve the level usually associated to the explored temperature range.

The following spectrum has been acquired after an heating process of 4 hours. The temperature, measured with a thermocouple, was fixed at $T \simeq 190°C$ on the alkali reservoir and at $T \simeq 60°C$ on the NP glass side. The illumination has proceeded

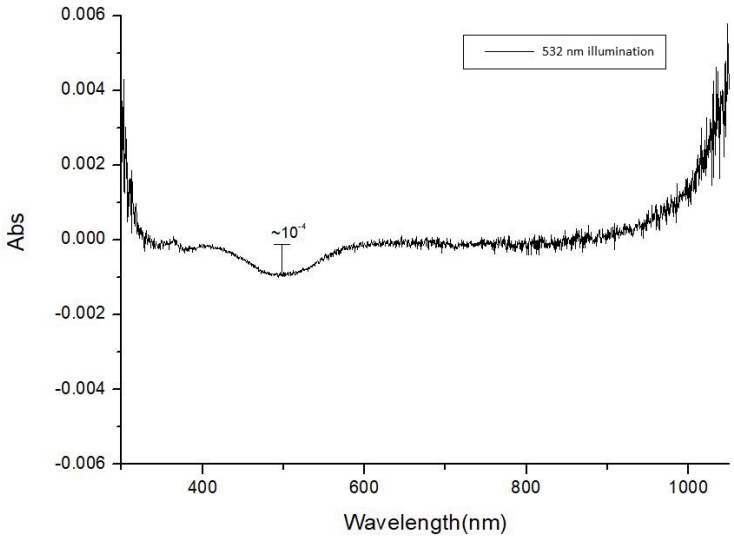

Figure 5.24: Absorbance spectrum after an illumination of 30 min with the 532 nm laser.

as previously described.

In this case the peak at 500*nm* increase of a factor 10; in fact, the percentage decrease is of 1%. This indicates the effectiveness of the heating in the adsorption on the pore surface. Nevertheless, considering the low atomic pressure, the absorbance peaks are not present.

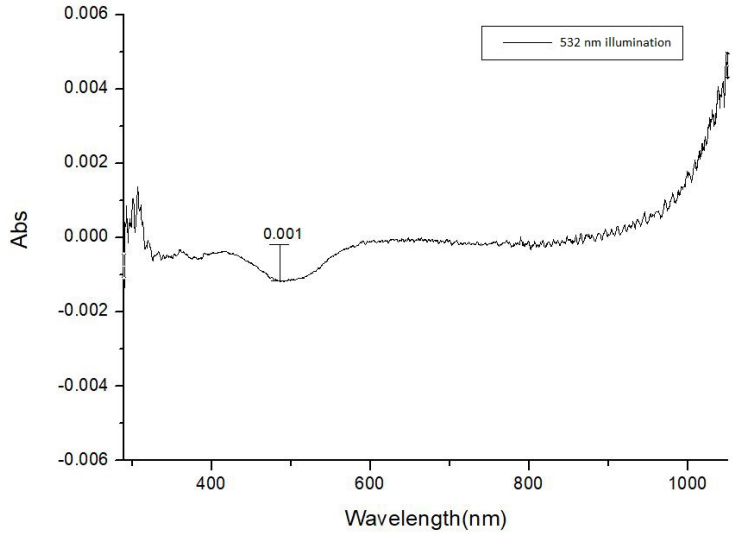

Figure 5.25: Absorbance spectrum after 4 hours of heating and an illumination of 30 min with the 532 nm laser.

As the 532*nm* wavelength is particularly efficient in the atomic desorption and it is also close to the plasmonic resonance, it favors the SPID effect instead of nanoparticle aggregation: this is a reasonable explanation of the decrease in the absorbance

spectrum.

For the same goal, the Hg lamp has been selected as a desorbing light source; in fact, its emission range falls enough far away from the predicted Na plasmonic resonance in such a way to only favor the aggregation of the adsorbed atoms into nanoparticles. In fig. 5.26 the spectrum after 3 hours of heating and two illuminations is reported: the first 30*min* duration lightning has taken profit of the green laser, later on the Hg lamp has been applied for 30*min*. The lamp intensity was 300mW/cm^2, covering a surface of 1 cm^2.

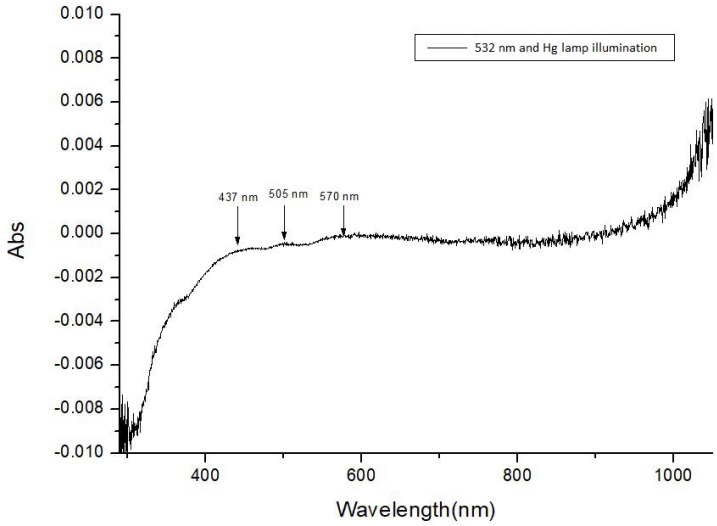

Figure 5.26: Absorbance spectrum after 3 hours of heating, a 30 min illumination of both the 532 *nm* laser and the high pressure Hg lamp, in sequence.

As can be seen in fig. 5.26, the main effect of the Hg lamp is the removal of the the emptying effect due to the illumination with the 532 *nm* laser source and the consequent formation of three peaks centered at 437 *nm*, 505 *nm* and 570 *nm*. The second wavelength value is in agreement with what observed in [174], which predicts an average particle size of 12 *nm*.

There are two interesting features to be underlined:

1. the growth in the IR part of the spectrum which can be associated with the formation of micrometric size particles.
2. the absorbance decrease in the UV zone in a similar way as the previously observed 500*nm* peak. This is a "cleaning" effect on the pores from Na, due to the main wavelengths emitted by the Hg lamp, which are indeed between 300 *nm* and 450 *nm*.

In principle, the growth in the IR part of the spectrum could be contrasted/prevented by an illumination with a light source emitting in the same IR range.

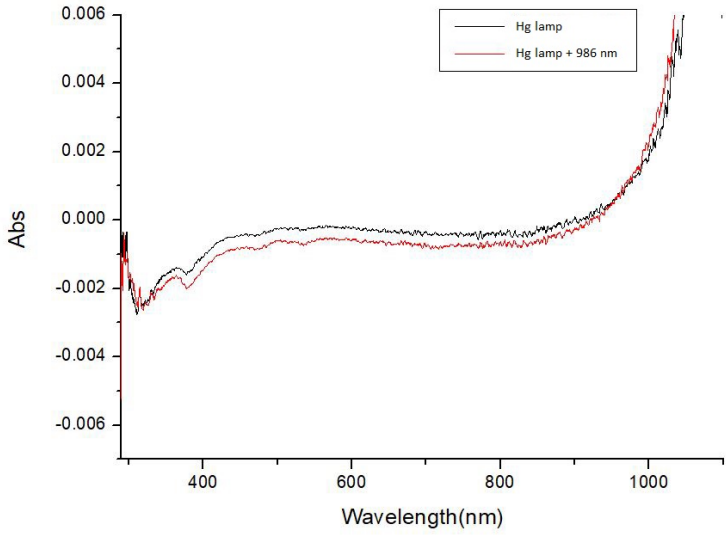

Figure 5.27: Absorbance spectrum after 6 hours of heating. *(black line)* 30 min with Hg lamp, *(red line)* 30 min with Hg lamp + 5 min with 986 nm laser.

Having this idea in mind, the next experiment has been prepared with the following steps: an heating process of 6 hours. an illumination of 45 min with the Hg lamp, a further 5 min illumination by the 986 *nm* laser at 30mW/cm^2 intensity. The results are shown in fig. 5.27.

The IR illumination does not change the spectral response of the sample. There are again both the peaks in UV-visible part of the spectrum, as induced by the Hg lamp illumination and the IR growth starting at about 900 *nm*. The effect of the 986 *nm* laser is a general downward shift of the spectrum, i.e. the sample has become more transparent and the NP formation caused by the UV has been reduced.

As a final investigation, in order to have a more complete picture of the cell response to an external stimulus in a range not yet explored, a high intensity 780 *nm* laser (800 mW/cm^2) has been introduced, applying the same strategy for the preparation of the sample and the execution of the measurements. Two types of illumination have been applied: A) the 780 *nm* source alone (15 min of application), B) Hg lamp (45 min) plus 780 *nm* laser (15 min). In fig. 5.28, the experimental data are reported.

The result is comparable with what has been found in the case of the 986 *nm* laser excitation.

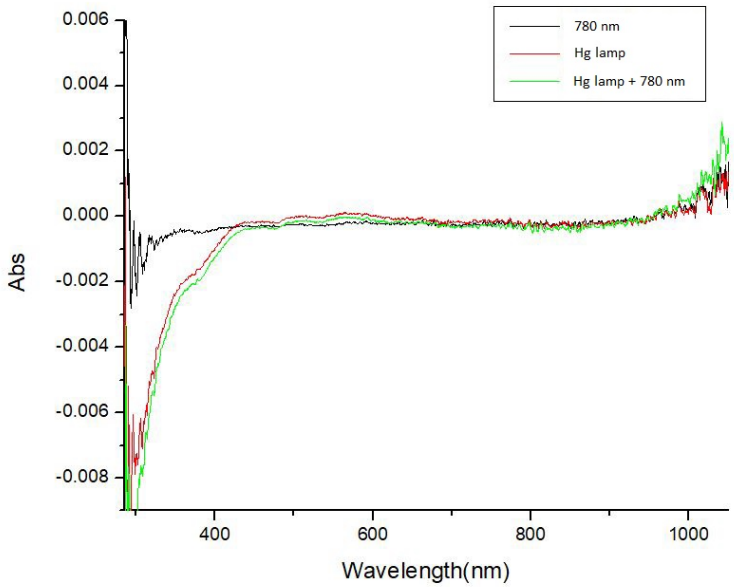

Figure 5.28: Absorbance spectrum after 6 hours of heating. *(black line)* 15 min with 780 nm laser, *(red line)* 45 min with Hg lamp, *(green line)* 45 min with Hg lamp + 15 min with 780 nm.

5.3.2 Rb cell

It has been clearly proved that a near-IR wavelength destroys the Rb nanostructures formed by an external illumination [30]. The Rb nanoporous sample, which has an average pore size of 17 *nm*, was illuminated only by the Hg lamp beam with an intensity of 300 mW/cm^2 and with the IR 986 *nm* laser wavelength with an intensity of 30 mW/cm^2. The cell was not heated since the Rb atomic vapor density is two orders of magnitude larger than the Na vapor density as said earlier. In fig. 5.29 are reported three absorbance spectrum: the black line was taken without any illumination, the red line after 10″ illumination with the Hg lamp and the green line after 5 min illumination with the 986 nm laser.

As can be seen by the black line in fig. 5.29, NPs are already present in the pore matrix without the needing of any illumination, referring to prolate and oblate spheroid, respectively with a resonance wavelength of $\lambda_{LSP} = 899\ nm$ and $\lambda_{LSP} = 751\ nm$ as described by the Gans model in sec. 3.5. This is a consequence of the larger vapor density and the consequently efficient loading. Also, these spectrum peaks, coincide with the one showed in fig. 3.8, where the sample was irradiated with a green light at 532 nm for 10 min and with an intensity of 30mW/cm^2. In that case, considering the longer exposure time and the larger desorption efficiency given by the wavelength of the light source, the resonance peaks have a larger amplitude an a less growth of the absorbance in the visible-UV part of the spectrum .

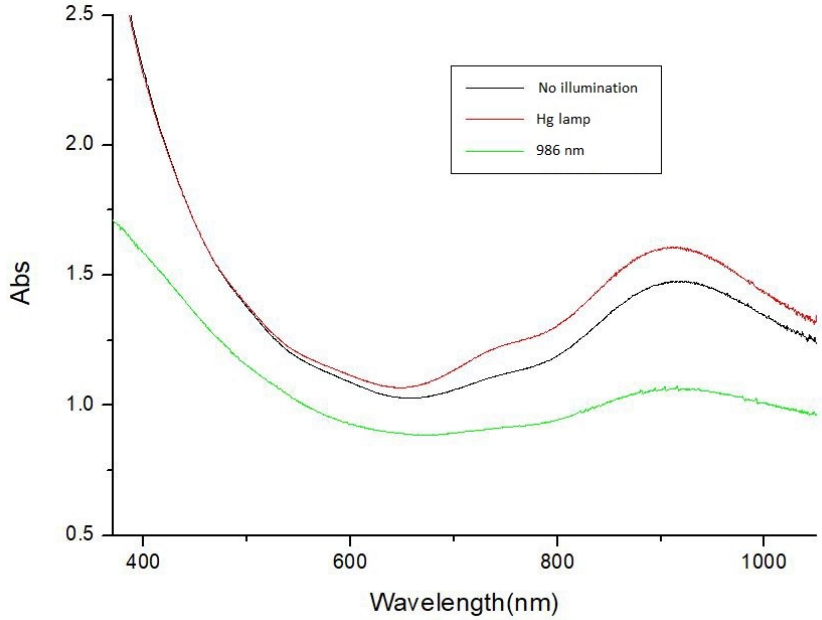

Figure 5.29: Absorbance spectrum. *(black line)* Spectrum acquired without illumination, *(red line)* illumination of 10 s with Hg lamp, *(green line)* illumination of 5 min with 986 nm.

There are different mechanisms involved in the process of nanoparticle formation:

1. the efficient desorption of alkali atoms adsorbed on the porous structure which has an high surface density.
2. the modification of atoms diffusion parameters induced by the light.
3. the environment in which the atoms are confined which provides a large available volume and hence a possibly very high atomic vapor density.
4. the presence of nucleation center where alkali atoms can accumulate to start the formation of aggregates. Nucleation centers can be both defects of pores structures or defects in the deposited atomic layer.

The size of the aggregated particles depends mainly on the pore size. In this case, the statistical favored length scale is about 3 nm, with an axial ratio of 1.25 for an oblate and 0.8 for a prolate. It is hard to identify in our kind of investigation the separated contribution given by each mechanism: nevertheless it is possible to conclude that the third point gives the most relevant consequence, In fact, such macroscopic effects are present only in nanoporous materials.

Gans theory of light-matter interaction with metal ellipsoidal nano-particles explains the observed spectrum predicting a shifting of the atomic lines, depending on the shape and size of the aggregates, due to the collective behaviour of the outer

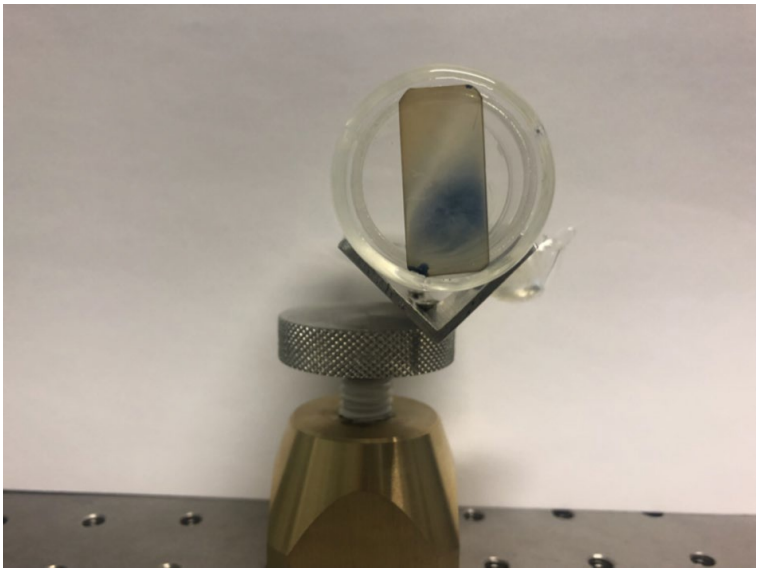

Figure 5.30: Picture of the nanoporous glass sample in the Rb cell after 10 *min* illumination of 532 *nm* laser source.

electronic shell in alkali atoms, namely the surface plasmon resonances. This means that an incident photon, resonant with a plasmonic band, is able to destroy the metal aggregates by excitation.

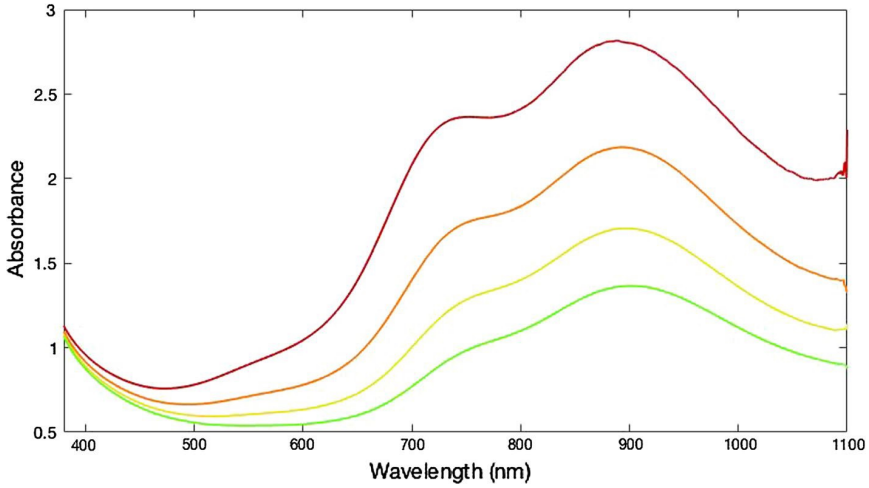

Figure 5.31: Absorbance spectra taken during the relaxation process. The sample was first illuminated for 10 min with the 532 nm laser source. Each lines has been taken at time interval of 45 min [20].

The effect of the Hg lamp, with only 10″ of exposition, is to further increase the formation of particles and then the amplitude of the resonance peaks in the IR part, while maintaining the same response at shorter wavelength.

The 986*nm* laser has two effects. First, it is able to destroy the NPs formed in the pores, being close to the resonant wavelength of 899*nm*, removing then the two peaks appeared in the other spectra. Second, it reduces the absorbance value of the

sample, hence making it more transparent. This may be due to the fact that, together with the destruction of the aggregates, there is also an emptying effect of the pores.

In fig. 5.30 is shown a picture of the PG sample taken immediately after 10 *min* illumination of 532 *nm* laser beam. It shows the macroscopic effect of the desorbing laser beam on the illuminated area.

However, as shown in fig. 5.31, without any desorbing illumination, NPs density decreases, tending to return to the condition before the illumination. The spectra in fig. 5.31 are taken after the 532 nm laser beam exposition with intervals of 45 min each one, starting from red line up to the green one.

This is an evidence that the NP is not a stable system: there is a dynamical equilibrium between Rb pore vapor density, Rb surface density, NPs density and Rb cell vapor density, as provided by the reservoir. Since the Rb reservoir contains a massive alkali drop (properly distilled), an infinite quantity of atoms released on time in vapor phase becomes available to enter the pore structure. The equilibrium condition keeps changing in time.

It was demonstrated [113] that the nanoparticles growing process corresponds to a change in the population ratio between oblate and prolate particles shape. To conclude, mainly because of the greater vapor density, the Rb sample revealed to be more efficient, as well in the adsorption and desorption process, both in the formation of NPs.

Chapter 6

Conclusion and Outlook

In this final chapter the main results of the Ph.D.work described in this thesis are collected (6.1). Special attention is given to the experimental data obtained on the nanoporous alumina. In sec. 6.2, a possible perspective for the future development on the research is provided.

6.1 Conclusion

In this work, optical and electronic techniques for the detection of the light induced desorption mechanisms of rubidium adsorbed onto various porous samples have been applied. It has been found that, by using porous glass surfaces with different average pore sizes and a proper frequency and intensity level of desorbing light, it was possible to exploit the LIAD to both load at detectable density values PG samples and enhance the formation of Rb aggregates in the nanostructured materials.

In particular, the formation of Rb nanoparticles in a nanoporous alumina $300nm$ thick film deposited on a sapphire substrate was demonstrated for the first time, in the difficult condition determined by a UHV environment. The sample has been prepared by a several hours commercial Rb dispenser loading and by a $\sim 1/2h$ $1.0W$ blue laser illumination. The final effect can be appreciated at naked eyes, as a spot of the beam waist size traced on the sample. It has been proved that the spot corresponds to a lower transparency both by a $852nm$ probe beam transmission measurement and by a spectrophotometer check.

As a second relevant result, the data collected with the Vycor 7930 Porous Glass in UHV have shown a relevant adsorption of Rb atoms deeply implanted in the sample. This was demonstrated when the desorption was induced by the 445*nm* laser beam, provoking a continuous emission of atoms according to a dynamical regime well fitted by the function $f(t) = \frac{a}{\sqrt{t}} \cdot e^{-b/t} + c$. This is a footprint of a migration of the atoms in the 4*nm* diameter pores, enhanced by the light. The high value of the diffusion time to the free fly in UHV indicates a long random walk into the Vycor volume available, without measurable contributions by surface adatoms. The channeltron counter part evidences the importance of the desorption of other species stored in the sample. The blue light becomes a cleaning tool from a significant fraction of the impurities previously accuulated in open air.

The 200 nm porous glass, because of its opacity, resulted the most difficult sample to perform measurement on. The optical measurements were performed by acquiring the reflected laser beam and according to them it is difficult to assert an actual adsorption and release of Rb atoms from the pores structure. Most probably the Rb atoms only deposited on the more external surface without penetrate in the structure. It is unknown if this depends on the size or porous structure, or on the sample quality.

Only the channeltron signal revealed a release of atoms from the sample, but since this device it can not distinguish between atomic species it may also indicates that the atoms incoming into the channeltron are not Rb atoms. In both the porous glass sample no nanoparticles formation has been observed.

A paper dedicated to the results obtained on the Vycor 7930 Porouos Glass is currently in preparation, as well as another one dedicated to the spectrophotometer analysis of the porous glasses enclosed in the alkali vapor cells.

The two alumina sample investigated have the same structural characteristic except for the thickness: 100 nm one and 300 nm the other. For what concerns the first sample, the channeltron signal revealed the desorption of some atoms by the surface, however the optical measurements did not reveal the presence of rubidium atoms on the surface. This was probably due to alumina layer which is not enough thick and hence has less volume available for the Rb to being adsorbed. Also it was not seen any nanoparticles formation. Nevertheless, an illumination of 2700 s with the 780 nm laser source, caused a decrease in the transmitted signal, suggesting than the presence of Rb onto the surface. However that quantity may be not enough for the formation of nanoparticles.

Next transmission measurements have been performed along the sample diameter with a 852 nm laser beam, which suggests the effective formation of aggregates on the sample.

X-Ray diffraction measurements have been performed, at *Dipartimento di Scienze*

della Terra of University of Pisa, on the 300 nm alumina sample, after the Rb deposition process. Those measurements showed that the presence of the nanoporous film does not affect the diffraction pattern of the crystal structure of α-Al_2O_3 substrate. Nanoparticles of Rb are also not revealed with this analysis. It must be noted, however, that Rb NPs quickly oxidize in air, then their presence in pores structures can be hardly revealed after the removal of tha sample from the UHV chamber.

Two porous glass enclosed in alkali vapor filled cell have been analyzed by using a spectrophotometer. One contains Na vapor and porous surface with an average pores size of 17 nm and porosity of 55% and the other is filled with Rb atoms and there is a porous glass with 20 nm pores size, comparable then with the previously described alumina samples, and a porosity of 53%.

It has been acquired absorbance spectra in range of 300 nm to 1100 nm, after illumination of different time (from 10 seconds up to 30 min) with a 532 nm laser source and a Hg lamp, which has a predominant component of UV-visible wavelength component. To favor the adsorption process the aklali reservoir was heated in an oven while the porous glass was kept at a lower temperature.

The acquired spectra revaled the formation of nanoparticles in particular in the Rb filled cell, probably due to the fact that the atomic vapor pressure is about 3 order of magnitude larger than the pressure in the Na cells. An illumination of 10 s with the Hg lamp was sufficient to induce the formation of Rb aggregate in the porous glass.

As a general comment it needs to be stressed out that the interest in the study of the nanoporous alumina mainly lies in the fact that, despite its chemical and electrical properties are well known, the light interaction properties and the possibility of nanoparticles growing on its surface are little studied and that is the reason behind the interest in this material. In addition, it is worth to say that the EBPVD is not commercially used to produce randomly oriented porous alumina, indeed the samples used in this work were provided by the researchers of the Saint Petersburg National Research University of Information technologies, Mechanics and Optics (ITMO).

To summarize, the most promising results have been obtained on the thicker sample of nanoporous alumina. This suggests that a minimum thickness is required to have a enough volume for the atoms to be adsorbed. Alumina substrate demonstrated to be a proper surface for the Rb atoms to adhere on it, and an illuination with a proper wavelength, can induce the formation of nanoparticles. Beside this aimed to be a preliminary study for the adsorption/desorption proces in the UHV regime, this work showed optimistic and promising result for the continuation of research. Also the observation on the vapor filled cell revealed the formation of nanoparticles, in particular in the Rb cell and with an illumination with the Hg lamp.

6.2 Outlook

In this section some scenarios for further developments of the current research are proposed .

The most challenging goal in the experimental work was revealed the loading process in the UHV environment. The small solid angle covered by the sample as well as the atom losses, reduce the adsorption of Rb atoms onto the surface. One way to overcome this problem can be to create a thermal gradient, cooling down the sample, as it was achieved for the PGs in the vapor cells, in order to promote the physiadsorption of the atoms onto the surface. Another way to optimize the same process can be to focus the Rb emission using an effusive source in place of the Rb dispenser.

Study the alumina in vapor filled cell, hence having a constant flux of atoms onto the surface, may help the understanding of adsorption/desorption as well as the nanoparticles formation. Moving the sample from the UHV chamber to the spectrophotometer is also a dangerous procedure, since the Rb atoms oxidizes as soon as they come in contact with the air. To build a complete and self consistent setup a part of which can be moved to the spectrophotomer without removing the sample from the vacuum could be designed. For example, one can think of a two chamber apparatus, where one chamber is kept at UHV regime and the other, used for the first manipulation of the sample, can be removed and kept at a lower quality vacuum value.

Furthermore, it would be interesting to study the same process with other alkalis, such K or Cs, and check if the interaction between the alumina substrate and the alkali atoms are favored with respect to Rb atoms.

It has been recently demonstrated the formation of micro structures starting from a layer of Rb od Cs on sapphire and nano porous glass surface, with pores size between 7 nm and 17 nm [188, 189], by means of a non-diffracting beam, in particular a Bessel beam. The wavelength used for the structure formation was 532 nm and a light intensity from $450\,mW/cm^2$ up to $4.5\,W/cm^2$. The conversion of a Gaussian beam into a non-diffractive Bessel-like beam can be made by the use of an axicon, a special kind of lens which has a conical surface.

A Bessel beam can be written in cylindrical coordinate as:

$$E(r,\phi,z) = A_0 e^{ik_z z} J_n(k_r r) e^{\pm in\phi} \tag{6.1}$$

where J_n is the n^{th} order Bessel function, k_z and k_r are the longitudinal and radial wavectors respectively, so that $k = \sqrt{k_z^2 + k_r^2} = \frac{2\pi}{\lambda}$, with λ wavelength of the electromagnetic radiation that generates the Bessel beam. and r, z and ϕ the radial, longitudinal and azimuthal component respectively.

These works demonstrated an efficient and easy way to shape and control the aggregation of atoms onto a pores structure. That is why it would be interesting extending this work to the nanoporous alumina and in particular performing that in the UHV chamber. Different alkali species and different wavelength laser source may be used as well.

Appendix A

Matlab code

In this appendix is reported the code used for the signals acquisition and the gaussian fit of the transmission signal showed in fig. 5.17b regarding the spot on the 300 nm sample of alumina.

A.1 Gaussian Fit Code

```
clear
close all

n=dir('*.mat');
x=8.4:0.1:10.4;
X=size(x);
err=zeros(X);
T=zeros(X);

for i=84:104
    filename=sprintf('trasmissione_campione_852nm_%dmm.mat',
        i);
    load(filename);
    i=i-83;
    PDup_s=smooth(PDup,100);
```

```
15      time0=time;
16      clear PDdw Rif rate dims duration dt Np ans X
17      S=std(PDup);
18      FWHM=2.355*S;
19      t=mean(PDup);
20      err(i)=FWHM;
21      T(i)=t;
22  end
23  clear j i m M FWHM time
24  figure;
25  errorbar(x,T,err,'s', 'MarkerSize',4,'MarkerEdgeColor','red',
        'MarkerFaceColor','red')
26  title('Transmission');
27  xlabel('Distance(cm)','FontWeight','bold','FontAngle','Italic
        ');
28  ylabel('Signal (V)','FontWeight','bold','FontAngle','Italic')
        ;
29  legend('signal not smoothed');
30
31  figure;
32  errorbar(x,T,err,'s', 'MarkerSize',4,'MarkerEdgeColor','red',
        'MarkerFaceColor','red')
33  P=polyfit(x,T,1);
34  yfit=P(1)*x+P(2);
35  hold on
36  plot(x,yfit,'r-.');
37  T_flat=T;
38  T_flat=T_flat-x*P(1);
39  title('Transmission');
40  xlabel('Distance(cm)','FontWeight','bold','FontAngle','Italic
        ');
41  ylabel('Signal (V)','FontWeight','bold','FontAngle','Italic')
        ;
42  legend({'transmission','linear fit'})
43  figure
44  scatter(x,-T_flat,'s','MarkerEdgeColor','blue','
        MarkerFaceColor','blue');
45  [ymin,xmin]=min(T_flat(1:end));
46  avg=mean(T_flat);
47  variation=((ymin/avg)*100)-100;
```

```
48 %% Fit: 'Gauss fit'.
49 Y=-T_flat+mean(T_flat);
50 [xData, yData] = prepareCurveData( x, Y );
51 % Set up fittype and options.
52 ft = fittype( 'a*exp(-((x-b)/c)^2)+d', 'independent', 'x', '
       dependent', 'y' );
53 opts = fitoptions( 'Method', 'NonlinearLeastSquares' );
54 opts.Display = 'Off';
55 opts.Lower = [-Inf -Inf 0];
56 opts.StartPoint = [0.004735181593712 9.5 0.27692298496089
       -0.004];
57 % Fit model to data.
58 [fitresult, gof] = fit( xData, yData, ft, opts );
59 figure
60 errorbar(xData, yData,err,'s', 'MarkerSize',4,'
       MarkerEdgeColor','black','MarkerFaceColor','black')
61 hold on
62 plot(fitresult)
63 xlabel( 'Distance(cm)', 'Interpreter', 'none' );
64 ylabel( 'Arbitrary unit', 'Interpreter', 'none' );
65 legend({'transmission point','fitted curve'})
66 coef=coeffvalues(fitresult);
67 FWHM=2*sqrt(log(2))*coef(3);
```

Bibliography

[1] Sebastian Polarz and B. Smarsly. *Nanoporous Materials*. Journal of Nanoscience and Nanotechnology **2**, 6 (2002), pp. 581–612.

[2] F. Höfling and T. Franosch. *Anomalous transport in the crowded world of biological cells*. Reports on Progress in Physics **76**, 4 (2013).

[3] F. Ge et al. *Unmodified single nanoparticles undergo a motion-pattern transition on the plasma membrane before cellular uptake*. Nano Today **39** (2021).

[4] D. Mendels and N. Tessler. *Drift and diffusion in disordered organic semiconductors: The role of charge density and charge energy transport*. Journal of Physical Chemistry C **117** (2013).

[5] E. Selivanovitch, B. LaFrance, and T. Douglas. *Molecular exclusion limits for diffusion across a porous capsid*. Nature Communications **12** (2021).

[6] C.K. Regmi et al. *Exploring the diffusion of molecular oxygen in the red fluorescent protein mCherry using explicit oxygen molecular dynamics simulations*. Journal of Physical Chemistry B **117** (2013).

[7] C. Bousige, P. Levitz, and B. Coasne. *Bridging scales in disordered porous media by mapping molecular dynamics onto intermittent Brownian motion*. Nature Communications **12**, 1 (2021).

[8] J. Zhang et al. *A metaheuristic-optimized multi-output model for predicting multiple properties of pervious concrete*. Construction and Building Materials **249** (2020).

[9] R.A. Minz et al. *Trapping of rare earth-doped nanorods using quasi Bessel beam optical fiber tweezers*. OSA Continuum **4**, 2 (2021), pp. 364–373.

[10] Jiaquan Xu et al. *Assembly of metals and nanoparticles into novel nanocomposite superstructures*. Scientific reports **3** (2013), p. 1730.

[11] S. Villalba, H. Failache, and A. Lezama. *Light-induced atomic desorption and diffusion of Rb from porous alumina*. Phys. Rev. A **81** (2010), p. 032901.

[12] R.B. Ambade et al. *Ultrafast flashlight sintered mesoporous NiO nanosheets for stable asymmetric supercapacitors*. Chemical Engineering Journal **436** (2022).

[13] L. Ding et al. *In-situ formation of nanosized 1T-phase MoS_2 in B-doped carbon nitride for high efficient visible-light-driven H_2 production*. Journal of Colloid and Interface Science **614** (2022), pp. 92–101.

[14] S. Zhang et al. *Influence of particle size on pore structure and multifractal characteristics in coal using low-pressure gas adsorption*. Journal of Petroleum Science and Engineering **212** (2022).

[15] K. Curran and J.S. Marshall. *Stochastic model of oscillatory diffusion for colloidal particles in a fixed porous bed*. Chemical Engineering Science **246** (2021).

[16] Tomas Svensson et al. *Holey random walks: Optics of heterogeneous turbid composites*. Phys. Rev. E **87** (2 2013), p. 022120.

[17] A. Ehrmann and T. Blachowicz. *Magnetic force microscopy on nanofibers—limits and possible approaches for randomly oriented nanofiber mats*. Magnetochemistry **7** (2021).

[18] M. Pan et al. *A stochastic model for thermal transport of nanofluid in porous media: Derivation and applications*. Computers and Mathematics with Applications **75**, 4 (2018), pp. 1226–1236.

[19] G. De Crozals et al. *Oligonucleotide solid-phase synthesis on fluorescent nanoparticles grafted on controlled pore glass*. RSC Advances **2**, 31 (2012), pp. 11858–11866.

[20] E. Mariotti et al. *Nanoparticle formation in nanoporous structures and applications*. Optical and Quantum Electronics **52** (2020), pp. 1–10.

[21] Ying Diao et al. *The role of nanopore shape in surface-induced crystallization*. Nature materials **10** (2011), pp. 867–71.

[22] M. Baker, W. Liu, and E. McLeod. *Accurate and fast modeling of scattering from random arrays of nanoparticles using the discrete dipole approximation and angular spectrum method*. Optics Express **29**, 14 (2021), pp. 22761–22777.

[23] Tomas Svensson et al. *Light diffusion in quenched disorder: Role of step correlations*. Physical Review E **89** (2014).

[24] Bruno F. Soares, Fredrik Jonsson, and Nikolay I. Zheludev. *All-Optical Phase-Change Memory in a Single Gallium Nanoparticle*. Phys. Rev. Lett. **98** (15 2007), p. 153905.

[25] Sudhanshu Srivastava et al. *Light-Controlled Self-Assembly of Semiconductor Nanoparticles into Twisted Ribbons*. Science (New York, N.Y.) **327** (2010), pp. 1355–9.

[26] A. Burchianti et al. *Optical characterization and manipulation of alkali metal nanoparticles in porous silica*. European Physical Journal D **49**, 2 (2008), pp. 201–210.

[27] N.G. Semaltianos and G. Karczewski. *Laser Synthesis of Magnetic Nanoparticles in Liquids and Application in the Fabrication of Polymer-Nanoparticle Composites*. ACS Applied Nano Materials **4**, 7 (2021), pp. 6407–6440.

[28] T.A. Vartanyan et al. *Change in the states of optically excited Rb atoms near sapphire surface*. Optics and Spectroscopy (English translation of Optika i Spektroskopiya) **115** (2013), pp. 60–67.

[29] A. Cappello et al. *Light induced atomic desorption from dry-film coatings*. The Journal of chemical physics **127** (2007), p. 044706.

[30] A. Burchianti et al. *Optical recording in Rb loaded-porous glass by reversible photoinduced phase transformations*. Opt. Express **16** (2008), pp. 1377–1384.

[31] A. Gozzini et al. *Light-induced ejection of alkali atoms in polysiloxane coated cells*. Il Nuovo Cimento D **15**, 5 (1993), pp. 709–722. ISSN: 03926737.

[32] D.S. Barker et al. *Light-induced atomic desorption of lithium*. Physical Review A **98** (2018).

[33] S.N. Atutov et al. *Light-induced diffusion and desorption of alkali metals in a siloxane film: Theory and experiment*. Physical Review A - Atomic, Molecular, and Optical Physics **60**, 6 (1999), pp. 4693–4700.

[34] H.L. Macdonell. *Porous glass chromatography*. Nature **189**, 4761 (1961), pp. 302–303.

[35] A.C. Lewis et al. *Microfabricated planar glass gas chromatography with photoionization detection*. Journal of Chromatography A **1217**, 5 (2010), pp. 768–774.

[36] S.R. Jim et al. *Engineered anisotropic microstructures for ultrathin-layer chromatography*. Analytical Chemistry **82**, 12 (2010), pp. 5349–5356.

[37] J.A. Kraai, A.X. Wang, and G.L. Rorrer. *Photonic Crystal Enhanced SERS Detection of Analytes Separated by Ultrathin Layer Chromatography Using a Diatom Frustule Monolayer*. Advanced Materials Interfaces **7**, 11 (2020).

[38] T. Meng et al. *A thermo-responsive affinity membrane with nano-structured pores and grafted poly(N-isopropylacrylamide) surface layer for hydrophobic adsorption*. Journal of Membrane Science **349**, 1-2 (2010), pp. 258–267.

[39] M.J. Greaney et al. *Indicator displacement assays for amino acids using Ni-NTA tethered to PAMAM dendrimers on controlled pore glass*. Chemical Communications **46**, 29 (2010), pp. 5337–5339.

[40] D.J. Greene et al. *Caustic-Stable, Controlled-Pore Glass-Ceramics*. Crystal Growth and Design **21** (2021), pp. 809–816.

[41] J. Parrado and J. Bautista. *Immobilization-Stabilization of Kerase, a Serine Protease from Streptomyces fradiae, by Covalent Attachment to Porous Glass*. Bioscience Biotechnology and Biochemistry **59**, 5 (1995), pp. 906–907.

[42] R. Turgis et al. *An original "click and bind" approach for immobilizing copper hexacyanoferrate nanoparticles on mesoporous silica*. Chemistry of Materials **25** (2013), pp. 4447–4453.

[43] D. Li, N.A. Ackaah-Gyasi, and B.K. Simpson. *Immobilization of bovine trypsin onto controlled pore glass*. Journal of Food Biochemistry **38**, 2 (2014), pp. 184–195.

[44] M.J. Damha, P.A. Giannaris, and S.V. Zabarylo. *An improved procedure for derivatization of controlled-pore glass beads for solid-phase oligonucleotide synthesis*. Nucleic Acids Research **18**, 13 (1990), pp. 3813–3821.

[45] Georgiy Shakhgildyan et al. *Nanoporous Glass with Controlled Pore Size for High-Efficiency Synthesis of Oligonucleotides*. Glass and Ceramics **75** (2019).

[46] R. Müller et al. *Ultra-thin porous glass membranes - An innovative material for the immobilization of active species for optical chemosensors*. Talanta **107** (2013), pp. 255–262.

[47] R. Lebullenger et al. *Glass foams for environmental applications*. Journal of Non-Crystalline Solids **356**, 44 (2010), pp. 2562–2568.

[48] Serge Caron et al. *Porous Glass Optical Fiber Sensor As an End-Of-Service Indicator for Respiratory Cartridges*. Sensors and Actuators B: Chemical **102** (2004), 198–206.

[49] S. Uemiya et al. *Steam reforming of methane in a hydrogen-permeable membrane reactor*. Applied Catalysis **67**, 1 (1990), pp. 223–230.

[50] H. Yang, Y. Lu, and B.J. Tatarchuk. *Glass fiber entrapped sorbent for reformates desulfurization for logistic PEM fuel cell power systems*. Journal of Power Sources **174**, 1 (2007), pp. 302–311.

[51] C.E. Megiris and J.H.E. Glezer. *Synthesis of H_2-Permselective Membranes by Modified Chemical Vapor Deposition. Microstructure and Permselectivity of SiO_2/C /Vycor Membranes*. Industrial & Engineering Chemistry Research **31**, 5 (1992), pp. 1293–1299.

[52] R. Liu et al. *Preparation of uniform-sized PLA microcapsules by combining Shirasu Porous Glass membrane emulsification technique and multiple emulsion-solvent evaporation method*. Journal of Controlled Release **103**, 1 (2005), pp. 31–43.

[53] M. Kukizaki and M. Goto. *Demulsification of water-in-oil emulsions by permeation through Shirasu-porous-glass (SPG) membranes*. Journal of Membrane Science **322**, 1 (2008), pp. 196–203.

[54] J. Zhang et al. *Effect of membrane wettability on membrane fouling and chemical durability of SPG membranes*. Separation and Purification Technology **36**, 5 (2015), pp. 1694–1699.

[55] S.N.N.M. Makhtar et al. *Preparation, characterization and performance evaluation of supported zeolite on porous glass hollow fiber for desalination application*. Arabian Journal of Chemistry **13**, 1 (2020), pp. 3429–3439.

[56] E. Magal et al. *Colloid transport in porous media: Impact of hyper-saline solutions*. Water Research **45**, 11 (2011), pp. 3521–3532.

[57] N.E. Weckman et al. *Multiplexed DNA Identification Using Site Specific dCas9 Barcodes and Nanopore Sensing*. ACS Sensors **4** (2019), pp. 2065–2072.

[58] N.A.W. Bell et al. *Multiplexed ionic current sensing with glass nanopores*. Lab on a Chip **13** (2013), pp. 1859–1862.

[59] K. Shen et al. *On-chip optical levitation with a metalens in vacuum*. Optica **8**, 11 (2021), pp. 1359–1362.

[60] V.N. Pak, A.N. Borisov, and G.G. Tengerekova. *Photochromic Properties of Porous Glass Modified with Molybdenum Oxide Groups*. Russian Journal of Applied Chemistry **91** (2018), pp. 375–378.

[61] T.V. Antropova et al. *Spectral properties of the high-silica porous glasses doped by silver halides*. Journal of Luminescence **193** (2018), pp. 29–33.

[62] N. A. Toropov et al. *Absorption and photoluminescence of epitaxial quantum dots in the near field of silver nanostructures*. J. Opt. Technol. **84** (2017), pp. 459–461.

[63] Muhammad Hasanuzzaman et al. *Production and Treatment of Porous Glass Materials for Advanced Usage*. Reference Module in Materials Science and Materials Engineering (2015).

[64] Walter I. Goldburg. *The Dynamics of Phase Separation Near the Critical Point: Spinodal Decomposition and Nucleation*. *Scattering Techniques Applied to Supramolecular and Nonequilibrium Systems*. Ed. by Sow-Hsin Chen, Benjamin Chu, and Ralph Nossal. Springer US, 1981, pp. 383–409.

[65] Mohamed Laradji, Soren Toxvaerd, and Ole Mouritsen. *Molecular Dynamics Simulation of Spinodal Decomposition in Three-Dimensional Binary Fluids*. Physical review letters **77** (1996), pp. 2253–2256.

[66] L. D. Gelb and K. E. Gubbins. *Characterization of Porous Glasses: Simulation Models, Adsorption Isotherms, and the Brunauer-Emmett-Teller Analysis Method*. Langmuir **14**, 8 (1998), pp. 2097–2111.

[67] P. Guenoun et al. *Spinodal decomposition patterns in an isodensity critical binary fluid: Direct-visualization and light-scattering analyses*. Phys. Rev. A **36**, 10 (1987), pp. 4876–4890.

[68] H. Lüth. *Solid Surfaces, Interfaces and Thin Films*. Springer Berlin Heidelberg, 2010.

[69] Zhujun Zhou et al. *Effect of heat treatment on* $7Na_2O - 23B_2O_3 - 70SiO_2$ *glass*. Ceramics International **37**, 6 (2011), pp. 1769–1773.

[70] V. Beschieru, B. Rathke, and S. Will. *Particle diffusion in porous media investigated by dynamic light scattering*. Microporous and Mesoporous Materials **125**, 1 (2009), pp. 63–69.

[71] M. Hermann. *Private Comunication*. VitraBio GmbH (2007).

[72] A. Burchianti et al. *Photo-ejection and transport of alkali atoms embedded in nanoporous silica*. Journal of Physics: Conference Series **19**, 1 (2005), pp. 86–89.

[73] Igor Levin and David Brandon. *Metastable Alumina Polymorphs: Crystal Structures and Transition Sequences*. Journal of the American Ceramic Society **81** (2005), pp. 1995 –2012.

[74] Priyanka Nayar et al. *Structural, optical and mechanical properties of amorphous and crystalline alumina thin films*. Thin Solid Films **568** (2014), pp. 19–24.

[75] M. Bauccio. *ASM engineered materials reference book*. ASM international, 1994.

[76] Fathi Habashi. *A short history of hydrometallurgy*. Hydrometallurgy **79** (2005), pp. 15–22.

[77] George V. Franks and Yang Gan. *Crystal Structure of Alumina Oxide and Hydroxide Phases.* Materials Science (2007).

[78] Andrew R. Hind, Suresh K. Bhargava, and Stephen C. Grocott. *The surface chemistry of Bayer process solids: a review*. Colloids and Surfaces A: Physicochemical and Engineering Aspects **146**, 1 (1999), pp. 359–374.

[79] N.A. Vinogradov et al. *Observation of Pore Growth and Self-Organization in Anodic Alumina by Time-Resolved X-ray Scattering*. ACS Applied Nano Materials **1**, 3 (2018), pp. 1265–1271.

[80] S. Habibi, A. Jafari, and Z. Fakhroueian. *Application of novel functionalized Al_2O_3/silica by organosiloxane and amine reagents for enhanced oil recovery*. Applied Nanoscience (Switzerland) **10**, 7 (2020), pp. 2085–2100.

[81] P. Parikh. *Alumina Ceramics: Engineering Applications and Domestic Market Potential*. Transactions of the Indian Ceramic Society **54** (2014), pp. 179–184.

[82] P.-W. Guan, G. Houchins, and V. Viswanathan. *Uncertainty quantification of DFT-predicted finite temperature thermodynamic properties within the Debye model*. Journal of Chemical Physics **151**, 24 (2019).

[83] E.C. Nykwest, D. Trujillo, and S.P. Alpay. *Surface localized magnetism in transition metal doped alumina*. Scientific Reports **11**, 1 (2021).

[84] K.S. Sree Harsha. *Chapter 5 - Thermal Evaporation Sources*. Ed. by K.S. Sree Harsha. Elsevier, 2006.

[85] Almas Bashir et al. *Chapter 3 - Interfaces and surfaces*. *Chemistry of Nanomaterials*. Ed. by Tahir Iqbal Awan, Almas Bashir, and Aqsa Tehseen. Elsevier, 2020, pp. 51–87.

[86] J. George. Ed. by J. George. Marcel Dekker, 1992.

[87] Alexandr Klimov et al. *Electron beam evaporation of alumina ceramics at forevacuum pressure range*. AIP Conference Proceedings **1772** (2016), p. 040003.

[88] I. Neelakanta Reddy et al. *Nanostructured alumina films by E-beam evaporation*. Ceramics International **41**, 9, Part A (2015), pp. 10537–10546.

[89] *Refractiveindex.info*. URL: https://refractiveindex.info/.

[90] H.-Y. Joo et al. *Spectrophotometric analysis of aluminum nitride thin films*. Journal of Vacuum Science and Technology A: Vacuum, Surfaces and Films **17**, 3 (1999), pp. 862–870.

[91] Jarosław Serafińczuk et al. *Depth dependent X-ray diffraction of porous anodic alumina films filled with cubic $YAlO_3 : Tb^{3+}$ matrix*. Optica Applicata **50** (2020), pp. 127–134.

[92] H. J. Butt, Graf K., and Kappl M. *Physics and Chemistry of Interfaces*. John Wiley e Sons, Ltd, 2003. Chap. 9.

[93] M.J. Hossain, M.M. Rahman, and M. Jafar Sharif. *Preference for low-coordination sites by adsorbed CO on small platinum nanoparticles*. Nanoscale Advances **2** (2020), pp. 1245–1252.

[94] M. Oria et al. *Spectral Observation of Surface-Induced Van der Waals Attraction on Atomic Vapour*. EPL (Europhysics Letters) **14** (1991), p. 527.

[95] Luca Marmugi. *Optical control of atomic transport and reversible self-assembly of nanoparticles in porous glass*. PhD thesis. Università degli Studi di Siena, 2013.

[96] W. Demtröder. *Atoms, Molecules and Photons*. Springer Berlin Heidelberg, 2018.

[97] Nicholas Stadie. *Synthesis and Thermodynamic Studies of Physisorptive Energy Storage Materials*. PhD thesis. California Institute of Technology, 2013.

[98] Alessia Burchianti. *Light-Induced Atomic Desorption general features and applications*. PhD thesis. Università degli Studi di Siena, 2003.

[99] A.-L. Barabasi and H. E. Stanley. *Fractal Concepts in Surface Growth*. Cambridge University Press, 1995.

[100] A. D. Slepkov et al. *Generation of large alkali vapor densities inside bare hollow-core photonic band-gap fibers*. Optics express **16** (2008), pp. 18976–83.

[101] K. Saha et al. *Enhanced Two-Photon Absorption in a Hollow-Core Photonic Bandgap Fiber*. Physical Review A **83** (2011), p. 033833.

[102] C. Perrella et al. *High-efficiency cross-phase modulation in a gas-filled waveguide*. Phys. Rev. A **88** (2013), p. 013819.

[103] M Meucci et al. *Light-Induced Atom Desorption*. Europhysics Letters (EPL) **25**, 9 (1994), pp. 639–643.

[104] A Burchianti et al. *Light-induced atomic desorption and related phenomena*. Physica Scripta **T135** (2009), p. 014012.

[105] Steinn Agustsson et al. *Enhanced Atomic Desorption of 209 and 210 Francium from Organic Coating*. Scientific Reports **7** (2017), p. 4207.

[106] Stoyan Tsvetkov, M. Taslakov, and Sanka Gateva. *Dynamics of the light-induced atomic desorption at homogeneous illumination*. Applied Physics B **123**, 3 (2017).

[107] Marinelli, C. et al. *Desorption of Rb and Cs from PDMS induced by non resonant light scattering*. European Physical Journal D **37** (2006), pp. 319–325.

[108] Jonathan Brewer et al. *Dynamics of alkali-metal atom photodesorption from polymer thin films*. Phys. Rev. A **69** (2004).

[109] Gozzini, S. and Lucchesini, A. *Light-induced potassium desorption from polydimethylsiloxane film*. Eur. Phys. J. D **28**, 2 (2004), pp. 157–162.

[110] Jihua Xu et al. *Photo-atomic effect: Temperature dependence of the photodesorption of Na and Na_2 from polymer surfaces*. The European Physical Journal D **10** (2000), pp. 243–246.

[111] A. Burchianti et al. *Reversible Light-Controlled Formation and Evaporation of Rubidium Clusters in Nanoporous Silica*. Physical Review Letters **97**, 15 (2006).

[112] A. Burchianti et al. *Light-induced atomic desorption from porous silica*. Europhysics Letters **67**, 6 (2004), pp. 983–989.

[113] L. Marmugi et al. *Laser-driven self-assembly of shape-controlled potassium nanoparticles in porous glass*. Laser Physics Letters **11**, 8 (2014).

[114] C. Marinelli et al. *A new class of photo-induced phenomena in siloxane films*. The European Physical Journal D - Atomic, Molecular, Optical and Plasma Physics **13** (2001), pp. 231–235.

[115] Eliran Talker et al. *Light-Induced Atomic Desorption in Microfabricated Vapor Cells for Demonstrating Quantum Optical Applications*. Phys. Rev. Applied **15** (2021), p. L051001.

[116] S. N. Atutov et al. *Fast and efficient loading of a Rb magneto-optical trap using light-induced atomic desorption*. Phys. Rev. A **67** (2003), p. 053401.

[117] B. P. Anderson and M. A. Kasevich. *Loading a vapor-cell magneto-optic trap using light-induced atom desorption*. Physical Review A **63**, 2 (2001).

[118] Shengwang Du et al. *Atom-chip Bose-Einstein condensation in a portable vacuum cell*. Phys. Rev. A **70** (2004).

[119] Ken'ichi Nakagawa et al. *Simple and efficient magnetic transport of cold atoms using moving coils for the production of Bose–Einstein condensation*. Applied Physics B **81** (2005), pp. 791–794.

[120] C. Klempt et al. *Ultraviolet light-induced atom desorption for large rubidium and potassium magneto-optical traps*. Phys. Rev. A **73** (2006), p. 013410.

[121] E. B. Alexandrov et al. *Light-induced desorption of alkali-metal atoms from paraffin coating*. Phys. Rev. A **66** (4 2002), p. 042903.

[122] Gozzini, S. et al. *Light-induced sodium desorption from paraffin film*. Eur. Phys. J. D **47**, 1 (2008), pp. 1–5.

[123] R.A Bernheim et al. *Threshold energy for the photon-stimulated desorption of Rb atoms from polydimethylsiloxane films*. Chemical Physics Letters **332** (2000), pp. 1–4.

[124] Jihua Xu et al. *Photo-atomic effect: Temperature dependence of the photodesorption of Na and Na-2 from polymer surfaces*. The European Physical Journal D **10** (2000), pp. 243–246.

[125] Atsushi Hatakeyama, Markus Wilde, and Katsuyuki Fukutani. *Classification of Light-Induced Desorption of Alkali Atoms in Glass Cells Used in Atomic Physics Experiments*. e-Journal of Surface Science and Nanotechnology **4** (2006), pp. 63–68.

[126] Kiminori Sato. *Study of Alkali-Metal Vapor Diffusion into Glass Materials*. Japanese Journal of Applied Physics **52** (2013), p. 086601.

[127] T. Karaulanov et al. *Controlling atomic vapor density in paraffin-coated cells using light-induced atomic desorption*. Phys. Rev. A **79** (2009), p. 012902.

[128] A. Lucchesini et al. *Low Energy Atomic Photodesorption from Organic Coatings*. Coatings **6** (2016), p. 47.

[129] A. Burchianti et al. *Optical response of alkali metal atoms confined in nanoporous glass*. Quantum Electronics **44**, 3 (2014), pp. 263–268.

[130] S. Villalba et al. *Rb optical resonance inside a random porous medium*. Optics Letters **38** (2013), p. 193.

[131] A. Bogi. *Photo-induced process in polymers and porous silica loaded with alkali metals*. PhD thesis. Università degli Studi di Siena, 2007.

[132] C. Marinelli et al. *a New Setup for the Study of Adsorption/Desorption Processes and Nanoparticles Formation in Porous Alumina*. Journal of the Siena Academy of Sciences **10**, 1 (2019).

[133] P.D. McDowall et al. *An atomic beam source for fast loading of a magneto-optical trap under high vacuum*. Review of Scientific Instruments **83** (2012).

[134] V. Dugrain, P. Rosenbusch, and J. Reichel. *Alkali vapor pressure modulation on the 100 ms scale in a single-cell vacuum system for cold atom experiments*. Review of Scientific Instruments **85** (2014).

[135] L. Torralbo-Campo et al. *Light-induced atomic desorption in a compact system for ultracold atoms*. Scientific Reports **5** (2015).

[136] M. Stephens, R. Rhodes, and C. Wieman. *Study of wall coatings for vapor-cell laser traps*. Journal of Applied Physics **76** (1994), pp. 3479–3488.

[137] Frank O. Goodman and Harold Y. Wachman. *Dynamics of Gas-Surface Scattering*. Academic Press, 1976.

[138] K. Rębilas. *Comment on "Light-induced atomic desorption and diffusion of Rb from porous alumina"*. Phys. Rev. A **82** (2010), p. 056901.

[139] J. H. Xu et al. *Photoatomic effect: Light-induced ejection of Na and Na_2 from polydimethylsiloxane surfaces*. Phys. Rev. A **54** (4 1996).

[140] Theodore E. Madey, Robert E. Johnson, and Thom M. Orlando. *Far-out surface science: radiation-induced surface processes in the solar system*. Surface Science **500**, 1 (2002), pp. 838–858.

[141] S. Biswal, D.S. Bhaskaram, and G. Govindaraj. *Role of graphene oxide in modifying magnetism in α-Fe_2O_3 nanoparticles: Raman and magnetization studies*. Materials Chemistry and Physics **266** (2021).

[142] Jonathan A. Scholl et al. *Observation of Quantum Tunneling between Two Plasmonic Nanoparticles*. Nano Letters **13**, 2 (2013), pp. 564–569.

[143] A. Ahmad, S.K. Srivastava, and A.K. Das. *First-principles calculations and experimental studies on Co2FeGe Heusler alloy nanoparticles for spintronics applications*. Journal of Alloys and Compounds **878** (2021).

[144] L. Martinetz et al. *Quantum electromechanics with levitated nanoparticles*. npj Quantum Information **6**, 1 (2020).

[145] A.C. Gandhi et al. *Surface-spin driven room temperature magnetic memory effect in Fe-substituted NiO nanoparticles*. Applied Surface Science **536** (2021).

[146] Ana Ledo-Suárez et al. *Thermal annealing as an easy tool for the controlled arrangement of gold nanoparticles in block-copolymer thin films*. Nanotechnology **24** (2013), p. 255304.

[147] Tanya Hutter, Stephen Elliott, and Sumeet Mahajan. *Interaction of metallic nanoparticles with dielectric substrates: effect of optical constants*. Nanotechnology **24** (Dec. 2012), p. 035201.

[148] R.H. Thabet et al. *Catalytic oxidation over nanostructured heterogeneous process as an effective tool for environmental remediation*. IOP Conference Series: Materials Science and Engineering **975**, 1 (2020).

[149] Y. Cao et al. *Synthesis of molecular-imprinting polymer coated magnetic nanocomposites for selective capture and fast removal of environmental tricyclic analogs*. Chemical Engineering Journal **426** (2021).

[150] Suljo Linic, Phillip Christopher, and David Ingram. *Plasmonic-metal nanostructures for efficient conversion of solar to chemical energy*. Nature materials **10** (Nov. 2011), pp. 911–21.

[151] E. Piktel et al. *Varied-shaped gold nanoparticles with nanogram killing efficiency as potential antimicrobial surface coatings for the medical devices*. Scientific Reports **11**, 1 (2021).

[152] Yunlu Dai et al. *Drug Delivery: Platinum (IV) Pro-Drug Conjugated $NaYF_4$: Yb^{3+}/Er^{3+} Nanoparticles for Targeted Drug Delivery and Up-Conversion Cell Imaging*. Advanced Healthcare Materials **2** (2013), pp. 514–514.

[153] Alan Mcnally. *Magnetic sensors: Nanoparticles detect infection*. Nature nanotechnology **8** (2013), pp. 315–6.

[154] U. Kreibig and M. Vollmer. *Optical Properties of Metal Clusters*. Springer-Verlag Berlin Heidelberg, 1995.

[155] K. Lance Kelly et al. *The Optical Properties of Metal Nanoparticles: The Influence of Size, Shape, and Dielectric Environment*. The Journal of Physical Chemistry B **107**, 3 (2003), pp. 668–677.

[156] Cecilia Noguez. *Surface Plasmons on Metal Nanoparticles: The Influence of Shape and Physical Environment*. The Journal of Physical Chemistry C **111**, 10 (2007), pp. 3806–3819.

[157] Lukas Novotny and Bert Hecht. *Principles of Nano-Optics*. Cambridge University Press, 2006.

[158] P. N. Prasad. *Nanophotonics*. John Wiley & Sons, Ltd, 2004.

[159] S. A. Maier. *Plasmonics: Fundamentals and Applications*. Springer, 2007.

[160] J. D. Jackson and R. F. Fox. *Classical Electrodynamics, 3rd ed.* American Journal of Physics **67** (1999), pp. 841–842.

[161] G. Mie. *Beiträge zur Optik trüber Medien, speziell kolloidaler metallösungen*. Annalen der physik **330**, 3 (1908), pp. 377–445.

[162] U. Kreibig, B. Schmitz, and H. D. Breuer. *Separation of plasmon-polariton modes of small metal particles*. Phys. Rev. B **36** (9 1987), pp. 5027–5030.

[163] U. Kreibig. *Kramers Kronig analysis of the optical properties of small silver particles*. Zeitschrift für Physik **234**, 4 (1970), pp. 307–318.

[164] R. Gans. *Über die Form ultramikroskopischer Goldteilchen.* Annalen der Physik **342** (1912), pp. 881 –900.

[165] R. Gans. *Über Die Form Ultramikroskopischer Silberteilchen*. Annalen der Physik **352** (1915), pp. 270 –284.

[166] C. F. Bohren and D. R. Huffman. *Absorption and Scattering of Light by Small Particles*. Wiley-VCH Verlag GmbH, 1983.

[167] S. Link, M. B. Mohamed, and M. A. El-Sayed. *Simulation of the Optical Absorption Spectra of Gold Nanorods as a Function of Their Aspect Ratio and the Effect of the Medium Dielectric Constant*. Journal of Physical Chemistry B **103** (1999), pp. 3073–3077.

[168] C. Bréchignac et al. *Collective resonance in large free potassium cluster ions*. Phys. Rev. Lett. **68** (1992), pp. 3916–3919.

[169] C. Bréchignac et al. *Optical response of large lithium clusters: Evolution toward the bulk*. Phys. Rev. Lett. **70** (1993), pp. 2036–2039.

[170] Hugh H. Richardson et al. *Thermo optical Properties of Gold Nanoparticles Embedded in Ice: Characterization of Heat Generation and Melting*. Nano Letters **6**, 4 (2006), pp. 783–788.

[171] W. Hoheisel et al. *Desorption stimulated by laser-induced surface-plasmon excitation*. Phys. Rev. Lett. **60** (1988), pp. 1649–1652.

[172] I. Lee et al. *Surface-plasmon-induced desorption by the attenuated-total-reflection method*. Physical Review B **39** (1989), pp. 8012–8014.

[173] Atsushi Hatakeyama et al. *Atomic alkali-metal gas cells at liquid-helium temperatures: Loading by light-induced atom desorption*. Physical Review A **65** (2002), pp. 22904–.

[174] W. Hoheisel, M. Vollmer, and F. Träger. *Desorption of metal atoms with laser light: Mechanistic studies*. Phys. Rev. B **48** (1993), pp. 17463–17476.

[175] J.L. Bao and E.A. Carter. *Surface-Plasmon-Induced Ammonia Decomposition on Copper: Excited-State Reaction Pathways Revealed by Embedded Correlated Wavefunction Theory*. ACS Nano **13** (2019), pp. 9944–9957.

[176] M. Vollmer et al. *Size manipulation of metal particles with laser light*. Phys. Rev. B **40** (1989), pp. 12509–12512.

[177] A. Sarracino et al. *Sub-100 nm high spatial frequency periodic structures driven by femtosecond laser induced desorption in GaAs*. Applied Physics Letters **118** (2021).

[178] *Alkali Metal Dispensers*. SAES getters, 2007.

[179] Oleg Kostko. *Photoelectron spectroscopy of mass-selected sodium, coinage metal and divalent metal cluster anions* (2007).

[180] *Channeltron Electron Multiplier Handbook For Mass Spectrometry Applications*. BURLE, 1996, pp. 1–64.

[181] *Technical description and instruction manual of an extended cavity diode laser ECDL-7830R (S/N 031944)*. VitaWave. 2019.

[182] Michal Smolik, Vaclav Skala, and Ondrej Nedved. *A Comparative Study of LOWESS and RBF Approximations for Visualization*. Lecture Notes in Computer Science **9787** (2016), 405–419.

[183] S. N. Atutov et al. *Light-induced diffusion and desorption of alkali metals in a siloxane film: Theory and experiment*. Phys. Rev. A **60** (1999), pp. 4693–4700.

[184] P.A. Petrov et al. *Photodesorption of rubidium atoms from a sapphire surface*. Optics and Spectroscopy **123**, 4 (2017), pp. 574–577.

[185] Marvin J. Weber. *Handbook of Laser Science and Technology, Volume IV, Optical Materials: Part 2*. **12**. CRC Press, 1986.

[186] O. Glemser. *Vapor Pressure of the Chemical Elements*. Angewandte Chemie **76**, 15 (1964), pp. 695–695.

[187] E. Kolobkova and N. Nikonorov. *Metal sodium nanoparticles in fluorophosphate glasses*. Journal of Alloys and Compounds **637** (2015), pp. 545–551.

[188] Rafael Drampyan et al. *Optical Shaping of Surface Metal Microstructures via Nondiffracting Beam Controlled Atomic Deposition*. Photonics and Nanostructures - Fundamentals and Applications **31** (June 2018), pp. 71–76.

[189] Francesco Sarri. *Optical microstructuring of alkali metal nanoparticle coatings on porous silica substrates induced by Bessel beam*. PhD thesis. Università degli Studi di Siena, 2019.